acta physica slovaca vol. 61 No. 4, 391 – 482 August 2011

COMPUTATIONAL NANOFLUIDICS: NONLOCAL TRANSPORT AND THE GLASS TRANSITION

Ruslan M. Puscasu[1]
Swinburne University of Technology, Melbourne, Victoria, 3122, Australia

Received 5 September 2011, accepted 6 September 2011

The paper gives a review of recent advances in theory and simulation of nonlocal transport in nanoflows. The aim is to show how to computationally model and simulate the nonlocal viscous transport in atomic and molecular fluids. The ultimate goal is to provide nanofluidics and other disciplines with methodologies capable to give exact descriptions of flow at the nanoscale by using nonlocal constitutive relations which involve nonlocal transport kernels.

Nanomaterials have properties that can be substantially different from those of the corresponding bulk phases. In particular, fluid flows in pores or channels of nanoscale dimension can deviate strongly from macroscopic expectations. When such structures approach the size regime corresponding to molecular scaling lengths, new physical constraints are placed on the behavior of the fluid. These physical constraints induce regions of the fluid to exhibit new properties (e.g. vastly increased viscosity near the pore wall) and they may affect changes in thermodynamic properties and may also alter the chemical reactivity of species at the fluid-solid interface. Consequently, many classical theories break down and are no longer valid at such small length and time scales.

The development of models that go beyond classical (Navier-Stokes-Fourier) hydrodynamics would be very helpful for the prediction and understanding of flows in highly confined geometries (typically 1-100 nm). While such nanoscale systems can be very difficult to probe experimentally, they can be easily approached in a very strict manner by molecular modelling, providing theory and simulation an opportunity for the discovery of new phenomena. We therefore review in this article the advances within the framework of generalized hydrodynamics and present the latest theoretical developments and modelling results that can ultimately lead to suitable predictive tools capable of accurate prediction of the key physical properties of fluids under nano-confined geometries.

[Continued on next page]

DOI: 10.2478/v10155-011-0004-8

PACS: 61.20.Ja, 61.25.H-, 61.25.Em, 61.25.hk, 64.70.pj, 66.20.Ej, 66.20.Gd, 66.20.-d, 66.20.Cy

KEYWORDS: Computational nanofluidics, Molecular dynamics, Nonlocal transport, Viscosity, Polymers, Glass transition

---

[1] E-mail address: rpuscasu@swin.edu.au

We start with an overview on the nonlocal constitutive relation and the microscopic definitions of the key properties such as momentum density autocorrelation function, stress autocorrelation function and the wavevector dependent viscosity. Then we demonstrate how the nonlocal viscosity kernel can be computed via equilibrium molecular dynamics. Firstly, we showcase the spatially nonlocal viscosity kernel for simple monatomic and diatomic fluids over a wide range of wavevectors, state points and potential energy functions. Further we consider more complex fluids; in particular, we report results for alkanes and polymer melts. Secondly, we study glass-forming liquids and therefore extend the temperature range and report the nonlocal viscosities of polymer melts cooled towards their glassy state. The results reveal the nonlocal nature of the viscous transport and we give evidence that the slow dynamics in supercooled liquids is governed by a dynamic critical point at which time and length scales diverge and link it to the dynamic heterogeneity. It follows that the response of polymer melts to a velocity gradient near the glass transition temperature is highly nonlocal.

In systems where the strain rate varies significantly over the width of the real space kernels, the generalized nonlocal viscosity must be used in order to correctly compute the velocity profile of molecular fluids via use of generalized hydrodynamics and thus the nonlocal behaviour of the transport must be integrated into methodologies developed to describe the multi-scale physics of nanoflows.

Contents

Notation

ABBREVIATIONS

ACF(s)	Autocorrelation function(s)
CF(s)	Correlation function(s)
EOM	Equations of motion
EQ	Equilibrium
FENE	Finitely Extensible Nonlinear Elastic potential
FENE-LJ	Finitely Extensible Nonlinear Elastic model with Lennard-Jones potential
FJC	Freely jointed chain model
FJC-LJ	Freely jointed chain model with Lennard-Jones potential
FJC-WCA	Freely jointed chain model with Weeks-Chandler-Andersen potential
GT	Glass transition
k-space	Reciprocal or wave-vector space
LJ	Lennard-Jones potential
MCT	Mode-coupling theory
MD	Molecular dynamics
MIC	Minimum image convention
NEMD	Nonequilibrium molecular dynamics
NEq	Nonequilibrium
pbc	Periodic boundary conditions
PDF	Pair distribution function
RDF	Radial distribution function
r-space	Euclidian (real) space
VACF(s)	Velocity autocorrelation function(s)
VK	Viscosity kernel
WCA	Weeks-Chandler-Andersen interatomic potential

LATIN ALPHABET

$C(\mathbf{k},t)$	Momentum density correlation function
$\tilde{C}(\mathbf{k},\omega)$	Laplace transform of the momentum density correlation function
$C_\perp(\mathbf{k},t)$	Transverse momentum density correlation function
$\tilde{C}_\perp(\mathbf{k},\omega)$	Laplace transform of the transverse momentum density correlation function
$\mathbf{c}_{i\alpha}$	Peculiar velocity of site α of molecule i
$\mathbf{C}_{i\alpha}$	Peculiar velocity of site α of molecule i relative to the center of mass of molecule i
d	Dimensionality of the system
$\mathbf{F}_i$	Force acting on particle i
$\mathbf{F}_{ij}^{inter}$	Intermolecular force acting on molecule i due to molecule j
$\mathbf{F}_{i\alpha}^{C}$	Bond constraint force on site α of molecule i
$\mathbf{F}_{i}^{D}$	Dihedral force acting on site α of molecule i
$\mathbf{F}_{i\alpha}^{FENE}$	Force acting on site α of molecule i due to the FENE potential
$\mathbf{F}_{i\alpha}^{LJ}$	Force acting on site α of molecule i due to the Lennard-Jones potential
$g(i\mathbf{k}\cdot\mathbf{r})$	Fourier transforms of the Irving-Kirkwood operator
$g(\mathbf{r})$	Radial distribution function
$\mathbf{J}(\mathbf{r},t)$	Instantaneous momentum density
$\tilde{\mathbf{J}}^{A}(\mathbf{k},t)$	Fourier transform of the atomic momentum density
$\tilde{\mathbf{J}}^{M}(\mathbf{k},t)$	Fourier transform of the molecular momentum density
$\mathbf{k}$	Wavevector
k	Force constant for the FENE potential
k_y	The component of the wave-vector in y direction
k_B	Boltzmann's constant
L	Side length of a cubic simulation cell
$I_{C_\perp}(\mathbf{k},t)$	Integral of the transverse momentum density correlation function
$I_N(\mathbf{k},t)$	Integral of the stress correlation function
m_i	Mass of particle i
$m_{i\alpha}$	Mass of site α on molecule i
M	Molecular weight
M_i	Mass of molecule i
N_c	Number of degrees of freedom lost through constraint
N	Number of particles
N_a	Number of atoms

N_m	Number of molecules
N_s	Number of sites in a molecule
$N(\mathbf{k},t)$	Stress correlation function
$\tilde{N}(\mathbf{k},\omega)$	Laplace transform of the stress correlation function
$\mathbf{p}_i$	Peculiar momentum of atom i for monatomic systems or centre of mass momentum of molecule i for molecular systems
$\mathbf{p}_{i\alpha}$	Momentum of site α on molecule i
$\mathsf{\mathbf{P}}$	Pressure tensor
$\tilde{\mathsf{\mathbf{P}}}^{A}$	Atomic pressure tensor
$\tilde{\mathsf{\mathbf{P}}}^{A^{Chlorine}}$	Atomic pressure tensor for model Chlorine
$\tilde{\mathsf{\mathbf{P}}}^{A^{Butane}}$	Atomic pressure tensor for model Butane
$\tilde{\mathsf{\mathbf{P}}}^{A^{FENE}}$	Atomic pressure tensor for model FENE
$\tilde{\mathsf{\mathbf{P}}}^{A^{FJC}}$	Atomic pressure tensor for model FJC
$\tilde{\mathsf{\mathbf{P}}}^{M}$	Molecular pressure tensor
P_{xy}	xy element of the pressure tensor
$\mathbf{r}$	Position vector
$\mathbf{r}_i$	Position of atom i for monatomic systems or centre of mass position of molecule i for molecular systems
$\mathbf{r}_{i\alpha}$	Position of site α on molecule i
$\mathbf{r}_{i\alpha j\beta}$	Vector from site α of molecule i to site β of molecule j
r_{ij}	Distance between atoms i and j
R_0	Maximum extension of the FENE potential
$\mathbf{R}_{i\alpha}$	Position of site α of molecule i relative to the center of mass of molecule i
s_r	Residual standard deviation
s, t, t'	Time
T	Temperature
T_A	Atomic temperature
T_g	Glass transition temperature
T_M	Molecular temperature
$\mathbf{u}(\mathbf{r},t)$	Streaming velocity of a fluid
$\nabla\mathbf{u}(\mathbf{r},t)$	Velocity gradient tensor
V	Volume
$\mathbf{v}_i$	Velocity of atom i for monatomic systems or centre of mass velocity of molecule i for molecular systems
$\mathbf{v}_{i\alpha}$	Velocity of site α on molecule i

GREEK ALPHABET

δt	Integration timestep
$\delta(t)$	Dirac delta function (of time)
$\delta(\mathbf{r} - \mathbf{r}_i)$	Kirkwood delta function
$\dot{\gamma}$	Strain-rate
$\dot{\gamma}(\mathbf{r}, t)$	Strain-rate tensor
$\tilde{\dot{\gamma}}(\mathbf{k}, t)$	Fourier transform of the strain-rate
ϵ	Lennard-Jones energy parameter
η	Shear viscosity
$\eta(\mathbf{k}, w)$	Wavevector and frequency dependent viscosity
$\rho(\mathbf{r}, t)$	Density of a fluid
$\tilde{\rho}(\mathbf{k}, t)$	Fourier transform of the density
ρ_a	Atomic number density
$\tilde{\rho}_a$	Fourier transform of the atomic number density
ρ_m	Molecular number density
$\tilde{\rho}_m$	Fourier transform of the molecular number density
$\sigma(\mathbf{r}, t)$	Stress-tensor
σ_{LJ}	Effective diameter of the Lennard-Jones potential
w	Frequency
Φ_{ij}	Interatomic potential
$\Phi_{i\alpha j\beta}$	Potential of site α on molecule i due to site β on molecule j
Φ_c	Shift constant in the Weeks-Chandler-Andersen potential
Φ_{ij}^{FENE}	The FENE potential between atoms i and j
Φ_{ij}^{LJ}	Lennard-Jones potential between atoms i and j
Φ_{ij}^{WCA}	Weeks-Chandler-Anderson potential between atoms i and j
ζ_A	Atomic thermostat multiplier
ζ_M	Molecular thermostat multiplier

Introduction

Nanofluidics constitutes undoubtedly an emerging theme in modern science. New nanoscale devices are proliferating leading to exceptional progress in nanotechnology [Abgrall 2009]. Computational nanosciences, including theory, design, modelling and simulation are increasingly playing a key role in advancing nanotechnology. One of the directions in nanoscience which has already born some exciting results is nanofluidics.

In general, nanofluidics can be defined as ”the study and application of fluid flow in and around nanosized objects” [Eijkel 2005, Bruus 2008, Tabeling 2005]. Though a rapid development of new applications using liquids containing suspended nanometer-size solid particles is extremely exciting on its own [Wang 2008a, Wang 2008b, Goff 208, Keblinski 2005], we only devote our study to ”purely” fluidic systems that are confined to structures of nanometer length scales.

A key branch of nanoscience is *computational nanofluidics*. Computational nanofluidics is crucial for the fundamental understanding and design of nanofluidic flows. While the great minds of the nineteenth and twentieth centuries understood the phenomena they were investigating before they cast them into models, today we do the opposite; many modern theories do not provide intuitive insights into the phenomena they are describing. By using advanced computational techniques we can increase the level of understanding phenomena which are difficult to imagine and comprehend; we can make these phenomena as meaningful as classical theories were to those who developed them.

For instance, nanofluidics is a field that has developed, in a broad sense, not as an extension and improvement of microfluidic systems, but rather as a way of exploiting certain unusual physical phenomena that simply do not exist at larger length scales [Edel 2009]. In this nanofluidic regime the characteristic physical scaling lengths of the fluid, (e.g. Debye length, hydrodynamic radius) very closely coincide with the dimensions of the nanostructure itself. When structures approach the size regime corresponding to molecular scaling lengths, new physical constraints are placed on the behavior of the fluid. For example, these physical constraints induce regions of the fluid to exhibit new properties not observed in bulk, (e.g. vastly increased viscosity near the pore wall); they may affect changes in thermodynamic properties and may also alter the chemical reactivity of species at the fluid-solid interface. Consequently, many classical theories break down and are no longer valid at such small length and time scales.

Classical Navier-Stokes-Fourier hydrodynamics, for instance, is limited to wide channels and small fields, therefore the development of models that go beyond classical hydrodynamics would be very helpful for the prediction and understanding of flows in highly confined geometries (typically 1-100 nm). There are many aspects that make classical treatment even more difficult, e.g. strong density inhomogeneities [Bitsanis 1988, Bitsanis 1990], fluid slip at solid surfaces [Thompson 1997, Cieplak 2001, Zhu 2003, Petravic 2007, Sokhan 2008, Bhatia 2008, Hansen 2010] etc.

We decided to tackle one of the problems in nanofluidics, namely spatial nonlocality. In the same way that every fluid must be regarded as viscoelastic, leading to a stress response that is nonlocal in time, the stress response of all fluids must also be regarded as being spatially nonlocal. Evidence for such viscoelastic behaviour has been seen in the velocity autocorrelation function [Alder 1967], in the neutron-scattering function [Alley 1983b] and in the transverse current autocorrelation function [Alley 1983b, Levesque 1973, Levesque 1987]. More recently, Todd *et al.* have shown that in all but the simplest flows (e.g. planar Couette and Poiseuille flows) and for velocity fields with high gradients in the strain rate over the width of the real space viscosity kernel, nonlocality can play a significant role [Todd 2008b, Todd 2008a]. Because such systems no longer respond pointwise and instantaneously to fluctuations but nonlocally in time and space, the nonlocal viscosity kernel (or memory kernel) $\eta(\mathbf{r}-\mathbf{r}', t-t')$ relating stress to the strain rate is introduced. For a homogeneous fluid the nonlocal constitutive relation reads [Alley 1983a, Evans 1990]

$$P_{xy}(\mathbf{r},t) = -\int_{0}^{t}\int_{-\infty}^{\infty} \eta(\mathbf{r}-\mathbf{r}', t-t')\dot{\gamma}(\mathbf{r}',t')d\mathbf{r}'dt', \tag{1}$$

where $P_{xy}(\mathbf{r},t)$ represents the (x,y) off-diagonal component of the pressure tensor and $\dot{\gamma}(\mathbf{r},t)$ is the shear strain rate at position $\mathbf{r}$ and time t. In the situation where the strain rate is constant in time and only varies with respect to the spatial coordinate y, Eq. (1) is written as

$$P_{xy}(y) = -\int_{-\infty}^{\infty} \eta(y-y')\dot{\gamma}(y')dy'. \tag{2}$$

It was found by Todd *et al.* that for a quadratic velocity profile, the non-local constitutive equation reduces to a simple local expression due to the symmetry of the non-local viscosity kernel [Todd 2008a].

Generally, the viscosity kernel for a Newtonian fluid reduces to a Dirac delta function. In reciprocal space Eq. (2), can be expressed as

$$\tilde{P}_{xy}(k_y) = -\tilde{\eta}(k_y)\tilde{\dot{\gamma}}(k_y), \tag{3}$$

where k_y is the y component of the wavevector. Such a constitutive equation is expected to be necessary for the description of flows in highly confined systems, due to the large change in the strain rate with position in the vicinity of the wall [Travis 1997].

The memory function $\eta(\mathbf{r}-\mathbf{r}', t-t')$ is merely the Fourier-transformed generalized transport coefficient to real space $\mathbf{r}$ and time t [Boon 1980, Evans 1990]. The best available theoretical predictions of the wavevector dependent viscosity are based on mode-coupling theory and generalized Enskog theory [Leutheusser 1982a, Leutheusser 1982b, Yip 1982]. However, these theories do not quantitatively agree with data obtained via computer simulations [Alley 1983a]. The theoretical predictions focus on the transverse momentum density autocorrelation function, which is found by an iterative numerical solution of a system of nonlinear equations. Consequently, the theories do not result in analytical expressions for the correlation functions or the wavevector dependent transport coefficients, which are the focus of the present study. More recently, a modified collective mode approach has been successfully applied by Omelyan *et al.* [Omelyan 2005] to the TIP4 model of water. Unlike other semi-phenomenological approaches used to describe the wavevector dependence of the viscosity for TIP4P and SPC/E models of water by Bertolini *et al.* [Bertolini 1995] and Palmer [Palmer 1994], Omelyan *et al.* reproduced the reciprocal space kernel using a relatively small number of modes.

Despite the fact that Alley and Alder [Alley 1983a] computed the generalized transport coefficients for hard spheres back in the early 1980s, the first serious attempt to study the nonlocal viscosity of confined fluids was made by Zhang *et al.* [Zhang 2004, Zhang 2005] and Cadusch *et al.* [Cadusch 2008] only two decades later. Zhang *et al.* model the (Couette and Poiseuille) flow by a nonlocal constitutive equation assuming that the viscosity kernel is independent of position i.e. $\eta(y, y-y') = \eta(y-y')$. This assumption of a homogeneous effective kernel is reasonable for relatively wide pores and low density fluids but it is limited in accuracy for the case of high densities and narrow confinement [Cadusch 2008]. Furthermore, since their analysis involves discrete Fourier transforms of the simulated data for the shear stress and strain rate, the domain restriction and the circular convolution inherent in the discrete Fourier transform methodology leads to singularities in the estimated kernel and a non-zero tail in the reciprocal space kernel for large wavevectors. In addition, the efforts to perform direct inversion to extract the kernel by discretizing the constitutive equation (assuming the viscosity kernel as a homogeneous function of relative separation) and selecting only those values that contribute to the shape of the kernel without attempting to Fourier transform the data led to a distortion of the shape of the true kernel.

An alternative to direct inversion of stress-strain rate data would be to determine the viscosity kernel independently for an unconfined, homogeneous fluid over an appropriate range of state points and then use the constitutive equation with appropriate boundary conditions to predict the flows for confined fluids. Following this idea, Hansen *et al.* [Hansen 2007] computed the nonlocal viscosity kernel for a simple monatomic system. Their preliminary results suggested that this work needs to be extended to cover a larger set of state points, potential energy functions and to extend the methodology to molecular fluids. We aimed this study to pursue this idea and to extend the work done by Hansen *et al.* [Hansen 2007] and understand fundamentally the spatially dependent transport properties for homogeneous molecular fluids.

We further expect that nonlocal transport phenomena would be relevant in shock waves [Alley 1983a, Holian 1980, Holian 1998, Reed 2006, Reed 2003], shear banding [Dhont 1999], flows of micellar solutions [Masselon 2008], suspensions of rigid fibers [Schiek 1995] and jammed or glassy systems [Goyon 2008] etc. Therefore such a work should be useful for a variety of applications in soft condensed matter.

Recently there has been a surge of interest in polymeric systems [Binder 1995, Kremer 2003]. Specifically, two large classes of materials such as polymeric chains, which are fundamental to both biology [Tegenfeldt 2004] and materials engineering, and hydrocarbons relevant to a wide range of chemical applications, are of special interest and therefore will be targeted in this work. We focus our attention on two relatively simple subclasses: on alkanes, in particular butane, and linear polymeric chains (similar to polyethylene). Our efforts will be focused on understanding how these chain systems behave in situations that commonly arise in nanofluidics.

In addition, polymeric materials are one of the most representative compounds that can exist in a glassy state and have attracted significant interest over the last decade. These model polymer melts are convenient systems for computer simulations of materials in metastable equilibrium near the glass transition temperature. Though the dynamics of such melts are generally explained by various theories such as mode coupling theory [Götze 1992], entropy theory [Gibbs 1955], free volume approach [Grest 1981] or the spin model [Binder 1986] the nature of the glass transition is still unclear.

In studies of a facilitated kinetic Ising model, Harrowell [Harrowell 1993] concluded that the glassy dynamics was the result of an increasing inhomogeneity in the spatial distribution of relaxation kinetics. This insight has proved a valuable approach to the analysis of structural relaxation in simple liquids [Hurley 1995, Hurley 1996] and it also provided a general framework with which to relate the range of glass behaviour [Perera 1996]. More recently, Widmer-Cooper *et al.* have shown that the localized low-frequency normal modes of a configuration in a supercooled liquid are causally correlated to the irreversible structural reorganization of the particles within this configuration [Widmer-Cooper 2009]. They also demonstrated that the spatial distribution of these soft local modes can persist in spite of significant particle reorganization. The consequence of these two results is that it is now feasible to construct a theory of relaxation length scales in glass-forming liquids without recourse to dynamics and to explicitly relate molecular properties to their collective relaxation [Widmer-Cooper 2008].

A body of literature exists on the viscoelastic properties and behaviour of the viscosity near the glass transition [Varnik 2002, Yamamoto 2002, Binder 2003, Wallace 2004]. There is much less information about the spatial dependence of viscosity for such systems [Furukawa 2009, Isobe 2009, Kim 2005, Mountain 1994]. Furukawa and Tanaka [Furukawa 2009], for instance, studied a different glass-forming liquid (a mixture of two atomic species) system and they did clearly confirmed the nonlocal nature of the viscous transport and linked it to the dynamic heterogeneity. There are, however, a few key differences between our results and Furukawa and Tanaka's work. For example, we use more robust empirical functions, a more extended set of stress and momentum density correlation function results and questioned in our analysis both the reciprocal and the real space viscosity kernels. Also, Kim and Keyes evaluated the wavevector dependent shear viscosity for a range of temperatures in a binary Lennard-Jones liquid system and observed a growing correlation length associated with a dynamically homogeneous domain [Kim 2005] . Isobe and Alder characterized the molasses tail (long time tail of the stress autocorrelation function) for a systems of elastic 2D hard discs and argued that the enhanced viscosity near solidification is due to a transitory existence of solid nuclei [Isobe 2009]. The transient existence of slow simultaneous unlocking mechanisms were considered as the origin of the molasses tail. In our study we address these questions by computing the viscosity kernel of a polymer melt as it is cooled down towards its glass transition temperature.

1 Theory and Methods

1.1 Microscopic mass and momentum density

A central problem in the study of fluids at molecular length and time scales is the computation of meaningful transport properties. While the macroscopic equations of motion for the densities of conserved quantities are well described by the classical Navier-Stokes-Fourier hydrodynamic theory [Evans 1990], we are mainly interested in the microscopic description of mass and momentum transfer. Therefore, in what follows, we will briefly introduce the microscopic expressions for the continuity equations.

In general, molecular hydrodynamic theories may be framed in atomic or molecular terms [Olmsted 1976a, Edberg 1987b, Allen 1984, Evans 1976]. Thus, it is important to understand the significant differences between two such formulations. Irving and Kirkwood [Irving 1950] derived in 1950 the microscopic expressions for the thermodynamic forces and fluxes in terms of ensemble averages. In fact the Irving-Kirkwood expression for the pressure tensor is the same expression as that derived using Gibbs' ensemble theory for a uniform fluid at equilibrium [Evans 1990]. The instantaneous expressions for the fluxes are usually preferred over ensemble based Irving-Kirkwood expressions. The reason is that the fluxes are based upon conservation laws and these laws are valid instantaneously for every member of the ensemble. They do not require ensemble averaging to be true. As ensemble averaging is very expensive in computer simulation time therefore it is rarely used in the calculation of system properties. As long as a system is ergodic, an ensemble average can always be replaced by a time average over a single phase-space trajectory.

We start with the macroscopic mass continuity equation governing the conservation of mass, which is

$$\frac{\partial \rho(\mathbf{r},t)}{\partial t} = -\nabla \cdot \Big[\rho(\mathbf{r},t)\mathbf{u}(\mathbf{r},t)\Big], \tag{1.1}$$

where $\rho(\mathbf{r},t)$ is the mass density and $\mathbf{u}(\mathbf{r},t)$ is the fluid streaming velocity at position $\mathbf{r}$ and time t. If we define the macroscopic momentum density as $\rho(\mathbf{r},t)\mathbf{u}(\mathbf{r},t)$ then, in the absence of external forces, we can write the macroscopic momentum continuity equation as

$$\frac{\partial \mathbf{J}(\mathbf{r},t)}{\partial t} = \frac{\partial[\rho(\mathbf{r},t)\mathbf{u}(\mathbf{r},t)]}{\partial t} = -\nabla \cdot \Big[\rho(\mathbf{r},t)\mathbf{u}(\mathbf{r},t)\mathbf{u}(\mathbf{r},t) + \mathsf{P}\Big], \tag{1.2}$$

where P is the pressure tensor.

In order to introduce the microscopic expressions for the continuity equations we need to define the microscopic mass and momentum density. The mass density can be defined either in the Schroedinger or Heisenberg representation. In the Schroedinger representation

$$\rho(\mathbf{r},t) = -\int d\mathbf{\Gamma} f(\mathbf{\Gamma},t) \sum_{i=1}^{N} m_i \delta(\mathbf{r} - \mathbf{r}_i), \tag{1.3}$$

where m_i is the mass of the individual particle in the single component (e.g. monatomic) system, $\mathbf{\Gamma}$ is the phase space vector and $f(\mathbf{\Gamma},t)$ is the N-particle distribution function in the phase space.

Alternatively, we can calculate the value at time t by following the mass $\sum_{i=1}^{N} m_i \delta(\mathbf{r} - \mathbf{r}_i)$, as it changes along a single trajectory in phase space. The mass density can then be calculated by summing the values of mass $\sum_{i}^{N} m_i \delta[\mathbf{r} - \mathbf{r}_i(t)]$, with a weighting factor determined by the probability of starting from each initial phase $\mathbf{\Gamma}$. These probabilities are chosen from an initial distribution function $f(\mathbf{\Gamma}, 0)$. This is the so called the Heisenberg representation of mass density written as

$$\rho(\mathbf{r}, t) = \int d\mathbf{\Gamma} f(\mathbf{\Gamma}, 0) \sum_{i}^{N} m_i \delta[\mathbf{r} - \mathbf{r}_i(t)] = \Big\langle \sum_{i}^{N} m_i | \mathbf{r}_i(t) = \mathbf{r} \Big\rangle. \tag{1.4}$$

The microscopic momentum density, $\rho(\mathbf{r}, t)\mathbf{u}(\mathbf{r}, t)$ is defined similarly as

$$\rho(\mathbf{r}, t)\mathbf{u}(\mathbf{r}, t) = \int d\mathbf{\Gamma} f(\mathbf{\Gamma}, 0) \sum_{i}^{N} m_i \mathbf{v}_i \delta[\mathbf{r} - \mathbf{r}_i(t)] = \Big\langle \sum_{i}^{N} \mathbf{p}_i(t) | \mathbf{r}_i(t) = \mathbf{r} \Big\rangle, \tag{1.5}$$

where $\mathbf{v}_i$ is the velocity and $\mathbf{p}_i$ is the momentum of particle i. For a molecular fluid the atomic representation of the momentum density can be written as

$$\mathbf{J}^A(\mathbf{r}, t) = \rho_a(\mathbf{r}, t)\mathbf{v}(\mathbf{r}, t) = \sum_{i=1}^{N_m} \sum_{\alpha=1}^{N_s} m_{i\alpha} \mathbf{v}_{i\alpha}(t) \delta(\mathbf{r} - \mathbf{r}_{i\alpha}), \tag{1.6}$$

where the atomic mass density is defined as

$$\rho_a(\mathbf{r}, t) = \sum_{i=1}^{N_m} \sum_{\alpha=1}^{N_s} m_{i\alpha} \delta(\mathbf{r} - \mathbf{r}_{i\alpha}). \tag{1.7}$$

The inner summation extends over the N_s mass points in a molecule and the outer summation extends over the number of molecules N_m in the system. If all the particles have the same mass then the atomic number density is equal to the atomic mass density in reduced units.

If we define the Fourier transform of a function $f(r)$ as

$$\mathcal{F}[f(\mathbf{r})] = \tilde{f}(\mathbf{k}) = \int_{-\infty}^{\infty} e^{i\mathbf{k}\mathbf{r}} f(\mathbf{r}) d\mathbf{r}, \tag{1.8}$$

then we can write the reciprocal space instantaneous mass density of a single component system as

$$\tilde{\rho}(\mathbf{k}, t) = \int_{-\infty}^{\infty} \sum_{i=1}^{N} m_i \delta[\mathbf{r} - \mathbf{r}_i(t)] e^{i\mathbf{k}\cdot\mathbf{r}} d\mathbf{r} = \sum_{i=1}^{N} m_i e^{i\mathbf{k}\cdot\mathbf{r}_i(t)} \tag{1.9}$$

and instantaneous momentum density in reciprocal space as

$$\tilde{\mathbf{J}}(\mathbf{k}, t) = \int_{-\infty}^{\infty} \sum_{i=1}^{N} m_i \mathbf{v}_i \delta[\mathbf{r} - \mathbf{r}_i(t)] e^{i\mathbf{k}\cdot\mathbf{r}} d\mathbf{r} = \sum_{i=1}^{N} m_i \mathbf{v}_i e^{i\mathbf{k}\cdot\mathbf{r}_i(t)}. \tag{1.10}$$

For a molecular system, the Fourier transform of the momentum density in the atomic representation can now be rewritten as

$$\tilde{\mathbf{J}}^A(\mathbf{k},t) = \sum_{i=1}^{N_m}\sum_{\alpha=1}^{N_s} m_{i\alpha}\mathbf{v}_{i\alpha}(t)e^{i\mathbf{k}\cdot\mathbf{r}_{i\alpha}}, \tag{1.11}$$

and the the transformed atomic mass density can be rewritten as

$$\tilde{\rho}_a(\mathbf{k},t) = \sum_{i=1}^{N_m}\sum_{\alpha=1}^{N_s} m_{i\alpha}e^{i\mathbf{k}\cdot\mathbf{r}_{i\alpha}}. \tag{1.12}$$

For molecules composed of N_s atoms we can define the mass of molecule i,

$$M_i = \sum_{\alpha=1}^{N_s} m_{i\alpha}, \tag{1.13}$$

the position of the molecular center of mass as

$$\mathbf{r}_i = \sum_{\alpha=1}^{N_s} m_{i\alpha}\mathbf{r}_{i\alpha}/M_i, \tag{1.14}$$

the position of site α of molecule i relative to the center of mass of molecule i as

$$\mathbf{R}_{i\alpha} = \mathbf{r}_{i\alpha} - \mathbf{r}_i, \tag{1.15}$$

and the center of mass momentum of the molecule as

$$\mathbf{p}_i = \sum_{\alpha=1}^{N_s} \mathbf{p}_{i\alpha}. \tag{1.16}$$

This means that the atomic mass density can be written in reciprocal space as

$$\tilde{\rho}_a(\mathbf{k},t) = \sum_{i=1}^{N_m}\sum_{\alpha=1}^{N_s} m_{i\alpha}e^{i\mathbf{k}\cdot(\mathbf{r}_i+\mathbf{R}_{i\alpha})}. \tag{1.17}$$

The molecular mass density is then

$$\tilde{\rho}_m(\mathbf{k},t) = \sum_{i=1}^{N_m} M_i e^{i\mathbf{k}\cdot\mathbf{r}_i} \tag{1.18}$$

in reciprocal space and

$$\rho_m(\mathbf{r},t) = \sum_{i=1}^{N_m} M_i\delta(\mathbf{r} - \mathbf{r}_i) \tag{1.19}$$

in real space, respectively.

We can expand the atomic momentum density about the molecular momentum density:

$$\tilde{\mathbf{J}}^A(\mathbf{k},t) = \sum_{i=1}^{N_m}\sum_{\alpha=1}^{N_s} m_{i\alpha}\mathbf{v}_{i\alpha}(1 + i\mathbf{k}\cdot\mathbf{R}_{i\alpha} + \ldots)e^{i\mathbf{k}\cdot\mathbf{r}_{i\alpha}}. \tag{1.20}$$

The Fourier transform of the momentum density in the molecular representation can then be written as

$$\tilde{\mathbf{J}}^M(\mathbf{k},t) = \sum_{i=1}^{N_m} M_i\mathbf{v}_i(t)e^{i\mathbf{k}\cdot\mathbf{r}_i}. \tag{1.21}$$

1.2 Wavevector dependent atomic and molecular pressure tensor

The pressure in a molecular liquid can be calculated using either of two expressions: the molecular or atomic pressure [Olmsted 1976a, Olmsted 1976b, Allen 1984, Edberg 1987b, Brown 1995, Travis 1995b]. The molecular pressure is the pressure calculated using the intermolecular forces and the molecular center of mass momenta. The atomic pressure on the other hand includes all intramolecular forces and constraint forces.

In order to derive the wavevector dependent molecular pressure tensor, we start with the Fourier transform of the momentum continuity equation excluding external body forces introduced previously in Eq. (1.2):

$$\frac{\partial}{\partial t}\Big[\widetilde{\rho\mathbf{v}}(\mathbf{k},t)\Big] = i\mathbf{k}\cdot\mathbf{P}(\mathbf{k},t) + i\mathbf{k}\cdot\Big[\widetilde{\rho\mathbf{v}\mathbf{v}}(\mathbf{k},t)\Big]. \tag{1.22}$$

If we recall that the microscopic expression of the real space momentum density for a molecular system was given in Eq. (1.6), the time derivative of its Fourier transform can be written as

$$\begin{aligned}\frac{\partial}{\partial t}\Big[\rho\mathbf{v}(\mathbf{k},t)\Big] &= \frac{\partial}{\partial t}\sum_{i=1}^{N_m}\sum_{\alpha=1}^{N_s} m_{i\alpha}\mathbf{v}_{i\alpha}e^{i\mathbf{k}\cdot\mathbf{r}_{i\alpha}} \\ &= \sum_{i=1}^{N_m}\sum_{\alpha=1}^{N_s} m_{i\alpha}(\dot{\mathbf{v}}_{i\alpha} + i\mathbf{k}\cdot\mathbf{v}_{i\alpha}\mathbf{v}_{i\alpha})e^{i\mathbf{k}\cdot\mathbf{r}_{i\alpha}} \\ &= \sum_{i=1}^{N_m}\sum_{\alpha=1}^{N_s} m_{i\alpha}\dot{\mathbf{v}}_{i\alpha}e^{i\mathbf{k}\cdot\mathbf{r}_{i\alpha}} + i\mathbf{k}\cdot\sum_{i=1}^{N_m}\sum_{\alpha=1}^{N_s} m_{i\alpha}\mathbf{v}_{i\alpha}\mathbf{v}_{i\alpha}e^{i\mathbf{k}\cdot\mathbf{r}_{i\alpha}}.\end{aligned} \tag{1.23}$$

Let us assume that Newton's equations of motion for a system of molecules is written as

$$m_{i\alpha}\dot{\mathbf{v}}_{i\alpha} = \mathbf{F}_{i\alpha} = \mathbf{F}^{\phi}_{i\alpha} + \mathbf{F}^{C}_{i\alpha} + \mathbf{F}^{D}_{i\alpha}, \tag{1.24}$$

with $\mathbf{F}^{\phi}_{i\alpha}$ being the contribution due to the atomic pair potential energy and $\mathbf{F}^{C}_{i\alpha}$ and $\mathbf{F}^{D}_{i\alpha}$ being the contribution of the internal molecular forces, such as the constraint and dihedral forces, respectively. Now, consider the first term involving the force due to the atomic pair potential energy in Eq. (1.24)

$$\begin{aligned}\sum_{i=1}^{N_m}\sum_{\alpha=1}^{N_s}\mathbf{F}_{i\alpha}^{\phi}e^{i\mathbf{k}\cdot\mathbf{r}_{i\alpha}} &= \sum_{i=1}^{N_m}\sum_{\alpha=1}^{N_s}\mathbf{F}_{i\alpha}^{\phi}e^{i\mathbf{k}\cdot(\mathbf{r}_i+\mathbf{R}_{i\alpha})} = \sum_{i=1}^{N_m}\sum_{\alpha=1}^{N_s}\mathbf{F}_{i\alpha}^{\phi}e^{i\mathbf{k}\cdot\mathbf{R}_{i\alpha}}e^{i\mathbf{k}\cdot\mathbf{r}_i} \\ &= \sum_{i=1}^{N_m}\sum_{\alpha=1}^{N_s}\mathbf{F}_{i\alpha}^{\phi}\Big(1+i\mathbf{k}\cdot\mathbf{R}_{i\alpha}+\frac{1}{2}[i\mathbf{k}\cdot\mathbf{R}_{i\alpha}]^2+\ldots\Big)e^{i\mathbf{k}\cdot\mathbf{r}_i} \\ &= \sum_{i=1}^{N_m}\sum_{\alpha=1}^{N_s}\mathbf{F}_{i\alpha}^{\phi}e^{i\mathbf{k}\cdot\mathbf{r}_i}+i\mathbf{k}\cdot\sum_{i=1}^{N_m}\sum_{\alpha=1}^{N_s}\mathbf{R}_{i\alpha}\mathbf{F}_{i\alpha}^{\phi}e^{i\mathbf{k}\cdot\mathbf{r}_i}+\ldots \qquad (1.25)\end{aligned}$$

Note that $\mathbf{r}_i$ and $\mathbf{R}_{i\alpha}$ are defined by Eqs. (1.15) and (1.14), respectively. The first term in Eq. (1.25) can be written as

$$\begin{aligned}\sum_{i=1}^{N_m}\sum_{\alpha=1}^{N_s}\mathbf{F}_{i\alpha}^{\phi}e^{i\mathbf{k}\cdot\mathbf{r}_{i\alpha}} &= \sum_{i=1}^{N_m}\sum_{\alpha=1}^{N_s}\sum_{j=1}^{N_m}\sum_{\beta=1}^{N_s}\mathbf{F}_{i\alpha j\beta}^{\phi}e^{i\mathbf{k}\cdot\mathbf{r}_i} \\ &= \sum_{j=1}^{N_m}\sum_{\beta=1}^{N_s}\sum_{i=1}^{N_m}\sum_{\alpha=1}^{N_s}\mathbf{F}_{j\beta i\alpha}^{\phi}e^{i\mathbf{k}\cdot\mathbf{r}_j} \\ &= -\sum_{i=1}^{N_m}\sum_{\alpha=1}^{N_s}\sum_{j=1}^{N_m}\sum_{\beta=1}^{N_s}\mathbf{F}_{i\alpha j\beta}^{\phi}e^{i\mathbf{k}\cdot\mathbf{r}_j}. \qquad (1.26)\end{aligned}$$

This allows us to express the configurational part of the wavevector dependent pressure tensor as:

$$\begin{aligned}\sum_{i=1}^{N_m}\sum_{\alpha=1}^{N_s}\mathbf{F}_{i\alpha}^{\phi}e^{i\mathbf{k}\cdot\mathbf{r}_{i\alpha}} &= \frac{1}{2}\sum_{i=1}^{N_m}\sum_{\alpha=1}^{N_s}\sum_{j=1}^{N_m}\sum_{\beta=1}^{N_s}\mathbf{F}_{i\alpha j\beta}^{\phi}\Big(e^{i\mathbf{k}\cdot\mathbf{r}_i}-e^{i\mathbf{k}\cdot\mathbf{r}_j}\Big) \\ &= -\frac{1}{2}\sum_{i=1}^{N_m}\sum_{\alpha=1}^{N_s}\sum_{j=1}^{N_m}\sum_{\beta=1}^{N_s}\mathbf{F}_{i\alpha j\beta}^{\phi}\Big(e^{i\mathbf{k}\cdot\mathbf{r}_{ij}}-1\Big)e^{i\mathbf{k}\cdot\mathbf{r}_i} \\ &= -\frac{1}{2}i\mathbf{k}\cdot\sum_{i=1}^{N_m}\sum_{\alpha=1}^{N_s}\sum_{j=1}^{N_m}\sum_{\beta=1}^{N_s}\mathbf{r}_{ij}\mathbf{F}_{i\alpha j\beta}^{\phi}\frac{\Big(e^{i\mathbf{k}\cdot\mathbf{r}_{ij}}-1\Big)}{i\mathbf{k}\cdot\mathbf{r}_{ij}}e^{i\mathbf{k}\cdot\mathbf{r}_i}. \qquad (1.27)\end{aligned}$$

We note that in some models, the pair force is set to zero for some sites; for example those that are joined to each other with a bond length or bond angle constraint or those sites which interact with each other via a dihedral interaction.

The contribution of the internal molecular forces, such as the constraint $\mathbf{F}_{i\alpha}^{C}$ and dihedral $\mathbf{F}_{i\alpha}^{D}$

forces, to the molecular pressure tensor is zero. This is proven by the following argument.

$$\begin{aligned}
\sum_{i=1}^{N_m}\sum_{\alpha=1}^{N_s}\mathbf{F}_{i\alpha}^{D}e^{i\mathbf{k}\cdot\mathbf{r}_{i\alpha}} &= \sum_{i=1}^{N_m}\sum_{\alpha=1}^{N_s}\mathbf{F}_{i\alpha}^{D}e^{i\mathbf{k}\cdot(\mathbf{r}_i+\mathbf{R}_{i\alpha})} = \sum_{i=1}^{N_m}\sum_{\alpha=1}^{N_s}\mathbf{F}_{i\alpha}^{D}e^{i\mathbf{k}\cdot\mathbf{R}_{i\alpha}}e^{i\mathbf{k}\cdot\mathbf{r}_i} \\
&= \sum_{i=1}^{N_m}\sum_{\alpha=1}^{N_s}\mathbf{F}_{i\alpha}^{D}(1+i\mathbf{k}\cdot\mathbf{R}_{i\alpha}+\frac{1}{2}[i\mathbf{k}\cdot\mathbf{R}_{i\alpha}]^2+\ldots)e^{i\mathbf{k}\cdot\mathbf{r}_i} \\
&= \sum_{i=1}^{N_m}\sum_{\alpha=1}^{N_s}\mathbf{F}_{i\alpha}^{D}e^{i\mathbf{k}\cdot\mathbf{r}_i} + i\mathbf{k}\cdot\sum_{i=1}^{N_m}\sum_{\alpha=1}^{N_s}\mathbf{R}_{i\alpha}\mathbf{F}_{i\alpha}^{D}e^{i\mathbf{k}\cdot\mathbf{r}_i}+\ldots \qquad (1.28)
\end{aligned}$$

The first term in Eq. (1.28) can be reduced further:

$$\sum_{i=1}^{N_m}\sum_{\alpha=1}^{N_s}\mathbf{F}_{i\alpha}^{D}e^{i\mathbf{k}\cdot\mathbf{r}_i} = \sum_{i=1}^{N_m}\Big(\sum_{\alpha=1}^{N_s}\mathbf{F}_{i\alpha}^{D}\Big)e^{i\mathbf{k}\cdot\mathbf{r}_i} = 0 \qquad (1.29)$$

because the sum of an internal force over all sites within a molecule is always zero. This also applies to the constraint forces.

Now consider the kinetic term of the derivative of the momentum density:

$$\begin{aligned}
\sum_{i=1}^{N_m}\sum_{\alpha=1}^{N_s}m_{i\alpha}\mathbf{v}_{i\alpha}\mathbf{v}_{i\alpha}e^{i\mathbf{k}\cdot\mathbf{r}_{i\alpha}} &= \sum_{i=1}^{N_m}\sum_{\alpha=1}^{N_s}m_{i\alpha}\Big[\mathbf{v}(\mathbf{r}_{i\alpha})+\mathbf{c}_{i\alpha}\Big]\Big[\mathbf{v}(\mathbf{r}_{i\alpha})+\mathbf{c}_{i\alpha}\Big]e^{i\mathbf{k}\cdot\mathbf{r}_{i\alpha}} \\
&= \sum_{i=1}^{N_m}\sum_{\alpha=1}^{N_s}m_{i\alpha}\Big[\mathbf{v}(\mathbf{r}_{i\alpha})\mathbf{v}(\mathbf{r}_{i\alpha})+\mathbf{v}(\mathbf{r}_{i\alpha})\mathbf{c}_{i\alpha} \\
&\quad +\mathbf{c}_{i\alpha}\mathbf{v}(\mathbf{r}_{i\alpha})+\mathbf{c}_{i\alpha}\mathbf{c}_{i\alpha}\Big]e^{i\mathbf{k}\cdot\mathbf{r}_{i\alpha}}. \qquad (1.30)
\end{aligned}$$

where $\mathbf{v}(\mathbf{r}_{i\alpha})$ and $\mathbf{c}_{i\alpha}$ is the streaming and thermal velocity, respectively.

The convective term of the momentum density equation shows that

$$\begin{aligned}
\tilde{\mathbf{J}}(\mathbf{k},t) &= F\Big\{(\rho\mathbf{v})\mathbf{v}\Big\} = F\Bigg\{\Big[\sum_{i=1}^{N_m}\sum_{\alpha=1}^{N_s}m_{i\alpha}\mathbf{v}_{i\alpha}\delta(\mathbf{r}-\mathbf{r}_{i\alpha})\Big]\mathbf{v}(\mathbf{r},t)\Bigg\} \\
&= \sum_{i=1}^{N_m}\sum_{\alpha=1}^{N_s}m_{i\alpha}\mathbf{v}_{i\alpha}\mathbf{v}(\mathbf{r}_{i\alpha},t)e^{i\mathbf{k}\cdot\mathbf{r}_{i\alpha}} \\
&= \sum_{i=1}^{N_m}m_i\Big[\mathbf{c}_{i\alpha}+\mathbf{v}(\mathbf{r}_{i\alpha},t)\Big]\mathbf{v}(\mathbf{r}_{i\alpha},t)e^{i\mathbf{k}\cdot\mathbf{r}_{i\alpha}} \\
&= \sum_{i=1}^{N_m}\sum_{\alpha=1}^{N_s}m_{i\alpha}\Big[\mathbf{c}_{i\alpha}\mathbf{v}(\mathbf{r}_{i\alpha},t)+\mathbf{v}(\mathbf{r}_{i\alpha},t)\mathbf{v}(\mathbf{r}_{i\alpha},t)\Big]e^{i\mathbf{k}\cdot\mathbf{r}_{i\alpha}}. \qquad (1.31)
\end{aligned}$$

But we also have

$$\widetilde{\rho\mathbf{v}\mathbf{v}}(\mathbf{k},t) = F\Big\{\mathbf{v}(\rho\mathbf{v})\Big\} = \sum_{i=1}^{N_m}\sum_{\alpha=1}^{N_s} m_{i\alpha}\Big[\mathbf{v}(\mathbf{r}_{i\alpha},t)\mathbf{c}_{i\alpha} + \mathbf{v}(\mathbf{r}_{i\alpha},t)\mathbf{v}(\mathbf{r}_{i\alpha},t)\Big]e^{i\mathbf{k}\cdot\mathbf{r}_{i\alpha}} \tag{1.32}$$

and

$$\widetilde{\rho\mathbf{v}\mathbf{v}}(\mathbf{k},t) = F\Big\{\rho(\mathbf{v}\mathbf{v})\Big\} = \sum_{i=1}^{N_m}\sum_{\alpha=1}^{N_s} m_{i\alpha}\mathbf{v}(\mathbf{r}_{i\alpha},t)\mathbf{v}(\mathbf{r}_{i\alpha},t)e^{i\mathbf{k}\cdot\mathbf{r}_{i\alpha}} \tag{1.33}$$

giving

$$\sum_{i=1}^{N_m}\sum_{\alpha=1}^{N_s} m_{i\alpha}\mathbf{v}(\mathbf{r}_{i\alpha},t)\mathbf{c}_{i\alpha}e^{i\mathbf{k}\cdot\mathbf{r}_{i\alpha}} = \sum_{i=1}^{N_m}\sum_{\alpha=1}^{N_s} m_{i\alpha}\mathbf{c}_{i\alpha}\mathbf{v}(\mathbf{r}_{i\alpha},t)e^{i\mathbf{k}\cdot\mathbf{r}_{i\alpha}} = 0. \tag{1.34}$$

Combining the kinetic part of the momentum density derivative and the convective term in the momentum equation, we find:

$$\begin{aligned}
& \sum_{i=1}^{N_m}\sum_{\alpha=1}^{N_s} m_{i\alpha}\Big[\mathbf{v}_{i\alpha}\mathbf{v}_{i\alpha}\Big]e^{i\mathbf{k}\cdot\mathbf{r}_{i\alpha}} - \rho\mathbf{v}\mathbf{v}(\mathbf{k},t) \\
= \quad & \sum_{i=1}^{N_m}\sum_{\alpha=1}^{N_s} m_{i\alpha}[\mathbf{v}(\mathbf{r}_{i\alpha})\mathbf{v}(\mathbf{r}_{i\alpha}) + \mathbf{v}(\mathbf{r}_{i\alpha})\mathbf{c}_{i\alpha} + \mathbf{c}_{i\alpha}\mathbf{v}(\mathbf{r}_{i\alpha}) + \mathbf{c}_{i\alpha}\mathbf{c}_{i\alpha}]e^{i\mathbf{k}\cdot\mathbf{r}_{i\alpha}} \\
- \quad & \sum_{i=1}^{N_m}\sum_{\alpha=1}^{N_s} m_{i\alpha}\mathbf{v}(\mathbf{r}_{i\alpha},t)\mathbf{v}(\mathbf{r}_{i\alpha},t)e^{i\mathbf{k}\cdot\mathbf{r}_{i\alpha}} \\
= \quad & \sum_{i=1}^{N_m}\sum_{\alpha=1}^{N_s} m_{i\alpha}\mathbf{c}_{i\alpha}\mathbf{c}_{i\alpha}e^{i\mathbf{k}\cdot\mathbf{r}_{i\alpha}}.
\end{aligned} \tag{1.35}$$

$$\tag{1.36}$$

To get this into the form required for the molecular pressure tensor, we must again separate the center of mass coordinates $\mathbf{r}_i$ from the coordinates relative to the centers of mass $\mathbf{R}_{i\alpha}$:

$$\begin{aligned}
\sum_{i=1}^{N_m}\sum_{\alpha=1}^{N_s} m_{i\alpha}\mathbf{c}_{i\alpha}\mathbf{c}_{i\alpha}e^{i\mathbf{k}\cdot\mathbf{r}_{i\alpha}} \quad = \quad & \sum_{i=1}^{N_m}\sum_{\alpha=1}^{N_s} m_{i\alpha}\mathbf{c}_{i\alpha}\mathbf{c}_{i\alpha}\Big(1 + i\mathbf{k}\cdot\mathbf{R}_{i\alpha} + \frac{1}{2}[i\mathbf{k}\cdot\mathbf{R}_{i\alpha}]^2 + \ldots\Big)e^{i\mathbf{k}\cdot\mathbf{r}_i} \\
= \quad & \sum_{i=1}^{N_m}\sum_{\alpha=1}^{N_s} m_{i\alpha}\mathbf{c}_{i\alpha}\mathbf{c}_{i\alpha}e^{i\mathbf{k}\cdot\mathbf{r}_i} \\
+ \quad & i\mathbf{k}\cdot\sum_{i=1}^{N_m}\sum_{\alpha=1}^{N_s} m_{i\alpha}\mathbf{R}_{i\alpha}\mathbf{c}_{i\alpha}\mathbf{c}_{i\alpha}e^{i\mathbf{k}\cdot\mathbf{r}_i} + \ldots
\end{aligned} \tag{1.37}$$

The first term contains the usual kinetic contribution to the molecular pressure tensor, plus another term representing the contribution of the relative peculiar velocity to the kinetic part of the pressure tensor

$$\begin{aligned}\sum_{i=1}^{N_m}\sum_{\alpha=1}^{N_s} m_{i\alpha}\mathbf{c}_{i\alpha}\mathbf{c}_{i\alpha}e^{i\mathbf{k}\cdot\mathbf{r}_i} &= \sum_{i=1}^{N_m}\sum_{\alpha=1}^{N_s} m_{i\alpha}(\mathbf{c}_i+\mathbf{C}_{i\alpha})(\mathbf{c}_i+\mathbf{C}_{i\alpha})e^{i\mathbf{k}\cdot\mathbf{r}_i} \\ &= \sum_{i=1}^{N_m} m_{i\alpha}\mathbf{c}_i\mathbf{c}_i e^{i\mathbf{k}\cdot\mathbf{r}_i} + \sum_{i=1}^{N_m}\sum_{\alpha=1}^{N_s} m_{i\alpha}\mathbf{C}_{i\alpha}\mathbf{C}_{i\alpha}e^{i\mathbf{k}\cdot\mathbf{r}_i}, \qquad (1.38)\end{aligned}$$

where $\mathbf{C}_{i\alpha}$ is the peculiar velocity relative to the center of mass. We have used the fact that

$$\sum_{i=1}^{N_m}\sum_{\alpha=1}^{N_s} m_{i\alpha}\mathbf{c}_i\mathbf{C}_{i\alpha}e^{i\mathbf{k}\cdot\mathbf{r}_i} = \sum_{i=1}^{N_m}\sum_{\alpha=1}^{N_s} \mathbf{c}_i m_{i\alpha}\mathbf{C}_{i\alpha}e^{i\mathbf{k}\cdot\mathbf{r}_i} = 0 \qquad (1.39)$$

because

$$\sum_{\alpha=1}^{N_s} m_{i\alpha}\mathbf{C}_{i\alpha} = \sum_{\alpha=1}^{N_s} m_{i\alpha}(\mathbf{c}_{i\alpha}-\mathbf{c}_i) = \sum_{\alpha=1}^{N_s} m_{i\alpha}\mathbf{c}_{i\alpha} - m_i\mathbf{c}_i = 0. \qquad (1.40)$$

Combining all of these results, i.e. Eqs. (1.23), (1.25), (1.27) and (1.37), we find that

$$\begin{aligned} i\mathbf{k}\cdot\tilde{\mathbf{P}}(\mathbf{k},t) &= \frac{\partial}{\partial t}\Big[\widetilde{\rho\mathbf{v}}(\mathbf{k},t)\Big] - i\mathbf{k}\cdot\Big[\widetilde{\rho\mathbf{v}\mathbf{v}}(\mathbf{k},t)\Big] \\ &= i\mathbf{k}\cdot\sum_{i=1}^{N_m} m_i\mathbf{c}_i\mathbf{c}_i e^{i\mathbf{k}\cdot\mathbf{r}_i} - \frac{1}{2}i\mathbf{k}\cdot\sum_{i=1}^{N_m}\sum_{\alpha=1}^{N_s}\sum_{j=1}^{N_m}\sum_{\beta=1}^{N_s}\mathbf{r}_{ij}\mathbf{F}^{\phi}_{i\alpha j\beta}\frac{\left(e^{i\mathbf{k}\cdot\mathbf{r}_{ij}}-1\right)}{i\mathbf{k}\cdot\mathbf{r}_{ij}}e^{i\mathbf{k}\cdot\mathbf{r}_i} \\ &+ i\mathbf{k}\cdot\sum_{i=1}^{N_m}\sum_{\alpha=1}^{N_s}\mathbf{R}_{i\alpha}\mathbf{F}^{\phi}_{i\alpha}e^{i\mathbf{k}\cdot\mathbf{r}_i} + i\mathbf{k}\cdot\sum_{i=1}^{N_m}\sum_{\alpha=1}^{N_s}\mathbf{R}_{i\alpha}\mathbf{F}^{D}_{i\alpha}e^{i\mathbf{k}\cdot\mathbf{r}_i} \\ &+ i\mathbf{k}\cdot\sum_{i=1}^{N_m}\sum_{\alpha=1}^{N_s} m\mathbf{C}_{i\alpha}\mathbf{C}_{i\alpha}e^{i\mathbf{k}\cdot\mathbf{r}_i} + O(k^2). \qquad (1.41)\end{aligned}$$

To within an arbitrary divergenceless quantity which we set to zero, this gives the wavevector dependent atomic pressure tensor as:

$$\begin{aligned} \tilde{\mathbf{P}}(\mathbf{k},t) &= \sum_{i=1}^{N_m} m_i\mathbf{c}_i\mathbf{c}_i e^{i\mathbf{k}\cdot\mathbf{r}_i} - \frac{1}{2}\sum_{i=1}^{N_m}\sum_{\alpha=1}^{N_s}\sum_{j=1}^{N_m}\sum_{\beta=1}^{N_s}\mathbf{r}_{ij}\mathbf{F}^{\phi}_{i\alpha j\beta}g(\mathbf{k}\cdot\mathbf{r}_{ij})e^{i\mathbf{k}\cdot\mathbf{r}_i} \\ &+ \sum_{i=1}^{N_m}\sum_{\alpha=1}^{N_s}\mathbf{R}_{i\alpha}\mathbf{F}^{\phi}_{i\alpha}e^{i\mathbf{k}\cdot\mathbf{r}_i} + \sum_{i=1}^{N_m}\sum_{\alpha=1}^{N_s}\mathbf{R}_{i\alpha}\mathbf{F}^{D}_{i\alpha}e^{i\mathbf{k}\cdot\mathbf{r}_i} \\ &+ \sum_{i=1}^{N_m}\sum_{\alpha=1}^{N_s} m\mathbf{C}_{i\alpha}\mathbf{C}_{i\alpha}e^{i\mathbf{k}\cdot\mathbf{r}_i} + O(k^2), \qquad (1.42)\end{aligned}$$

where $g(\mathbf{k}\cdot\mathbf{r}_{ij})$ is the Fourier transform of the Irving-Kirkwood O_{ij} operator [Irving 1950]

$$g(\mathbf{k}\cdot\mathbf{r}_{ij}) = \frac{(e^{i\mathbf{k}\cdot\mathbf{r}_{ij}}-1)}{i\mathbf{k}\cdot\mathbf{r}_{ij}} = \sum_{n=0}^{\infty}\frac{1}{(n+1)!}(i\mathbf{k}\cdot\mathbf{r}_{ij})^n. \tag{1.43}$$

The first line in Eq. (1.42) is the wavevector dependent molecular pressure tensor and the other terms can be rearranged into the second derivative of the mass dispersion tensor (the completely symmetric part) and the antisymmetric part of the molecular pressure tensor.

For a constrained diatomic fluid the wavevector dependent pressure tensor can be written in atomic representation as

$$\begin{aligned}\tilde{\mathbf{P}}^{A^{Diatomic}}(\mathbf{k},t) &= \sum_{i=1}^{N_m}\sum_{\alpha=1}^{2}\frac{\mathbf{p}_{i\alpha}\mathbf{p}_{i\alpha}}{m_{i\alpha}}e^{i\mathbf{k}\cdot\mathbf{r}_{i\alpha}} \\ &- \frac{1}{2}\sum_{i=1}^{N_m}\sum_{\alpha=1}^{2}\sum_{j\neq i}^{N_m}\sum_{\beta=1}^{2}\mathbf{r}_{i\alpha j\beta}\mathbf{F}_{i\alpha j\beta}g(\mathbf{k}\cdot\mathbf{r}_{i\alpha j\beta})e^{i\mathbf{k}\cdot\mathbf{r}_{i\alpha j\beta}} \\ &+ \sum_{i=1}^{N_m}\sum_{\alpha=1}^{2}\mathbf{r}_{i\alpha}\mathbf{F}_{i\alpha}^{C}g(\mathbf{k}\cdot\mathbf{r}_{i\alpha})e^{i\mathbf{k}\cdot\mathbf{r}_{i\alpha}}\end{aligned} \tag{1.44}$$

where $\mathbf{F}_{i\alpha j\beta}$ is the LJ force acting on site α of molecule i due to site β of molecule j, and $\mathbf{F}_{i\alpha}^{C}$ is the bond constraint force on site α of molecule i. $\mathbf{r}_{i\alpha j\beta} = \mathbf{r}_{j\beta} - \mathbf{r}_{i\alpha}$ is the minimum image separation of site α of molecule i from site β of molecule j. $g(\mathbf{k}\cdot\mathbf{r}_{i\alpha j\beta}) = (e^{i\mathbf{k}\cdot\mathbf{r}_{i\alpha j\beta}}-1)/i\mathbf{k}\cdot\mathbf{r}_{i\alpha j\beta}$ and $g(\mathbf{k}\cdot\mathbf{r}_{i\alpha}) = (e^{i\mathbf{k}\cdot\mathbf{r}_{i\alpha}}-1)/i\mathbf{k}\cdot\mathbf{r}_{i\alpha}$.

The wavevector dependent atomic pressure tensor for a polymer system composed of N_m molecules and N_s sites per molecule is defined as

$$\begin{aligned}\tilde{\mathbf{P}}^{A^{FJC/FENE}}(\mathbf{k},t) &= \sum_{i=1}^{N_m}\sum_{\alpha=1}^{N_s}\frac{\mathbf{p}_{i\alpha}\mathbf{p}_{i\alpha}}{m_{i\alpha}}e^{i\mathbf{k}\cdot\mathbf{r}_{i\alpha}} \\ &- \frac{1}{2}\sum_{i=1}^{N_m}\sum_{\alpha=1}^{N_s}\sum_{j\neq i}^{N_m}\sum_{\beta=1}^{N_s}\mathbf{r}_{i\alpha j\beta}\mathbf{F}_{i\alpha j\beta}g(i\mathbf{k}\cdot\mathbf{r}_{i\alpha j\beta})e^{i\mathbf{k}\cdot\mathbf{r}_{i\alpha j\beta}} \\ &- \sum_{i=1}^{N_m}\sum_{\alpha=1}^{N_s-2}\sum_{\beta=\alpha+2}^{N_s}\mathbf{r}_{i\alpha i\beta}\mathbf{F}_{i\alpha i\beta}g(i\mathbf{k}\cdot\mathbf{r}_{i\alpha i\beta})e^{i\mathbf{k}\cdot\mathbf{r}_{i\alpha i\beta}} \\ &+ \sum_{i=1}^{N_m}\sum_{\alpha=1}^{N_s}\mathbf{r}_{i\alpha}\mathbf{F}_{i\alpha}^{C/FENE}g(i\mathbf{k}\cdot\mathbf{r}_{i\alpha})e^{i\mathbf{k}\cdot\mathbf{r}_{i\alpha}}.\end{aligned} \tag{1.45}$$

$\mathbf{F}_{i\alpha j\beta}$ is the LJ force acting on site α of molecule i due to site β of molecule j and $\mathbf{F}_{i\alpha}^{C/FENE}$ is either the constraint force for freely jointed chains (FJC) or the bond force for finite extensible nonlinear elastic chains (FENE) on site α of molecule i. $\mathbf{r}_{i\alpha j\beta} = (\mathbf{r}_{j\beta} - \mathbf{r}_{i\alpha})_{min}$ is the minimum image separation of site α of molecule i from site β of molecule j. $g(x) = (e^x - 1)/x = \sum_{n=0}^{\infty}(x)^n/(n+1)!$, with $x = i\mathbf{k}\cdot\mathbf{r}_{i\alpha j\beta}$, $x = i\mathbf{k}\cdot\mathbf{r}_{i\alpha i\beta}$ and $x = i\mathbf{k}\cdot\mathbf{r}_{i\alpha}$, respectively.

For model butane, a torsional or dihedral force component $\mathbf{F}^D$ should be also included in the pressure tensor, so that

$$\begin{aligned}
\tilde{\mathsf{P}}^{A^{Butane}}(\mathbf{k},t) &= \sum_{i=1}^{N_m}\sum_{\alpha=1}^{N_s}\frac{\mathbf{p}_{i\alpha}\mathbf{p}_{i\alpha}}{m_{i\alpha}}e^{i\mathbf{k}\cdot\mathbf{r}_{i\alpha}} \\
&- \frac{1}{2}\sum_{i=1}^{N_m}\sum_{\alpha=1}^{N_s}\sum_{j\neq i}^{N_m}\sum_{\beta=1}^{N_s}\mathbf{r}_{i\alpha j\beta}\mathbf{F}_{i\alpha j\beta}\,g(i\mathbf{k}\cdot\mathbf{r}_{i\alpha j\beta})e^{i\mathbf{k}\cdot\mathbf{r}_{i\alpha j\beta}} \\
&+ \sum_{i=1}^{N_m}\sum_{\alpha=1}^{N_s}\mathbf{r}_{i\alpha}\mathbf{F}_{i\alpha}^{D}\,g(\mathbf{k}\cdot\mathbf{r}_{i\alpha})e^{i\mathbf{k}\cdot\mathbf{r}_{i\alpha}} \\
&+ \sum_{i=1}^{N_m}\sum_{\alpha=1}^{N_s}\mathbf{r}_{i\alpha}\mathbf{F}_{i\alpha}^{C}\,g(\mathbf{k}\cdot\mathbf{r}_{i\alpha})e^{i\mathbf{k}\cdot\mathbf{r}_{i\alpha}},
\end{aligned} \tag{1.46}$$

where $\mathbf{F}_{i\alpha}^{C}$ is the intramolecular constraint forces.

The pressure tensor in the molecular representation is defined for all the systems as

$$\begin{aligned}
\tilde{\mathsf{P}}^{M}(\mathbf{k},t) &= \sum_{i=1}^{N_m}\frac{\mathbf{p}_{i}\mathbf{p}_{i}}{M_{i}}e^{i\mathbf{k}\cdot\mathbf{r}_{i}} \\
&- \frac{1}{2}\sum_{i=1}^{N_m}\sum_{j\neq i}^{N_m}\mathbf{r}_{ij}\mathbf{F}_{ij}^{inter}\,g(i\mathbf{k}\cdot\mathbf{r}_{ij})e^{i\mathbf{k}\cdot\mathbf{r}_{ij}}
\end{aligned} \tag{1.47}$$

where, $\mathbf{F}_{ij}^{inter}$ represents the intermolecular force. $\mathbf{r}_{ij} = \mathbf{r}_j - \mathbf{r}_i$ is the minimum image separation of the center of mass of molecule i from the center of mass of molecule j. The momenta appearing in these equations, $\mathbf{p}_{i\alpha}$, $\mathbf{p}_i$, are the momenta appearing in the respective atomic and molecular equations of motion which are introduced in Section 2.

1.3 Wavevector and frequency dependent viscosity

In what follows we present expressions for the wave-vector and frequency dependent viscosities derived only for the atomic representation. Because the molecular stress tensor is not symmetric instantaneously the formulation of correlation function expressions is much more complex and will not be considered in this review.

The complex wavevector and frequency dependent viscosity, $\eta(\mathbf{k},\omega)$, can be evaluated by using three different expressions in terms of (a) the Fourier-Laplace transform of the transverse momentum density ACF, $C_{\perp}(\mathbf{k},t)$, (b) the Fourier-Laplace transform of the symmetric traceless stress tensor ACF, $N(\mathbf{k},t)$, and (c) the Fourier-Laplace transform of a generalized mean square displacement of the transverse momentum density. The Green-Kubo and Einstein relations can be derived as limiting cases of these expressions. The methodology for the derivation of these expressions has been previously described by [Evans 1990, Daivis 2004].

Here we give an overview of the first two [(a) and (b)] expressions of the wavevector and frequency dependent viscosity. The third expression in terms of the Fourier-Laplace transform of a generalized mean square displacement of the transverse momentum density (c) is not discussed as it is not useful in computer simulations of periodic systems, because it cannot be written in a convenient, directly calculable form for zero wavevector [Daivis 2004].

The wavevector and frequency dependent viscosity in terms of the transverse momentum density ACF and the stress ACF are very similar to the corresponding expressions for the self-diffusion coefficient [Evans 1990, Evans 1983, Evans 1981a, Evans 1981b, Evans 1980], and the derivations of these types of expression proceed in a similar sequence of steps for all of the transport coefficients [Hansen 1986].

For an aperiodic fluidic system with zero average streaming velocity, the Fourier transform of the continuity equation for the momentum density , Eq. (1.22), reduces to

$$\frac{\partial}{\partial t}\tilde{\mathbf{J}}(\mathbf{k},t) = i\mathbf{k}\cdot\tilde{\mathbf{P}}(\mathbf{k},t). \tag{1.48}$$

The pressure tensor in Eq. (1.48) can be decomposed into its isotropic, traceless symmetric and antisymmetric parts. For an atomic fluid with central forces, the antisymmetric part is zero [Evans 1990].

If we set the wavevector $(0,k_y,0)$ in reciprocal space and let J_x be the component of the momentum density in the *x* direction, and use the fact that

$$\dot{\gamma}(k_y,t) = -ik_y\tilde{u}_x(k_y,t) = -\frac{ik_y}{\rho}\tilde{J}_x(k_y,t), \tag{1.49}$$

by inserting the generalized constitutive relation for the shear viscosity Eq. (3), we find

$$\frac{\partial}{\partial t}\tilde{J}_x(k_y,t) = -ik_y\int\limits_0^\infty \tilde{\eta}(k_y,t-t')\tilde{\dot{\gamma}}(k_y,t')dt'. \tag{1.50}$$

We can rewrite Eq. (1.50) as

$$\frac{\partial}{\partial t}\tilde{J}_x(k_y,t) = -\frac{k_y^2}{\rho}\int\limits_0^\infty \tilde{\eta}(k_y,t-t')\tilde{J}_x(k_y,t')dt'. \tag{1.51}$$

By Fourier-Laplace transformation of both sides of Eq. (1.51) in time and using Onsager's regression hypothesis [Onsager 1931a, Onsager 1931b], multiply both sides by $\tilde{J}_x(k_y,0)$ and take the ensemble average, we can obtain the transverse momentum density ACF

$$\tilde{C}_\perp(k_y,\omega) = \frac{C_\perp(k_y,0)}{-i\omega + k_y^2\tilde{\eta}(k_y,\omega)/\rho}, \tag{1.52}$$

where ρ is the atomic mass density of the fluid and $C_\perp(k_y,t)$ is the equilibrium transverse current ACF defined as

$$\tilde{C}_\perp(k_y,\omega) = \Big\langle J_x(k_y,t)J_x(-k_y,0)\Big\rangle. \tag{1.53}$$

For the sake of simplicity of notation and consistency with the notation used in previous publications, we dropped the tilde sign over the correlation functions and kept the tilde notation over the Fourier-Laplace transformed correlation functions only.

The integral of the transverse momentum density ACF is given as:

$$I_{C_\perp}(k_y, t) = \int_0^t C_\perp(k_y, t')dt'. \tag{1.54}$$

The zero time value of $C_\perp(k_y, t = 0)$ for an atomic fluid in the thermodynamic limit is

$$C_\perp(k_y, 0) = \rho k_B T. \tag{1.55}$$

Note that $\mathbf{J}(\mathbf{r}, t) = \rho\mathbf{u}(\mathbf{r}, t)$, with ρ being the average equilibrium density, is only valid in linear order fluctuations at equilibrium. Also, we must note that the theoretical value of $C_\perp(k_y, t = 0) = \rho k_B T$ for an atomic fluid obtained from a Canonical ensemble average in the thermodynamic limit differs slightly from the theoretical value in the simulated isokinetic ensemble given for a molecular system by $C_\perp(k_y, t = 0) = \rho k_B T(1 - 4N_s N_m/3)$, because the total peculiar (i.e. thermal) kinetic energy and three components of the momenta are constants of the motion in our simulations. For a molecular fluid with constrained bonds, we must also account for the internal bond constraints in deriving a relationship between the zero time value of the atomic momentum density ACF and the temperature. This point is discussed further in the results sections. To ensure numerical consistency of our results, we use the simulated value of $C_\perp(k_y, t = 0)$ rather than Eq. (1.55) in all our calculations of the wavevector dependent viscosity.

Eq. (1.52) can be rewritten so that we obtain the expression for the wavevector and frequency dependent viscosity

$$\tilde{\eta}(k_y, \omega) = \frac{\rho}{k_y^2} \frac{C_\perp(k_y, 0) - i\omega\tilde{C}_\perp(k_y, \omega)}{\tilde{C}_\perp(k_y, \omega)}. \tag{1.56}$$

If we express the transverse momentum density ACF in terms of the stress ACF we obtain the viscosity in terms of a flux correlation function

$$N(k_y, t) = \frac{1}{V k_B T}\Big\langle P_{xy}(k_y, t) P_{xy}(k_y, 0)\Big\rangle, \tag{1.57}$$

and its Laplace transform

$$\tilde{N}(k_y, \omega) = \mathcal{L}\Big[N(k_y, t)\Big], \tag{1.58}$$

respectively, where the Fourier-Laplace transform (one-sided Fourier transform) is defined as

$$\mathcal{L}[f(t)] = \tilde{f}(\omega) = \int\limits_0^\infty f(t)e^{-i\omega t}dt. \tag{1.59}$$

The integral of the shear stress ACF can be written as

$$I_N(k_y, t) = \int_0^t N(k_y, t')dt' \tag{1.60}$$

which converges to the Green-Kubo viscosity for zero wavevector and to zero at non-zero wavevector.

Since [Evans 1990]

$$\frac{\partial^2}{\partial t^2}\langle J_x(k_y,t)J_x(-k_y,0)\rangle = \langle\frac{\partial}{\partial t}J_x(k_y,t)\frac{\partial}{\partial t}J_x(-k_y,0)\rangle = -k^2\langle P_{xy}(k_y,t)P_{xy}(-k_y,0)\rangle, \tag{1.61}$$

it follows that

$$(i\omega)^2 C_\perp(k_y,0) - i\omega C_\perp(k_y,0) = -k^2 V k_B T \tilde{N}(k_y,\omega). \tag{1.62}$$

Substituting Eq. (1.62) into Eq. (1.56) gives us the generalized shear viscosity in terms of the flux (shear stress) autocorrelation function

$$\tilde{\eta}(k_y,\omega) = \frac{\tilde{N}(k_y,\omega)}{C_\perp(k_y,t=0)/\rho k_B T - k^2\tilde{N}(k_y,\omega)/i\omega\rho}. \tag{1.63}$$

In the zero wavevector limit, a generalization of the Green-Kubo expression for the shear viscosity for an isotropic fluid allows the transverse momentum flux to be in an arbitrary direction rather than along a coordinate axis and can be written in terms of the stress tensor as [Hansen 1986, Daivis 1994]:

$$\eta = \frac{V}{10k_B T}\int_0^\infty \Big\langle \mathbf{P}^{os}(t) : \mathbf{P}^{os}(0)\Big\rangle dt \tag{1.64}$$

where the *os* superscript denotes the traceless symmetric part of the stress tensor $\mathbf{P}^{os}(t) = \frac{1}{2}[\mathbf{P}(t) + \mathbf{P}^T(t)] - \frac{1}{3}tr[\mathbf{P}(t)]\mathbf{1}$ and V is the simulation volume. Eq. (1.64) is valid for both atomic and molecular representations.

In the case $\omega \rightarrow 0$ and $k_y \rightarrow 0$, relation (1.63) reduces to the Green-Kubo formula [Hansen 1986]. All the non-zero wavevector integrals of the stress correlation functions, Eq. (1.57), converge to zero [Evans 1990]. By computing the integrals of the stress CFs one can computationally verify the zero values of the zero-frequency limit of the function $\tilde{N}(\mathbf{k},\omega)$ and thus demonstrate why neither substitution of $\omega = 0$ into Eq.(1.63) nor evaluation of Eq. (1.57) at non-zero wavevector yields the zero-frequency wavevector dependent viscosity. Therefore the relation in Eq. (1.56) must be used when non-zero wavevector viscosities are calculated. In order to obtain intensive correlation functions the expressions for N and $C_\perp$ must be normalized by the volume of the simulated system. We must also note that the number of degrees of freedom has not been taken explicitly into consideration in these equations. The correction terms for each simulated system are introduced in the next section.

2 Models and Simulations

2.1 Molecular dynamics

Molecular dynamics (MD) is a computational tool [Allen 1989, Rapaport 1995] that has contributed significantly to the fundamental understanding of fluid dynamics at atomic and molecular scales by providing information about processes not directly accessible by experimental studies. MD simulations model ensembles of interacting particles under specific internal and external forces. Given the initial coordinates and velocities of an ensemble of particles that interact under certain conditions, this method integrates the equations of motion numerically, providing new sets of coordinates and velocities at each integration time step. From the obtained particle trajectories one can calculate various global system properties as statistical averages.

Generally, MD simulation is a powerful tool allowing to solve the classical equations of motion of systems with many millions of atoms interacting with each other. It is particularly suited to study polymer-like systems due to the strict control of the internal motion. However, a fundamental approximation made in classical molecular dynamics is that one ignores explicit quantum effects and chooses an intermolecular potential which gives a sufficiently good approximation to these effects. If this approximation could not be made and significant quantum effects existed in the system then a quantum molecular dynamics scheme would perhaps be necessary [Car 1985, Cramer 2002, Jensen 2007].

In this work we simulate simple monatomic systems as well as more complex molecular systems such as alkanes and polymer melts. For this purpose we have used the FORTRAN90 modular molecular dynamics code developed by Peter Daivis at RMIT University. Some additional features were added due to the specificity of the simulated systems. The code also requires some ”tricks” of packing and pre-equilibration specific to dense systems of molecules. For computational efficiency we use an improved construction algorithm [Matin 2003] to build the cell neighbour list. Simulations have been carried out on the Swinburne University of Technology’s Supercomputer and the Australian National Computational Infrastructure’s supercomputer with an aggregated time of over 30 CPU years (equivalent to approximately 16 million CPUs running for 1 minute).

2.2 Monatomic systems

For the atomic fluids studied in this work, the atoms interact via a Lennard-Jones (LJ) or Weeks-Chandler-Andersen (WCA) potential energy function [Weeks 1971]. The LJ atoms have an interaction potential truncated at $r_c = 2.5\sigma$ and WCA atoms have an interaction potential truncated at $r_c = 2^{1/6}\sigma$ [Weeks 1971]. In general:

$$\Phi_{ij}(r_{ij}) = \begin{cases} 4\epsilon\left[\left(\frac{\sigma}{r_{ij}}\right)^{12} - \left(\frac{\sigma}{r_{ij}}\right)^{6}\right] - \Phi_c, & r_{ij} < r_c \\ 0, & r_{ij} \geq r_c \end{cases} \tag{2.1}$$

where r_{ij} is the interatomic separation, ϵ is the potential well depth, and σ is the value of r_{ij} at which the unshifted potential is zero. The shift Φ_c is the value of the unshifted potential at the cutoff $r_{ij} = r_c$, and is introduced to eliminate the discontinuity in the potential energy. At distances greater than the cutoff distance r_c, the potential is zero. The WCA potential is convenient in computations because it is short-ranged and therefore computationally undemanding, but still retains the essential physics, i.e. the repulsive interaction which dominates the transport phenomena we intend to study. The phase diagrams of Lennard-Jones fluids including the effect of truncation and shifting on the phase diagram can be found in the reference by Smit [Smit 1992].

2.3 Molecular systems

In molecular systems the distinction can be made between the intramolecular interactions, i.e. interactions between different sites of the same molecule, and intermolecular ones, i.e. those between all other atoms, which are irrespective of the topological constraints. The intramolecular potential energy comprises contributions from bond interactions, bond angle interactions and torsional interactions. The intermolecular potential can be divided into two-, three-, or other many-body interactions. In this study only pairwise interactions are taken into consideration.

The total potential energy in a system of molecules at position $\mathbf{r}_i$ can be calculated as the sum of intra- and intermolecular interactions:

$$U = U_{intra} + U_{inter}. \tag{2.2}$$

The total internal energy takes the form:

$$\Phi = \sum_{i=1}^{N_m} \sum_{\alpha}^{N_s} \frac{\mathbf{p}_{i\alpha}^2}{2m_{i\alpha}} + \sum_{i=1}^{N_m} \sum_{\alpha=1}^{N_s-2} \sum_{\beta=\alpha+2}^{N_s} U_{i\alpha j\beta} + \sum_{i=1}^{N_m-1} \sum_{\alpha}^{N_s} \sum_{j=i+1}^{N_m} \sum_{\beta=1}^{N_s} U_{i\alpha j\beta} \tag{2.3}$$

where the total energy is separated into its kinetic, intramolecular and intermolecular components. $U_{i\alpha j\beta}$ is the potential energy between atom α on molecule i and atom β on molecule j. The site indexing scheme used in the expression for the intramolecular potential energy given here is only valid for linear molecules [Matin 2000].

I. Diatomic model (liquid chlorine)

Our diatomic model of liquid chlorine is similar the the one used by Edberg *et al.* [Edberg 1987a], Hounkonnou *et al.* [Hounkonnou 1992], Travis *et al.* [Travis 1995b, Travis 1995a] and more recently by Matin *et al.* [Matin 2000, Matin 2001] to allow a direct comparison of our results with previous work. This model represents chlorine as a diatomic LJ molecule with $r_c = 2.5\sigma$ and a fixed bond length of 0.63σ. For an adequate representation of the properties of chlorine the LJ parameters are: $\sigma = 3.332$ Å and $\epsilon/k_B = 178.3$ K.

II. Model Butane

To simulate our butane molecules we have used the united atom model developed by Ryckaert and Bellemans [Ryckaert 1975, Ryckaert 1978] and then more extensively studied by [Rigby 1987, Takeuchi 1991, Roe 1994, Daivis 1994]. In this model each molecule is composed of $N_s = 4$ sites of mass 2.411×10^{-23} g which represent methyl groups. The distance between neighbouring sites is fixed to 1.53 Å and bond angles are fixed to $109.47°$ by a next-nearest-neighbour constraint. A dihedral potential that depends on the dihedral angle ϕ acts between each pair of methyl groups. We use a simple truncated cosine power series for the dihedral potential. We note here that while the semiflexible Ryckaert and Bellemans model reproduces the equilibrium properties of n-alkanes satisfactorily, it does not correctly generate all the transport coefficients [Edberg 1987b]. As we are interested in transport processes where the significant time scales are vastly longer than those for molecular vibrations, we are not considering the fully vibrational model with quadratic or Morse-type potentials for chemical bonds and bond angles. More sophisticated models have to be employed in order to get a better agreement with experiment [Toxvaerd 1990, Luo 1992b, Luo 1992a, Chynoweth 1991, Luo 1991, Martin 1998].

III. Polymer models

The molecular model that we have chosen to represent polymer molecules [Doi 1986, Doi 1996] is the freely jointed Lennard-Jones tangent chain (FJC) and bead-spring model also known as the finite extensible nonlinear elastic model (FENE).

III.A. Model FJC

An ideal chain (or freely-jointed chain) (FJC) is the simplest model to describe a polymer [Rapaport 1979, Smith 1996]. It only assumes a polymer as a random walk and neglects any kind of interactions among monomers. Although it is simple, its generality gives us some insights about the physics of polymers. In this ideal model, monomers are rigid rods of a fixed length, and their orientation is completely independent of the orientations and positions of neighbouring monomers, to the extent that two monomers can co-exist at the same place. In this very simple approach where no interactions between monomers are considered, the energy of the polymer is taken to be independent of its shape, which means that at thermodynamic equilibrium, all of its shape configurations are equally likely to occur as the polymer fluctuates in time, according to the Maxwell-Boltzmann distribution.

In our model (usually reffered as to freely-jointed tangent chain model [Johnson 1994]) each molecule consists of N_s sites of equal mass $m_{i\alpha}$ which interact via a truncated ($r_c = 2^{1/6}$) and shifted Lennard-Jones (LJ) interaction, Eq. (2.1), joined by rigidly constrained bonds of length $l = \sigma$. LJ interactions in this model can occur between any two different sites except those connected by a bond. In our simulations, for linear molecules with constrained bond length, we have used the Gaussian constraint method to calculate the constraint force [Morriss 1991, Edberg 1986, Edberg 1987b, Daivis 2007, Daivis 2003].

III.A. Model FENE

The FENE molecules that we simulate in this work consist of a linear chain of N_s beads interacting via pair potentials. Adjacent beads along the chain interact via a combined FENE spring potential, Eq. (2.4), and LJ potential Eq. (2.1). Beads which are not on the same molecule and beads which are on the same molecule but not adjacent interact just by the LJ potential. This model has been initially introduced by Bishop *et al.* [Bishop 1979] but gained in popularity only after the polymer simulations of Kremer and Grest [Kremer 1990]. In this model, the finite extensible nonlinear elastic potential is given as

$$\Phi_{ij}^{FENE}(r_{ij}) = \begin{cases} -\frac{1}{2}kR_0^2 \ln\left[1 - \left(\frac{r_{ij}}{R_0}\right)^2\right], & r_{ij} \le R_0 \\ +\infty, & r_{ij} \ge R_0, \end{cases} \tag{2.4}$$

where $k = 30\epsilon$ is the spring constant for the FENE bond, $R_0 = 1.5\sigma$ is the limit of the bond extension, and r_{ij} is the distance between particles i and j. The LJ potential cutoff distance was $r_c = 2.5\sigma$. The minimum of the bond potential along the chain occurs at a position $l_{min} \approx 0.97\sigma$ which is different from the minimum position $r_{min} \approx 1.13\sigma$ of the LJ potential. Also, the superposition of these two length scales prevents crystallization very efficiently, and the resulting structure of the melt and the corresponding glass resembles corresponding experimental data [Binder 1999, Kenna 1986].

The importance of the FENE potential over a Hookean potential is that a FENE bond cannot be extended beyond the fixed length R_0. The choice of coefficients k and R_0 are the values that have been used in a number of previous investigations using this potential [Bosko 2004a, Bosko 2004b, Bosko 2005, Kröger 2000, Kröger 1997, Kröger 1993]. It has been reported by the authors in these works that the molecules did not cross each other. Thus a key property of the polymers was correctly modelled. More recently, additional features in this model were introduced such as chain stiffness (besides the intrinsic stiffness induced by the excluded volume) [Faller 2001, Bulacu 2005].

2.4 Equations of motion

The equations of motion (EOM) can be written for a monatomic fluid in the isokinetic ensemble (at equilibrium) as [Evans 1990]:

$$\dot{\mathbf{r}}_i = \frac{\mathbf{p}_i}{m_i}, \quad \dot{\mathbf{p}}_i = \mathbf{F}_i - \zeta_A \mathbf{p}_i \tag{2.5}$$

where i denotes atom i. $\mathbf{r}_i$ is the position, $\mathbf{p}_i$ is the momentum and m_i is the mass of the designated atom. $\mathbf{F}_i$ is the force on atom i due to other atoms and ζ_A is the atomic thermostat multiplier. The thermostat multiplier is chosen so as to fix the kinetic temperature. As mentioned previously, we use the value of ζ_A that results from the application of Gauss' principle of least constraint to the imposition of constant kinetic temperature:

$$\zeta_A = \frac{\sum_{i=1}^{N} \mathbf{F}_i \cdot \mathbf{p}_i}{\sum_{i=1}^{N} \mathbf{p}_i^2}. \tag{2.6}$$

The atomic temperature T_A for a system of N_a atoms is defined as

$$T_A = \frac{1}{(dN_a - N_c)k_B} \left\langle \sum_{i=1}^{N_a} \frac{\mathbf{p}_i^2}{m_i} \right\rangle, \tag{2.7}$$

where d is the dimensionality of the atomic system and N_c is the number of constraints on the system (including constraints for conserved quantities).

The equations of motion for a molecular fluid can be given in either the atomic or molecular formalism. In fact, the molecular version of the homogeneous isothermal EOM with a molecular thermostat at equilibrium is similar to the atomic EOM with a molecular thermostat, provided that all of the relevant forces are included [Todd 2007].

The thermostatted molecular EOM for polymer melts are given by [Todd 2007]

$$\dot{\mathbf{r}}_{i\alpha} = \frac{\mathbf{p}_{i\alpha}}{m_{i\alpha}}, \quad \dot{\mathbf{p}}_{i\alpha} = \mathbf{F}_{i\alpha}^{LJ} + \mathbf{F}_{i\alpha}^{C/FENE} - \zeta_M \frac{m_{i\alpha}}{M_i}\mathbf{p}_i. \tag{2.8}$$

The force on a site is separated into three terms; $\mathbf{F}_{i\alpha}^{LJ}$ is the contribution due to the Lennard-Jones type interactions on site α of molecule i and $\mathbf{F}_{i\alpha}^{C/FENE}$ is either the constraint force or the bonding force. ζ_M is the molecular thermostat multiplier

$$\zeta_M = \frac{\sum_{i=1}^{N_m} \mathbf{F}_i \cdot \mathbf{p}_i / M_i}{\sum_{i=1}^{N_M} \mathbf{p}_i^2 / M_i} \tag{2.9}$$

and is derived from Gauss' principle of least constraint and acts to keep the molecular center of mass kinetic temperature T_M constant. The molecular temperature T_M is defined by

$$T_M = \frac{1}{(dN_m - N_c)k_B} \sum_{i=1}^{N_m} \frac{\mathbf{p}_i^2}{m_i} \tag{2.10}$$

A sparse matrix linear equation solver is also used for the FJC system [Golub 1996].

For butane the EOM are

$$\dot{\mathbf{r}}_{i\alpha} = \frac{\mathbf{p}_{i\alpha}}{m_{i\alpha}}, \quad \dot{\mathbf{p}}_{i\alpha} = \mathbf{F}_{i\alpha}^{T} + \mathbf{F}_{i\alpha}^{C} - \zeta_M \frac{m_{i\alpha}}{M_i}\mathbf{p}_i \tag{2.11}$$

where $\mathbf{F}_{i\alpha}^{T}$ represents the total force due to potential interactions and dihedral forces, and $\mathbf{F}_{i\alpha}^{C}$ represents the intramolecular constraint forces.

Following the equipartition principle, we will not distinguish between molecular and atomic temperature, but simply use T to indicate the temperature.

2.5 Integration of equations of motion

The time evolution of a set of N interacting particles is followed by integrating their EOM which are described by a set of N second-order differential equations in the Lagrangian representation or $2N$ first-order differential equations in the Hamiltonian approach. Time integration algorithm is based on finite difference methods, in which the time is discretized on a finite grid, the time step δt being the distance between consecutive points on the grid. A comparative description of various integration schemes such as Euler, Verlet, Leap-frog, Velocity Verlet, predictor-corrector, etc. can be found in [Cicotti 1986]. In this work the fifth-order Gear predictor-corrector algorithm is employed to integrate the EOM [Allen 1989, Gear 1971, Gear 1966, Rahman 1964] as it is efficient and accurate and relatively fast.

The main ingredient of the predictor-corrector algorithm is the corrector step, which accounts for a feedback mechanism. The feedback can damp the instabilities that might be introduced by the predictor step. This method provides both the positions and velocities of the atoms at the same time and it can be used to calculate forces, which depend explicitly on the velocity. This is in turn usually needed in algorithms which control temperature and pressure. It worth to mention, that interactions are evaluated using the results of the predictor step, but they are not re-evaluated again following the corrector step. The mean error, induced by the absence of force re-evaluation, is insignificant. Gear algorithms have very small energy fluctuations, but they are not reversible. Hence, there is always an energy drift [Haile 1983]. For large δt, if one needs stability in the total energy of the system, Velocity Verlet or operator-splitting integrators similar to those developed by Zhang [Zhang 1997] could be a better choice.

The predictor-corrector method consists of three steps:

1. *Predictor stage*: If the classical trajectory is continuous, then an estimate of the positions, velocities, momentum, accelerations etc. may be obtained by a Taylor series expansion about time t. We use

$$\mathbf{r}_i^n = \frac{1}{n!}(\delta t)^n\Big(\frac{d^n\mathbf{r}_i}{dt^n}\Big) \tag{2.12}$$

to represent the n^{th} order derivative term in the Taylor expansion of the position vector of particle i and

$$\mathbf{p}_i^n = \frac{1}{n!}(\delta t)^n\Big(\frac{d^n\mathbf{p}_i}{dt^n}\Big) \tag{2.13}$$

to represent the n^{th} order derivative term in the Taylor expansion of the momentum vector of particle i. The predicted position vector, momentum vector and their scaled time derivatives at time $t + \delta t$ are as follows,

$$\begin{pmatrix} \mathbf{r}_0^p(t+\delta t) \\ \mathbf{r}_1^p(t+\delta t) \\ \mathbf{r}_2^p(t+\delta t) \\ \mathbf{r}_3^p(t+\delta t) \\ \mathbf{r}_4^p(t+\delta t) \\ \mathbf{r}_5^p(t+\delta t) \end{pmatrix} = \begin{pmatrix} 1 & 1 & 1 & 1 & 1 & 1 \\ 0 & 1 & 2 & 3 & 4 & 5 \\ 0 & 0 & 1 & 3 & 6 & 10 \\ 0 & 0 & 0 & 1 & 4 & 10 \\ 0 & 0 & 0 & 0 & 1 & 5 \\ 0 & 0 & 0 & 0 & 0 & 1 \end{pmatrix} \times \begin{pmatrix} \mathbf{r}_0(t) \\ \mathbf{r}_1(t) \\ \mathbf{r}_2(t) \\ \mathbf{r}_3(t) \\ \mathbf{r}_4(t) \\ \mathbf{r}_5(t) \end{pmatrix} \tag{2.14}$$

$$\begin{pmatrix} \mathbf{p}_0^p(t+\delta t) \\ \mathbf{p}_1^p(t+\delta t) \\ \mathbf{p}_2^p(t+\delta t) \\ \mathbf{p}_3^p(t+\delta t) \\ \mathbf{p}_4^p(t+\delta t) \\ \mathbf{p}_5^p(t+\delta t) \end{pmatrix} = \begin{pmatrix} 1 & 1 & 1 & 1 & 1 & 1 \\ 0 & 1 & 2 & 3 & 4 & 5 \\ 0 & 0 & 1 & 3 & 6 & 10 \\ 0 & 0 & 0 & 1 & 4 & 10 \\ 0 & 0 & 0 & 0 & 1 & 5 \\ 0 & 0 & 0 & 0 & 0 & 1 \end{pmatrix} \times \begin{pmatrix} \mathbf{p}_0(t) \\ \mathbf{p}_1(t) \\ \mathbf{p}_2(t) \\ \mathbf{p}_3(t) \\ \mathbf{p}_4(t) \\ \mathbf{p}_5(t) \end{pmatrix} \tag{2.15}$$

2. *Force and acceleration*: The forces and accelerations are calculated from the predicted positions and then a correction term is calculated.

$$\mathbf{a}_i^c(t+\delta t) = \frac{1}{m}\mathbf{F}_i^c \tag{2.16}$$

The force is computed taking the gradient of the potential at the predicted positions. The resulting acceleration $\mathbf{a}_i^c(t+\delta t)$ will be different from the predicted acceleration $\mathbf{a}_i^p(t+\delta t)$. The difference between the two constitutes an error signal which is then used to calculate the corrected positions and their time derivatives.

$$\delta\mathbf{a}_i(t+\delta t) = \mathbf{a}_i^c(t+\delta t) - \mathbf{a}_i^p(t+\delta t) \tag{2.17}$$

3. *Corrector stage*: The error signal is used to correct positions and their derivatives.

$$\mathbf{r}_i^c(t+\delta t) = \mathbf{r}_i^p(t+\delta t) + \alpha\delta\mathbf{a}_i(t+\delta t) \tag{2.18}$$

α being the corrector coefficients which depend upon the order of the differential equation [Gear 1971, Gear 1966]:

$$\alpha = \begin{pmatrix} 3/16 \\ 251/360 \\ 1 \\ 11/18 \\ 1/6 \\ 1/60 \end{pmatrix} \tag{2.19}$$

The corrector stage is

$$\begin{pmatrix} \mathbf{r}_0^c(t+\delta t) \\ \mathbf{r}_1^c(t+\delta t) \\ \mathbf{r}_2^c(t+\delta t) \\ \mathbf{r}_3^c(t+\delta t) \\ \mathbf{r}_4^c(t+\delta t) \\ \mathbf{r}_5^c(t+\delta t) \end{pmatrix} = \begin{pmatrix} \mathbf{r}_0^p(t+\delta t) \\ \mathbf{r}_1^p(t+\delta t) \\ \mathbf{r}_2^p(t+\delta t) \\ \mathbf{r}_3^p(t+\delta t) \\ \mathbf{r}_4^p(t+\delta t) \\ \mathbf{r}_5^p(t+\delta t) \end{pmatrix} + \begin{pmatrix} \alpha_0(t) \\ \alpha_1(t) \\ \alpha_2(t) \\ \alpha_3(t) \\ \alpha_4(t) \\ \alpha_5(t) \end{pmatrix} \delta\mathbf{a}_i(t+\delta t) \tag{2.20}$$

A more detailed information on time integration algorithms can be found in [Allen 1989, Sadus 1999].

2.6 Lennard-Jones reduced units

In MD simulations the physical quantities are usually not expressed directly in international system of units because the numerical values would be either very small or very large and thus can lead to underflow or overflow as a result of floating-point operations, i.e. the values are not within a numerically manageable range [Allen 1989]. Therefore all quantities reported in this paper are reported in terms of reduced units and the simulations are themselves performed in these units. The reduced units are relative to the Lennard-Jones parameters. When using the Lennard-Jones potential, its parameters $\sigma = \epsilon = 1.0$ are the most appropriate units of length and energy. These, together with the mass $m = 1.0$ forms the MD units, while the rest of the physical quantities are expressed in reduced units. The conversion from real units to reduced units gives the reduced: length $r^* = r/\sigma$, velocity $v^* = v\sqrt{\epsilon/m}$, force $f^* = f\epsilon/\sigma$, density $\rho^* = \rho/\sigma^3$, temperature $T = k_B T/\epsilon$, time $t^* = t/(\sigma\sqrt{m/\epsilon})$, pressure $\mathsf{P}^* = \mathsf{P}(\sigma^3/\epsilon)$, strain-rate $\dot{\gamma}^* = \dot{\gamma}\sqrt{(m\sigma^2)/\epsilon}$ and viscosity $\eta^* = \eta\sqrt{\sigma^4/(m\epsilon)}$.

For the remainder of the paper the asterisk is dropped. In the case when simulations need to be compared with experiments, the LJ coefficients must be chosen to experimentally observed properties of the liquid.

3 Simple Fluids: Monatomics and Diatomics

3.1 Introduction

In this section[2] we focus on computing the spatially nonlocal viscosity kernel for monatomic and diatomic fluids over a wide range of wavevectors, state points and potential energy functions and thus extend the work done by Hansen *et al.* [Hansen 2007]. We are specifically interested in identifying functional forms that fit the reciprocal space kernel data. On the basis of these results, we are be able to assess the length scale (i.e. the width of the real space kernel) over which the governing generalized constitutive relation Eq. (2) must be used in these systems.

We will use the Edberg, Evans, and Morriss algorithm [Edberg 1986, Edberg 1987b, Daivis 1992] with an improved cell neighbour list construction algorithm [Matin 2003] to perform equilibrium simulations in the isokinetic molecular dynamics ensemble. The model used for the monatomic and diatomic systems has been given in Sections 2.2 and 2.3 and we summarize the most important parameters used in our simulations in Table 3.1.

Our simulations were carried out in a cubic box with periodic boundary conditions. The fifth-order Gear predictor corrector algorithm [Gear 1966, Gear 1971] with time step $\delta t = 0.001$ was employed to solve the equations of motion. The equations of motion and their integration method has also been given in Section 2.4 and Section 2.5.

All the systems were equilibrated for at least 10^6 time steps. The results from production runs were ensemble averaged over 14 runs, each of length 10^6 steps (i.e. a total of 1.4×10^7 time steps). The transverse momentum density ACFs were computed over at least 20 reduced time units and the stress ACFs were computed over at least 40 reduced time units. Both the transverse momentum density and stress ACFs were computed at wavevectors $k_{yn} = 2\pi n/L_y$ where mode number n is from 0 to 40 with increment 2 and $L_y = (N_a/\rho)^{1/3}$. L_y is the length of the simulation box. For the remainder of this section we drop the n index in k_{yn} for simplicity. The ACFs were Laplace transformed with respect to time using Filon's rule [Allen 1989]. We do not report the frequency dependent viscosities in this work. The wavevector dependent viscosities at zero frequency were calculated using Eqs. (1.56) and (1.63). Eq. (1.56) was used to obtain the non-zero wavevector and frequency dependent viscosities and Eq. (1.63) was used to obtain the zero wavevector viscosity.

The autocorrelation functions were evaluated for both 108 and 864 molecule systems in order to determine whether the results were system size dependent. There were no observed differences

---

[2] This section contains material reprinted with permission from R. M. Puscasu *et al.*, J. Phys.: Condens. Matter **22** (2010) 195105. Copyright 2010, Institute of Physics.

Tab. 3.1. Simulation details

	WCA	LJ	Chlorine
Site number density,ρ_a	$0.375, 0.480, 0.840$	0.840	1.088
Temperature, T	$0.765, 1.0$	$0.765, 1.0$	0.97
Number of atoms, N_a	$108, 2048, 6912$	$108, 2048, 6912$	$216, 1728$
Number of sites, N_s	1	1	2
Bond length, l	-	-	0.63
LJ cutoff, r_c	$2^{1/6}$	2.5	2.5

within the statistical errors in both monatomic and diatomic systems. We also note that in order to limit the enormous number of figures in this review, we do not display the results for the transverse momentum density and stress autocorrelation functions for monatomic systems. Nevertheless, the most relevant results for the transverse momentum density and stress autocorrelation functions are given for more complex systems in the following sections. However, we must mention that for monatomic systems both quantities (i.e. the transverse momentum density and stress ACFs) were in good agreement with those previously observed for Lennard-Jones monatomic liquids [Palmer 1994, Hansen 2007] and their running integrals have fully converged which suggests that the correlation functions have decayed to zero.

3.2 Reciprocal space viscosity kernel

The reciprocal space kernels for monatomic and diatomic fluids are plotted in Figs. (3.1) and (3.2). The error bars are smaller than the symbol sizes and therefore omitted. Generally the statistical reliability of reciprocal space kernel data increases as k_y increases.

Our zero wavevector, zero frequency viscosities for monatomic fluids agree well with those available in the literature. For the WCA system at the state point ($\rho_a = 0.375$, $T = 0.765$) we found $\eta_0 = 0.27 \pm 0.01$ which agrees with the results of Hansen *et al.* 0.273 [Hansen 2007, Alley 1983a], while at the state point ($\rho_a = 0.840$, $T = 1.0$) we found $\eta_0 = 2.29 \pm 0.07$, in agreement with the results of Matin *et al.* (2.1 ± 0.2) [Matin 2000]. For chlorine we found $\eta_0 = 6.89 \pm 0.32$, which agrees with the limiting values (6.7±0.4) of the shear and elongational viscosities at zero strain rate [Matin 2000].

It has been shown previously that numerous one parameter functions failed to capture the behaviour of the reciprocal space kernel data [Hansen 2007]. We therefore present the best fits with two or more fitting parameters. We have identified two functional forms that fit the data well: an N_G term Gaussian function

$$\tilde{\eta}_G(k_y) = \eta_0 \sum_j^{N_G} A_j \exp(-k_y^2/2\sigma_j^2) \qquad A_j, \sigma_j \in \mathbb{R}_+ \tag{3.1}$$

and a Lorentzian type function

$$\tilde{\eta}_L(k_y) = \frac{\eta_0}{1 + \alpha \left|k_y\right|^{\beta}} \qquad \alpha, \beta \in \mathbb{R}_+, \tag{3.2}$$

We present the best fits of the data to (i) a two-term Gaussian function with freely estimated amplitudes (i.e. unconstrained fitting) termed as $\tilde{\eta}_{G_2}$; (ii) to a two-term Gaussian function with interdependent amplitudes (i.e. constrained fitting $\sum_j^{N_G} A_j = 1$) given by Hansen *et al.* [Hansen 2007] and termed as $\tilde{\eta}_{G_{2H}}$; (iii) to a four-term Gaussian function with freely estimated amplitudes, termed as $\tilde{\eta}_{G_4}$ and (iv) to the Lorentzian type function, Eq. (3.2), termed as $\tilde{\eta}_L$.

In order to measure the magnitude of the residuals we use the residual standard deviation defined as

$$s_r = \sqrt{\sum_{n=1}^{n_s} r^2/(n_s - n_p)} \tag{3.3}$$

where n_s is the number of data points, n_p is the number of fitting parameters, and r is the residual [Peck 2008]. After an iterative curve fitting procedure the accurate estimation of η_0 was kept fixed allowing all other parameters in Eqs. (3.1) and (3.2) to be used as fitting parameters. In Table 3.2 we have listed the fitting parameters for monatomic and diatomic molecular fluids and compared to the previous results where possible.

A useful check of the fitting can be performed by calculating the total Gaussian amplitudes which should converge to the value of 1, Table 3.3.

The reciprocal space results presented in Fig. 3.1 for LJ and chlorine systems demonstrate that the four-term Gaussian function fits the data much better than the other two forms with a difference between the data and the fit of less than 0.5%, see Fig. 3.1(c). The two-term Gaussian $\tilde{\eta}_{G_{2H}}$ fits the kernel data better than the Lorentzian-type function in the low-k_y region, Fig. 3.1(a), which suggests a more Gaussian-like behaviour in the low-k_y region, a fact previously observed by Hansen *et. al* [Hansen 2007] for atomic fluids modeled with WCA potentials. Nevertheless the difference between the two-term Gaussian fit and the data is less than 2% which still makes

Tab. 3.2. Zero frequency, zero wavevector shear viscosity and fitted parameter values for monatomic and diatomic systems

		WCA	WCA	WCA	LJ	LJ	Chlorine
State Point	ρ_a	0.375	0.480	0.840	0.840	0.840	1.088
	T	0.765	0.765	1.000	0.765	1.0	0.97
System size	N_a		2048				1728
	η_0	0.265(0.273 [Hansen 2007])	0.392	2.290	2.810	2.650	6.889
2-term Gaussian, $A_2 = 1 - A_1$ Eq. (3.1)	A	0.189(0.440 [Hansen 2007])	0.309	0.155	0.093	0.107	0.407
	σ_1	12.48(4.750 [Hansen 2007])	6.916	8.122	10.04	9.088	5.377
	σ_2	2.116(1.376 [Hansen 2007])	1.835	2.592	2.778	2.759	1.236
	s_r	0.007(0.005 [Hansen 2007])	0.013	0.044	0.021	0.027	0.082
2-term Gaussian Eq. (3.1)	A_1	0.792	0.687	0.874	0.907	0.892	0.592
	A_2	0.174	0.254	0.155	0.094	0.106	0.407
	σ_1	2.245	2.113	2.592	2.776	2.765	1.237
	σ_2	13.36	7.745	8.124	10.02	9.127	5.377
	s_r	0.007	0.011	0.035	0.022	0.031	0.081
4-term Gaussian Eq. (3.1)	A_1	0.432	0.566	0.778	0.689	0.868	0.398
	A_2	0.394	0.248	0.118	0.190	0.047	0.538
	A_3	0.120	0.138	0.088	0.114	0.089	0.055
	A_4	0.056	0.047	0.017	0.017	0.020	0.008
	σ_1	3.228	2.826	2.950	2.709	2.814	4.355
	σ_2	1.261	0.821	0.651	2.709	0.145	1.155
	σ_3	8.165	6.973	8.496	7.037	7.628	10.46
	σ_4	15.19	14.74	23.66	24.94	19.99	37.56
	s_r	0.008	0.002	0.012	0.014	0.024	0.018
Lorentzian-type Eq. (3.2)	α	0.198(0.180 [Hansen 2007])	0.170	0.062	0.041	0.043	0.239
	β	1.562(1.662 [Hansen 2007])	1.715	2.326	2.602	2.572	1.667
	s_r	0.002(0.005 [Hansen 2007])	0.005	0.042	0.018	0.042	0.016

Tab. 3.3. Total amplitude for Gaussian functional form

		WCA			LJ		Chlorine
State Point	ρ_a	0.375	0.480	0.840	0.840	0.840	1.088
	T	0.765	0.765	1.000	0.765	1.0	0.97
2-term Gaussian	$\sum_{j=1}^{2} A$	0.966	0.941	1.029	1.001	0.998	0.999
4-term Gaussian	$\sum_{j=1}^{4} A$	1.002	0.999	1.001	1.010	1.024	0.999

$\tilde{\eta}_{G_{2H}}$ a good analytical three parameter approximation of the reciprocal space viscosity kernel.

The maximum difference between the Lorentzian-type fit and Gaussian fits are around 4% while the maximum difference between the Gaussian fits is around 2%, see Fig. 3.1(d). Essentially, this suggests that, when computing the real space kernels, the four-term Gaussian functional form is to be trusted. It is obvious that eight parameters in the four-term Gaussian make its use less convenient, but on the other hand the Gaussian function can analytically be inverse Fourier transformed while the inverse Fourier transform of the Lorentzian-type function can only

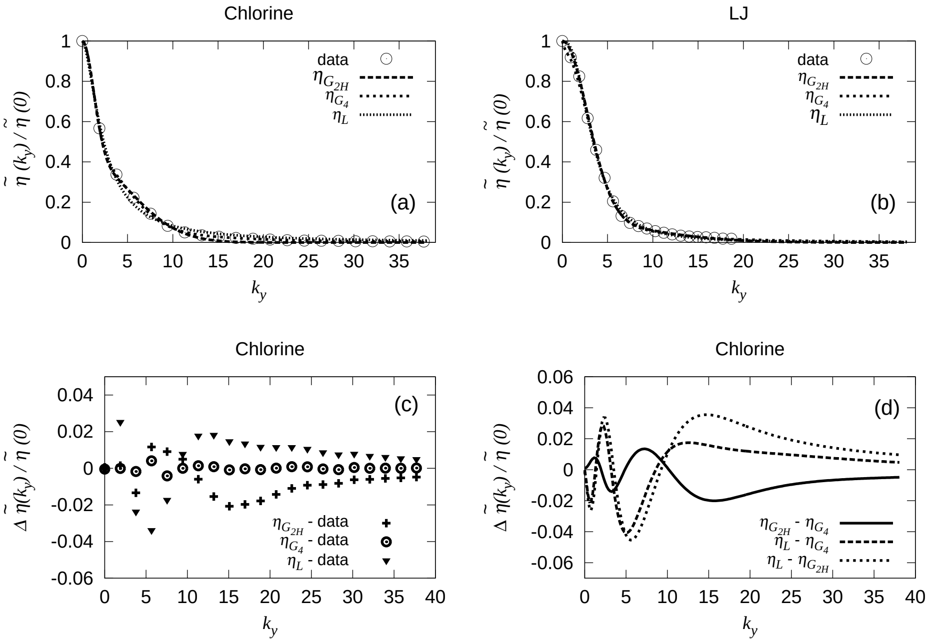

Fig. 3.1. Normalized kernel data, best fit of Eq. (3.1) with $N_G = 2$ and 4, and Eq. (3.2) and difference between the fits: (a) Best fits to normalized kernel for chlorine fluid ($\rho_a = 1.088$, $T = 0.97$, $N_a = 1728$); (b) Best fits to normalized kernel for LJ fluid ($\rho_a = 0.840$, $T = 1.0$, $N_a = 2048$); (c) Differences between the kernels and simulation data (a); (d) Differences between the fitted kernels (b).

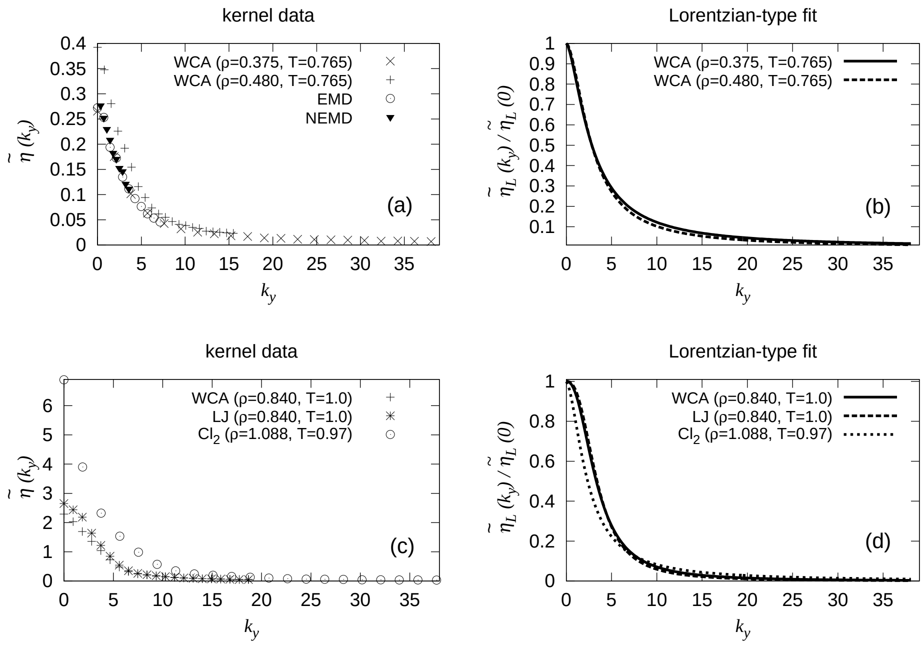

Fig. 3.2. Reciprocal-space kernels of monatomic and diatomic fluids: (a) Kernel data of a WCA fluid at two different densities ($T = 0.765$, $N_a = 2048$); (b) Best fit of normalized kernel data (a) to Lorentzian-type function Eq. (3.2); (c) Kernel data of a WCA fluid and LJ fluid at the same state point ($\rho_a = 0.840$, $T = 1.0$, $N_a = 2048$), Chlorine at ($\rho_a = 1.088$, $T = 0.97$, $N_a = 1728$); (d) Best fit of the normalized kernel data (c) to the Lorentzian-type function Eq. (3.2).

be evaluated numerically for general values of β.

Fig. 3.2(a) shows the kernel data for a WCA fluid at two different densities along with two sets of data published previously by Hansen *et al.* [Hansen 2007]. EMD is the set obtained from an equilibrium MD simulation at the same state point ($\rho_a = 0.375$, $T = 0.765$) and NEMD is the set obtained from a nonequilibrium MD simulation based on the sinusoidal transverse force (STF) method. An excellent agreement between both sets of data was found. Fig. 3.2(b) shows the normalized fit to Eq. (3.2).

The normalized kernels, Fig. 3.2(b), show a similar behavior for $k_n \leq 4$. Though the higher density kernel is slightly lower for $k_n \geq 4$ they show a similar limiting behavior. This effect was not seen by Hansen *et al.* due to lack of data for high wave vectors. Fig. 3.2(d) indicates that despite the difference between the interaction potentials, the results for LJ and WCA fluids are very close. This confirms that transport is dominated by repulsive interactions, rather than attractive. The sharper kernel for the diatomic system, Fig. 3.2(d), suggests a more Lorentzian-type behavior in the low wavevector region. It is also important to mention that even though the fitting parameters are significantly affected by temperature, the resulting kernels vary weakly over the range of temperatures chosen here. This was also observed by Hansen *et al.* for WCA monatomic fluids.

3.3 Real space viscosity kernel

The viscosity kernel in reciprocal space is an even function since it is symmetric about the origin; thus the the real space kernel is symmetric because the Fourier transform keeps the even properties of the function. This means that the viscosity kernel in real space can be found via an inverse Fourier cosine transform, $F_c^{-1}[\dots]$, of the viscosity kernel in reciprocal space. Since the integral is being computed over an interval symmetric about the origin (i.e. -∞ to +∞), the Fourier cosine transform simplifies to:

$$F_c^{-1}[\tilde{\eta}(k_y)] = \eta(y) = \sqrt{\frac{2}{\pi}} \int_0^{\infty} \tilde{\eta}(k_y)\cos(k_y y)dk_y. \tag{3.4}$$

The inverse Fourier cosine transform of the Gaussian function, Eq. (3.1), exists [Papoulis 1962] and it is even possible to obtain an analytical expression. For an N_G term Gaussian function the inverse Fourier cosine transform is

$$\eta_G(y) = \frac{\eta_0}{\sqrt{2\pi}} \sum_j^{N_G} A_j \sigma_j \exp[-(\sigma_j y)^2/2] \qquad A_j, \sigma_j \in \mathbb{R}_+. \tag{3.5}$$

Though the Lorentzian-type function given in Eq. (3.2) fulfills the criteria for having an inverse Fourier transform $\eta_L(y)$ (i.e. the function is absolutely integrable, square integrable and the function and its derivative are piecewise continuous), the integral in Eq. (3.4) is not readily obtained analytically in the general case. However, the integral can be evaluated numerically. In this work, a Simpson method has been employed for this purpose.

The real space kernels for atomic and diatomic fluids at zero frequency are presented in Figs. 3.3, 3.4 and 3.5. Fig. 3.3(a) shows the resulting kernels for chlorine and Fig. 3.3(b) shows the resulting kernels for a LJ fluid extracted from two-term and four-term Gaussian functions, Eq. (3.5), and inverse Fourier transform of Eq. (3.2). We find very little difference between the kernels obtained via two- and four-term Gaussians for these systems.

Figs. 3.3(c) and 3.3(d) show the differences between all three fits. It can be seen that there exists a significant difference (almost 25%) between the kernels extracted from Gaussian and Lorentzian type functions for small y. The discrepancy decreases rapidly as y increases and becomes approximately zero for $y \geq 1.5$. The width of the kernel for chlorine is roughly 4-6 atomic diameters, Fig. 3.3(a), and 3-5 atomic diameters for monatomic LJ and WCA fluids, Fig. 3.3(b).

For monatomic systems at relatively low densities ($\rho_a = 0.375 - 0.480$), the real space kernels are affected considerably by the functional form chosen to fit the reciprocal space kernel, Fig. 3.4. For instance, the equally weighted two-term Gaussian function, Fig. 3.4(a), distorts the real space kernels and predicts a noticeably higher $\eta(y = 0)$ value. As we increase the density, the discrepancy between Gaussian functions, as well as between Gaussian and Lorentzian-type functions, only partially reduces, Fig. 3.4(b,d). The width of the kernel for WCA fluids at low

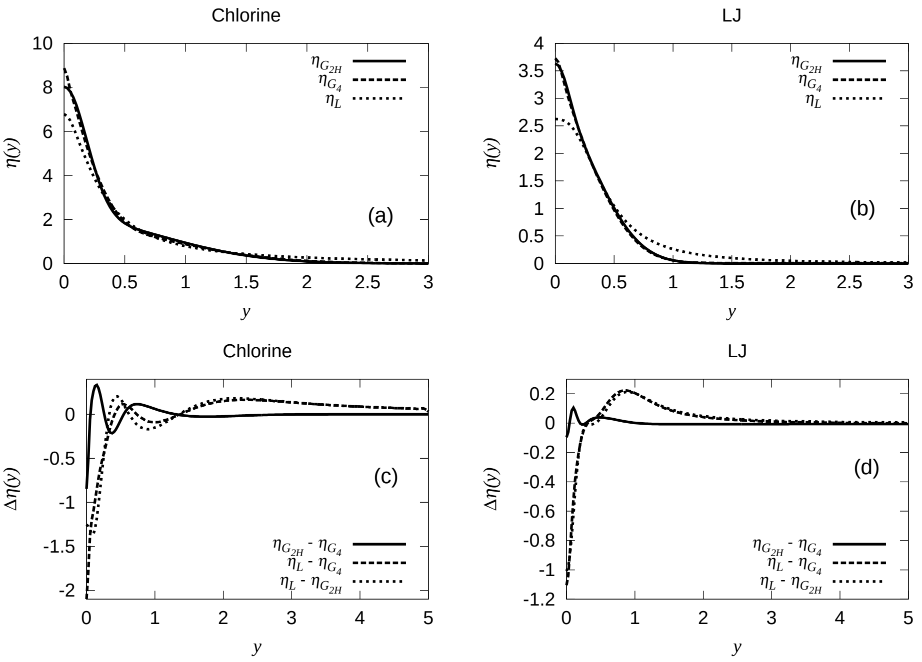

Fig. 3.3. Real space kernel of monatomic and diatomic fluids as predicted by Gaussian and Lorentzian fits of reciprocal space kernel data: (a) chlorine ($\rho_a = 1.088$, $T = 0.97$); (b) LJ ($\rho_a = 0.840$, $T = 1.0$); (c) Differences between the kernels shown in (a); (d) Differences between the kernels shown in (b).

density is roughly 2-4 atomic diameters.

In Figs. 3.5(a) and 3.5(b) we compare the unnormalized kernel data in y space extracted from four-term Gaussian and Lorentzian-type functional forms for all the simulated systems. Despite the fact that the difference between the reciprocal kernels is less than 4%, Fig. 3.1(d) (e.g. chlorine - dashed line), the kernels for the corresponding systems in real space look noticeably different (Figs. 3.5(a) and 3.5(b)), for all the systems (e.g. chlorine - dashed dotted line). However, the zero wavevector viscosities obtained from both functional forms are very close, with less than 2% error. We can determine the zero wavevector viscosities $\eta_0 = \eta(k = 0, \omega = 0)$ by integrating the real space kernel over y, and thus test our numerical analysis.

The zero wavevector viscosity η_0 obtained from a Gaussian function $\eta_G(y)$ is

$$\eta_0 = \int\limits_{-\infty}^{\infty} \eta_G(y)dy = \frac{\eta_0}{\sqrt{2\pi}} \int\limits_{-\infty}^{\infty} \Big\{ \sum_j^{N_G} A_j \sigma_j \exp[-(\sigma_j y)^2/2] \Big\} dy. \tag{3.6}$$

Since the general analytical expression for $\eta_L(y)$ does not exist [Hansen 2007] we evaluate the integral numerically and present the results from all functional forms in Table 3.4. A comparison of the viscosities in Table 3.4 with the simulated zero frequency zero wavevector shear viscosities

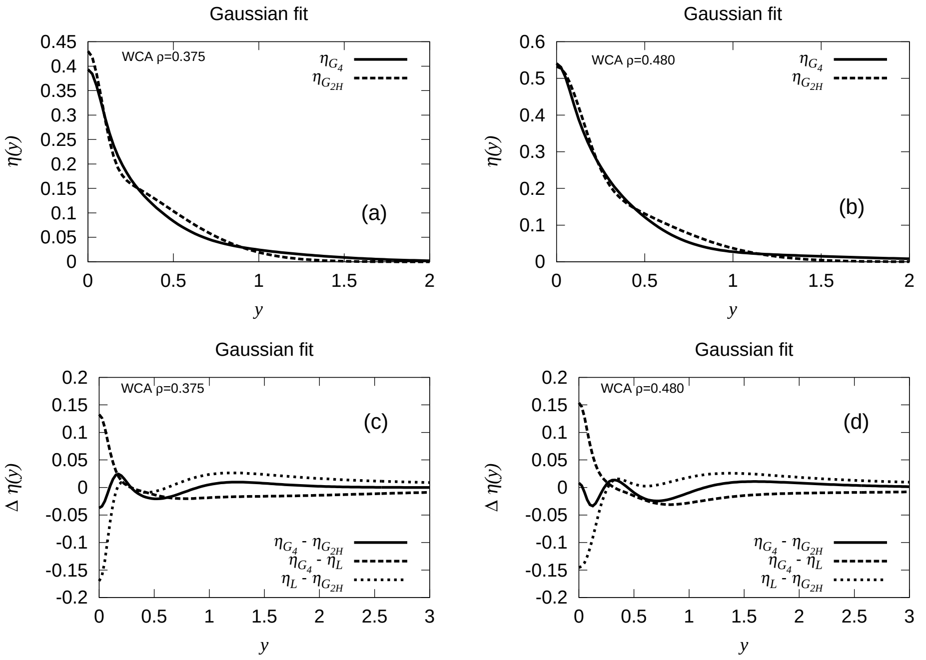

Fig. 3.4. Real space kernel of monatomic WCA fluids as predicted by Gaussian fits of the reciprocal space kernel data, Eq. (3.5): (a) Kernels obtained from two- and four-term Gaussian fits for a WCA fluid at $\rho_a = 0.375$ and $T = 0.765$; (b) Kernels obtained from two- and four-term Gaussian fits for a WCA fluid at $\rho_a = 0.480$ and $T = 0.765$; (c) Differences between the kernels for a WCA fluid at $\rho_a = 0.375$ and $T = 0.765$; (d) Differences between the kernels for a WCA fluid at $\rho_a = 0.480$ and $T = 0.765$.

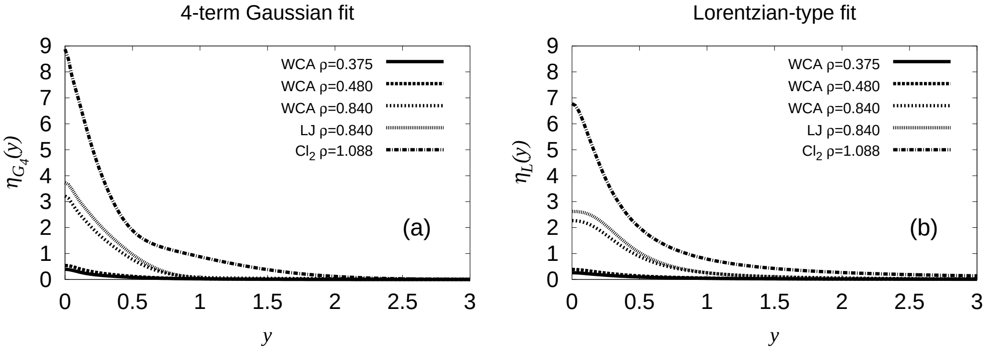

Fig. 3.5. Real space viscosity kernels of monatomic and diatomic fluids, WCA ($\rho_a = 0.375$, $T = 0.765$), WCA ($\rho_a = 0.480$, $T = 0.765$), WCA ($\rho_a = 0.840$, $T = 1.0$), LJ ($\rho_a = 0.840$, $T = 1.0$), chlorine ($\rho_a = 1.088$, $T = 0.97$): (a) Kernels obtained from the four-term Gaussian functional form Eq. (3.5); (b) Kernels obtained numerically from the Lorentzian-type functional form Eq. (3.2).

Tab. 3.4. Effective viscosities evaluated from $\eta_{G_4}(y)$, $\eta_{G_{2H}}(y)$ and numerically from $\tilde{\eta}_L(k)$. The values can be compared to the zero frequency, zero wavevector viscosities shown in Table 3.2.

		WCA			LJ		Chlorine
State Point	ρ_a	0.375	0.480	0.840	0.840	0.840	1.088
	T	0.765	0.765	1.000	0.765	1.000	0.97
2-term Gaussian	η_0	0.265	0.392	2.290	2.723	2.614	6.881
4-term Gaussian	η_0	0.265	0.390	2.288	2.807	2.653	6.897
Lorentzian	η_0	0.269	0.428	2.320	2.913	2.711	7.049

given in Table 3.2 shows an integration error of less than 3%. This confirms the accuracy of our numerical analysis techniques.

It is of interest to discuss the real space viscosity kernels for monatomic and diatomic systems from a structural point of view. For this purpose we define a structural normalization factor

$$\xi_g = \frac{\int\limits_0^\infty r[g(r)-1]^2 dr}{\int\limits_0^\infty [g(r)-1]^2 dr} \tag{3.7}$$

where $g(r)$ is the radial distribution function (RDF). Eq. (3.7) is a measure of the range over which the correlation function decays to 1 and therefore could be regarded as a correlation length of the radial distribution function. The RDF (or structure factor in reciprocal space) can be defined by

$$g(r) = \left\langle \frac{\sum_{i=1}^N \sum_{j>1}^N \delta(|\mathbf{r}-\mathbf{r}_{ij}|)}{4\pi r^2 N\rho} \right\rangle. \tag{3.8}$$

For an atomic description $\mathbf{r}_{ij}$ is the distance vector between atoms i and j, N is the total number of atoms, and ρ is the atomic number density. For a molecular fluid $\mathbf{r}_{ij}$ is the distance vector between the centers of mass of molecules i and j, N is the total number of molecules, and ρ is the molecular number density.

The atomic radial distribution functions and normalization factors are presented in Fig. 3.6. We can see that the RDF are typical monatomic and diatomic Lennard-Jones pair correlation functions. ξ_g generally increases as we increase the density and temperature from 0.605 at state point $\rho_a = 0.375, T = 0.756$ to 0.730 at $\rho_a = 0.480, T = 1.0$ and only slightly increases as we increase the cutoff distance, i.e. switch from WCA system to a LJ system at the same state point. ξ_g for chlorine at state point $\rho_a = 1.088, T = 0.97$ was found to be 0.585.

The normalized kernels with respect to $\eta(y = 0)$ and spatial scaling factor ξ_g are shown in Figs. 3.7(a) and 3.7(b). While generally the width of unnormalized kernels increases as we increase the density (Figs. 3.5(a) and 3.5(b)), the width of the normalized kernels of WCA fluids decreases marginally as we increase the density from 0.376 (continuous line) to 0.840 (short-dashed line). The LJ system shows a slightly narrower kernel (dotted line) compared to the WCA system at the same state point (short-dashed line). Though the kernels obtained from both

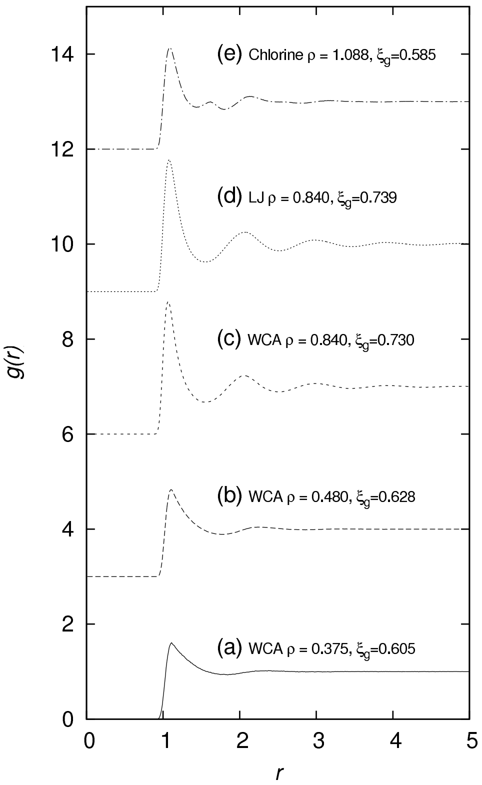

Fig. 3.6. Radial distribution function $g(r)$ and normalization factors ξ_g, Eq. (3.7): WCA [(a) $\rho_a = 0.375$, (b) $\rho_a = 0.480$ both at $T = 0.765$], (c) WCA ($\rho_a = 0.840$, $T = 1.0$); LJ (d) ($\rho_a = 0.840$, $T = 1.0$); chlorine (e) ($\rho_a = 1.088$, $T = 0.97$). For clarity, the RDFs are shifted upwards by 3 units.

functional forms are quite close to each other (almost identical for values of y of about half of the atomic or molecular diameters, i.e. $y = 0.5\sigma$), we can see in Fig. 3.7(a) and 3.7(b) that the structural normalization did not completely remove the discrepancy between the normalized kernels of the WCA system at different densities, and the normalized kernels of WCA, LJ and chlorine systems, for values higher than $y = \sigma$.

If we recall that Fig. 3.7(b) is based on a Lorentzian-type fit, a further question as to whether the kernel differences are due to numerical analysis, i.e. the choice of the fitting function, or due to improper structural factor arises. A four-term Gaussian only shows slightly narrower kernels which suggests a need for a more comprehensive structural normalization.

3.4 Summary

The main results can be summarized as follows:

(i) For monatomic fluids the shape of the normalized viscosity kernel in reciprocal space in

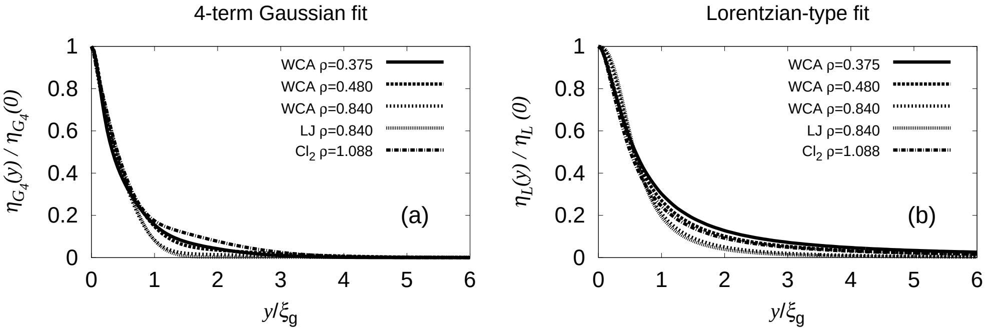

Fig. 3.7. Normalized real space viscosity kernels of monatomic and diatomic fluids, WCA ($\rho_a = 0.375$, $T = 0.765$), WCA ($\rho_a = 0.480$, $T = 0.765$), WCA ($\rho_a = 0.840$, $T = 1.0$), LJ ($\rho_a = 0.840$, $T = 1.0$), chlorine ($\rho_a = 1.088$, $T = 0.97$): (a) Normalized kernels, shown in Fig. 3.5(a), obtained from the four-term Gaussian functional form Eq. (3.5); (b) Normalized kernels, shown in Fig. 3.5(b), obtained numerically from the Lorentzian-type functional form Eq. (3.2).

the low wavevector region is the same for a whole range of densities considered here. Though the normalized reciprocal kernels insignificantly decrease with the density, they show a similar limiting behaviour at high k_y values. For the LJ potential compared to a WCA potential we find higher viscosities in the low wavevector region but the normalized shapes of the kernels are almost identical.

(ii) While a relatively simple Lorentzian-type function fits the atomic and diatomic data well over the entire range of k_y at all the state points it is not possible to analytically inverse Fourier transform it to the real space domain. Therefore one may consider up to a four-term Gaussian function which gives better accuracy in reciprocal space compared to the Lorentzian-type function. Our analysis of the high k_y regime reveals that the two-term equally weighted Gaussian functional form is inaccurate in predicting the real space kernels whilst the unequally weighted Gaussian only slightly improves the fit.

(iii) The overall conclusion is that the real space viscosity kernel for chlorine has a width of roughly 4-6 atomic diameters while for monatomic systems at high densities the width is about 3-5 atomic diameters and 2-4 atomic diameters at low densities. This means that generalized hydrodynamics must be used in predicting the flow properties of such fluids on length scales where the gradient in the strain rate varies significantly on these scales.

Finally, our results for diatomic fluids should also provide a good test for more complex molecular systems and the methodology can easily be used for instance in chain-like molecules. Such an analysis follows in the next section.

4 Molecular Fluids: Alkanes and Polymer Melts

4.1 Introduction

Because of their technological relevance, polymer solutions and melts are the subject of intense study. A polymer (synthetic or natural) is a macromolecule made up of many smaller units, sometime called monomers or mers. Polymers can vary in size from several mers to thousands of mers. These chains can be well organized like a box of uncooked spaghetti or very entangled like a bowl of cooked spaghetti. Bonded together these polymeric molecules form different architectures, such as linear and branched chains, rings, combs, networks etc. and the way they organize themselves greatly influences a material's property which motivates the great interest in understanding their dynamics.

Polymer chains can tangle up. The longer a polymer chain is, the more tangled up it can get. Since the chains are harder to pull out or separate, that can make products made out of polymers stronger. Some polymers are more straight and stiff than others. These won't tangle up as much, but they're strong for a different reason - stiff chains can pack together and stick to each other. Studies on time and length scales which determine the transition from unentangled to entangled dynamical behaviour by means of MD simulations can be found in [Doi 1986, Kremer 1990, Padding 2002].

The polymers we will consider here are all linear polymers. A linear polymer is made up of one molecule after another, hooked together in a long chain usually called the backbone. Linear polymers do not have to be in a straight, rigid line. Those single bonds between atoms in the backbone can swivel around. The dynamics of a separate polymer chain is by itself a very complex problem: the random motion of each bead is restricted by the chain connectivity and the interactions with other monomers, while the overall motion is the result of successive individual adjustments. Chain dynamics is even more complicated if the chain is part of a dense ensemble of other chains (in melts, glasses or networks): supplementary restrictions arise due to the chain entanglement.

We can understand the polymer structure and dynamics through the use of models [Flory 1969, Ferry 1980]. Analytic theories typically deal with idealized models, meaning that the specific chemical structure is reduced to the very essential parameters, such as connectivity, topology, excluded volume, etc. [Kremer 2003]. To understand a specific chemical system this is not sufficient. Therefore, there is also a tradition of work dealing with models, which incorporates as many chemical details as possible either by conducting extended quantum chemical calculations or by using ab initio density functional approaches [Car 1985, Cramer 2002, Jensen 2007]. Without going into great detail, we will only mention two of the most widely used theories for polymer melt dynamics: the Rouse model for the simple case of unentangled chains [Rouse 1953] and the reptation model for entangled chains [de Gennes 1979, Doi 1986]. In the Rouse model, a Gaussian chain of beads connected by springs interacts with a stochastic medium that mimics the presence of the other chains. As a consequence, the chain center of mass is subjected to particle-like diffusion. In the reptation model, on the other hand, the polymer chain is confined inside a ”tube” formed by the constraints imposed by entanglement with other chains. The chain length at which these reptation models dominate the dynamics is known as the entanglement length N_c. The reptation model was originally developed to describe the dynamics of a long chain inside highly dense polymer melts. Nevertheless this model might also be applied to the fracture behaviour of amorphous polymers [Evans 1987, Bulacu 2008]. It is important to mention that amorphous polymers in the glassy state have countless technical applications and therefore are very important. Our next section will be solely dedicated to such systems.

Alkane chains, also known as paraffins, are very important chemical compounds, yet relatively simple, and therefore will be targeted in this section. In short, alkanes consist only of the elements carbon and hydrogen (i.e. hydrocarbons), wherein these atoms are linked together exclusively by single bonds (i.e. they are saturated compounds) without any cyclic structure (i.e. loops) [Olah 2003]. Saturated hydrocarbons can be linear wherein the carbon atoms are joined in a snake-like structure, branched wherein the carbon backbone splits off in one or more directions, or cyclic wherein the carbon backbone is linked so as to form a loop. Saturated hydrocarbons can also combine any of the linear, cyclic and branching structures, and they are still alkanes as long as they are acyclic (i.e. having no loops). In general, there is no limit to the number of carbon atoms that can be linked together, the only limitation being that the molecule is acyclic, is saturated, and is a hydrocarbon. Saturated oils and waxes are examples of larger alkanes where the number of carbons in the carbon backbone tends to be greater than 10. An investigation on how the branching structure of alkanes changes under confinement and its ramifications for transport properties of confined fluids can be found in [Wang 2002].

Although alkanes are not very reactive and have little biological activity they are very important in biological applications. Alkanes can be viewed as a molecular tree upon which can be hung the interesting biologically active/reactive portions of molecules. However, their thermodynamic and transport properties are of interest mainly in petrochemical applications [Freund 1982]. Some synthetic polymers such as polyethylene and polypropylene are alkanes with chains containing hundreds of thousands of carbon atoms. These materials are used in innumerable applications.

A considerable number of studies have been devoted to the simulation of thermophysical properties of alkanes over a wide range of physical conditions. Many groups worldwide have worked on the development of sophisticated alkane models and force fields to achieve excellent agreements with experiments often with the price of high computational costs [Gordon 2006, Smit 1999].

In this work[3] we will focus our attention on a linear alkane with four carbon atoms i.e. butane. Though the term butane may refer to any of two structural isomers (i.e. unbranched and branched), or to a mixture of them, in the IUPAC nomenclature [IUPAC 2010], however, butane refers only to the unbranched *n*-butane isomer; the other one being called ”methylpropane”. To simulate butane we have used the united atom model by Ryckaert and Bellemans [Daivis 1994, Ryckaert 1975, Ryckaert 1978] because it gives a reasonable value for the viscosity.

Our simulations are based on the Edberg, Evans, and Morriss algorithm [Edberg 1986, Edberg 1987b, Baranyai 1990, Daivis 1992] with an improved cell neighbour list construction algorithm [Matin 2003]. Both, model butane and polymer melts, were summarized in Section 2. We have also studied the chain length dependence of the viscosity kernel. A series of three different molecular sizes was studied, consisting of 10, 20 and 50-site molecules. The system sizes studied were 108 and 864 molecules and the molecular temperature and reduced site number

---

[3] This section contains material reprinted with permission from R. M. Puscasu *et al.*, Phys. Rev. E **82**, 011801 (2010). Copyright 2010, American Physical Society.

density were $T = 1.0$ and $\rho_a = 0.84$, respectively. The state point was chosen to correspond to previous studies [Daivis 2007, Kröger 1993, Kremer 1990] of chain dynamics. These parameters remained constant through this series of simulations. The values of the relevant simulation parameters are summarized in Table 4.1.

We conduct the simulations using a fifth-order Gear algorithm [Gear 1966, Gear 1971] with an integration timestep of $\delta t = 0.002$. The equations of motion (EOM) for model butane and polymer melts were introduced in Section 2.

After the initial equilibration, we performed production runs for a minimum of 1.4×10^7 time steps averaging 14 runs, each of length 10^6 steps. The transverse momentum density ACFs were computed over at least 10 reduced time units for 10-site molecules and over at least 20 reduced time units for 50-site molecules. The stress ACFs were computed over at least 20 and 40 reduced time units for 10-site and 50-site molecules, respectively. Correlation functions, Laplace transforms and wavevector dependent viscosities are all computed as described in Section 3.1.

The results presented below have been obtained by simulation of 108 and 864 molecules in the isokinetic molecular dynamics ensemble. In this section we report results for transverse momentum density and shear stress autocorrelation functions, structural properties, reciprocal and real space viscosity kernels for two molecular systems, namely, butane and FJC polymeric melts. In order to validate our code and results we reproduced and compared previous results for correlation functions, self-diffusion and zero wavevector, zero frequency dependent viscosities of butane and FJC chains where possible. Very good agreement was found in all cases.

4.2 Correlation functions

Initially, we examine the momentum density and shear stress autocorrelation functions in atomic and molecular representations. We must first note that the ACFs were evaluated for both 108 and 864 molecule systems in order to determine whether the results were system size dependent. No such evidence was found for butane as well as for FJC systems. In order to limit the number of figures, we only display the results for one state point for butane and FJC molecules and for system size $N_m = 864$.

The transverse momentum density ACFs in atomic and molecular representations for four non-zero wavevectors are shown for butane in Figs. 4.1(a,b), and for FJC in Figs. 4.2(a,b). Their corresponding integrals are shown in Figs. 4.1(c,d) and Figs. 4.2(c,d) respectively.

The general features of our transverse momentum density ACFs are in agreement with those observed previously for hard spheres [Alley 1983a] and for Lennard Jones liquids [Palmer 1994].

Tab. 4.1. Simulation details

	Butane	FJC/FENE
Site number density, ρ_a	$1.676, 1.46$	0.84
Temperature, T	$4.05, 3.79$	1
Number of molecules, N_m	$108, 864$	$108, 864$
Number of sites, N_s	4	$10, 20, 50$
Bond length, l	0.39	1
LJ cutoff, r_c	2.5	$2^{1/6}$

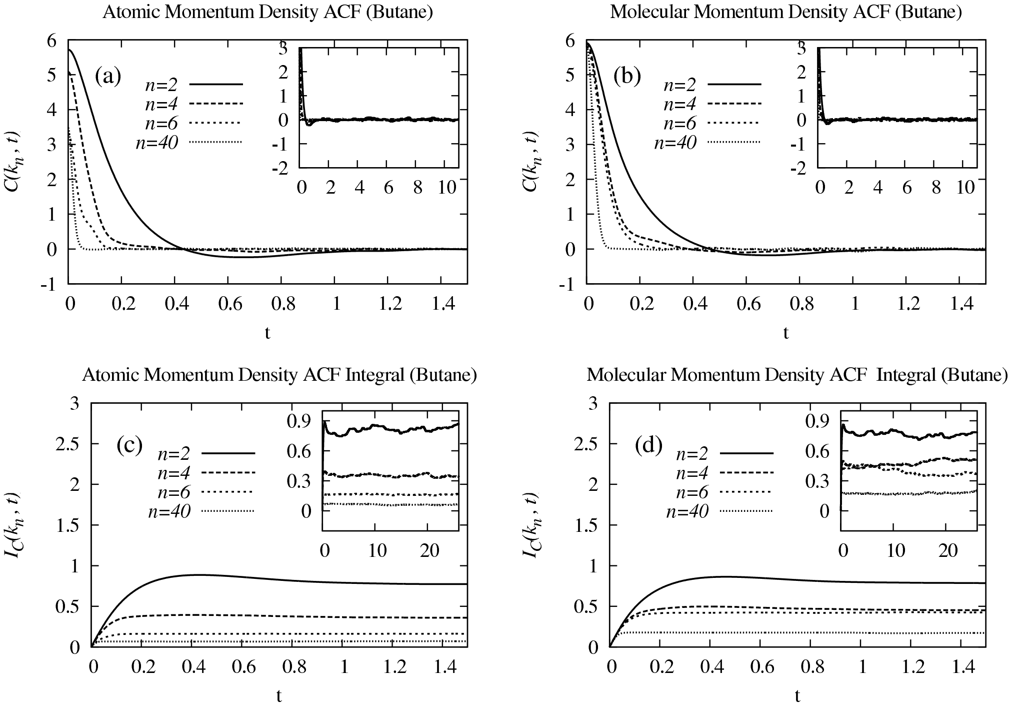

Fig. 4.1. Momentum density ACFs as a function of mode number n for butane in atomic and molecular formalisms ($\rho_a = 1.46$, $T = 4.05$, $N_m = 864$, $N_s = 4$): (a) Atomic transverse momentum density ACFs, Eq. (1.53); (b) Molecular transverse momentum density ACFs, Eq. (1.53); (c) Integral of the atomic transverse momentum density ACFs, Eq. (1.54); (d) Integral of the molecular transverse momentum density ACFs, Eq. (1.54). The momentum density **J** in Eq. (1.53) is either in atomic or molecular representation i.e. either Eq. (1.11) or Eq. (1.21). The insets show the long-time behaviors for the same mode numbers.

Though the simulated values of $C_\perp(\mathbf{k}, t = 0)$ (for butane $C_\perp(\mathbf{k} = 0, t = 0) = 5.913$ at $\rho = 1.46, T = 4.05$) in the molecular representation are in agreement with theoretical values, Eq. (1.55), (for butane $C_\perp(\mathbf{k} = 0, t = 0) = 5.909$, $\rho_a = 1.46, T = 4.05$), a closer examination of Fig. 4.1(a) and Fig. 4.2(a) shows that, in the atomic representation, the zero time momentum density ACFs differ for different k_y values. Presumably, this is a consequence of correlations between the momenta of different sites on the same molecule that are involved in bond angle or bond length constraints (see Evans and Morriss, Chapter 4. Eq. (37) in [Evans 1990]). As a consequence, there is no longer a simple relationship between the temperature and the zero time value of the momentum density ACF. This is confirmed by the following analysis.

Having the transverse momentum current for a molecular system in the atomic representation defined by Eq. (1.11) we can form the equilibrium transverse current autocorrelation function by

$$\Big\langle J_x(k_y) J_x^*(k_y) \Big\rangle \quad = \quad \Big\langle \sum_{i=1}^{N_m} \sum_{\alpha=1}^{N_s} p_{xi\alpha} e^{ik_y y_{i\alpha}} \sum_{j=1}^{N_m} \sum_{\beta=1}^{N_s} p_{xj\beta} e^{-ik_y y_{i\beta}} \Big\rangle. \tag{4.1}$$

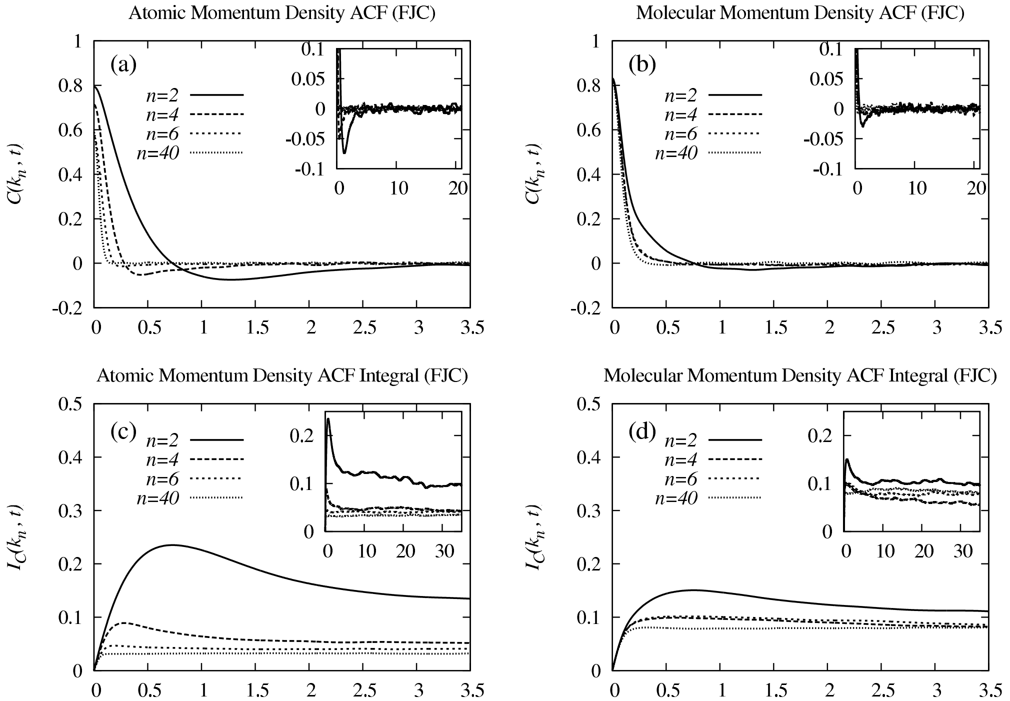

Fig. 4.2. Momentum density ACFs as a function of mode number n for FJC in atomic and molecular formalisms ($\rho_a = 0.84$, $T = 1.0$, $N_m = 108$, $N_s = 10$): (a) Atomic transverse momentum density ACFs, Eq. (1.53); (b) Molecular transverse momentum density ACFs, Eq. (1.53); (c) Integral of the atomic transverse momentum density ACFs, Eq. (1.54); (d) Integral of the molecular transverse momentum density ACFs, Eq. (1.54). The insets show the long-time behaviors for the same mode numbers.

If we expand Eq. (4.1) into

$$\begin{aligned}\Big\langle J_x(k_y)J_x^*(k_y)\Big\rangle &= \Big\langle \sum_{i=1}^{N_m}\sum_{\alpha=1}^{N_s} p_{xi\alpha}^2\Big\rangle + \Big\langle \sum_{i=1}^{N_m}\sum_{\alpha=1}^{N_s}\sum_{\beta\neq\alpha}^{N_s} p_{xi\alpha}p_{xi\beta}e^{ik_y(y_{i\alpha}-y_{i\beta})}\Big\rangle \\ &+ \Big\langle \sum_{i=1}^{N_m}\sum_{\alpha=1}^{N_s}\sum_{j\neq i}^{N_m}\sum_{\beta=1}^{N_s} p_{xi\alpha}p_{xj\beta}e^{ik_y(y_{i\alpha}-y_{j\beta})}\Big\rangle \qquad (4.2)\end{aligned}$$

we can see that Eq. (4.2) factorizes into three terms. The first term is the total atomic kinetic energy, which is directly related to the atomic temperature. The second term involves the zero time value of a correlation function of the momenta for different atoms on the same molecule. These atoms may be connected by constraints and their momenta will be correlated, so the mean value of this term is expected to have a non-zero value. The third term, involving correlations between the momenta of atoms on different molecules is expected to be zero at equilibrium. Therefore the y-intercepts in Figs. 4.1 and 4.2 are computed from the correlation function in

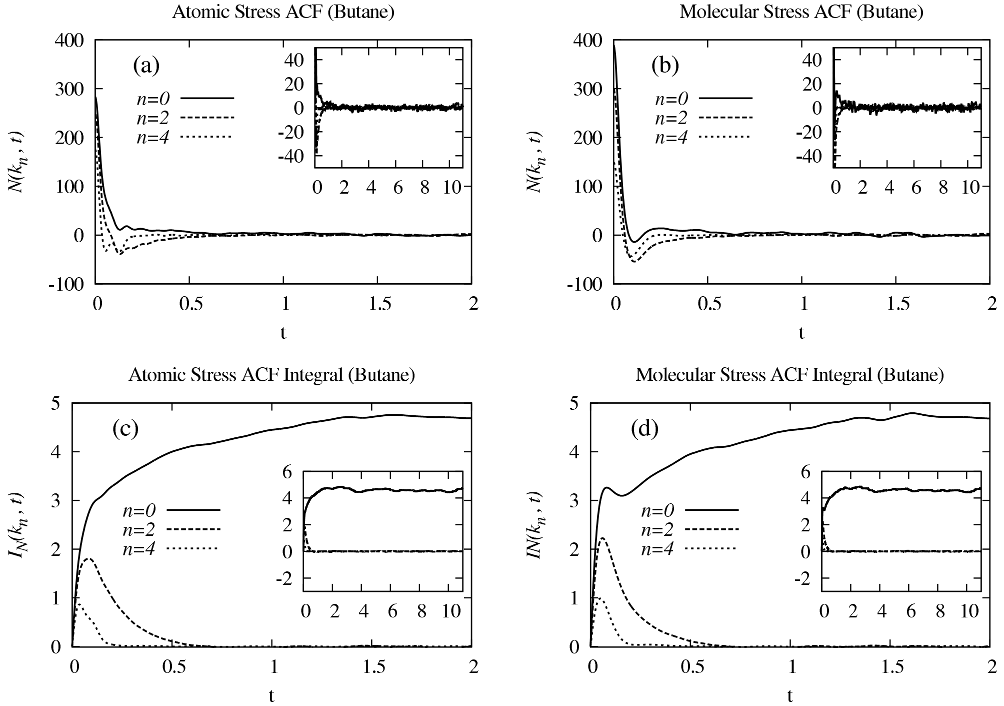

Fig. 4.3. Stress ACFs as a function of mode number n for butane in atomic and molecular formalisms ($\rho_a = 1.46$, $T = 4.05$, $N_m = 864$, $N_s = 4$): (a) Atomic stress ACFs, Eq. (1.57); (b) Molecular stress ACFs, Eq. (1.57); (c) Integral of the atomic stress ACFs, Eq. (1.60); (d) Integral of the molecular stress ACFs, Eq. (1.60). The atomic stress ACFs in Eq. (1.57) were computed with atomic pressure tensor and the molecular stress ACFs were computed with molecular pressure tensor. The insets show the long-time behaviors for the same mode numbers.

Eq. (1.53) and not from the temperature, Eq. (1.55). Note that Eq. (1.55) is only true when T is interpreted as the molecular temperature.

The shear stress ACFs in atomic and molecular representations for four wavevectors are plotted for butane in Figs. 4.3(a,b) and for FJC in Figs. 4.4(a,b) and their integrals in Figs. 4.3(c,d) and Figs. 4.4(c,d) respectively. All the ACFs show a fast, oscillatory, initial decay followed by a long-time tail. The tail's noise is surprisingly higher in the molecular formalism and equally pronounced in both butane and polymeric systems. The main difference between zero and finite k_y functions is that their time integral is proportional to the viscosities at $k_y = 0$, but it vanishes for nonzero k_y due to the conservation law. As a consequence the generalized viscosities cannot be obtained from a Green-Kubo integration at nonzero k_y as pointed out by Evans and Morriss [Evans 1990]. The long-time value of the zero wavevector integral (the Green-Kubo expression for the viscosity) converges to a viscosity of 4.8 for butane, which is in excellent agreement with the Green-Kubo data at the same state point given by Daivis and Evans [Daivis 1995]. The

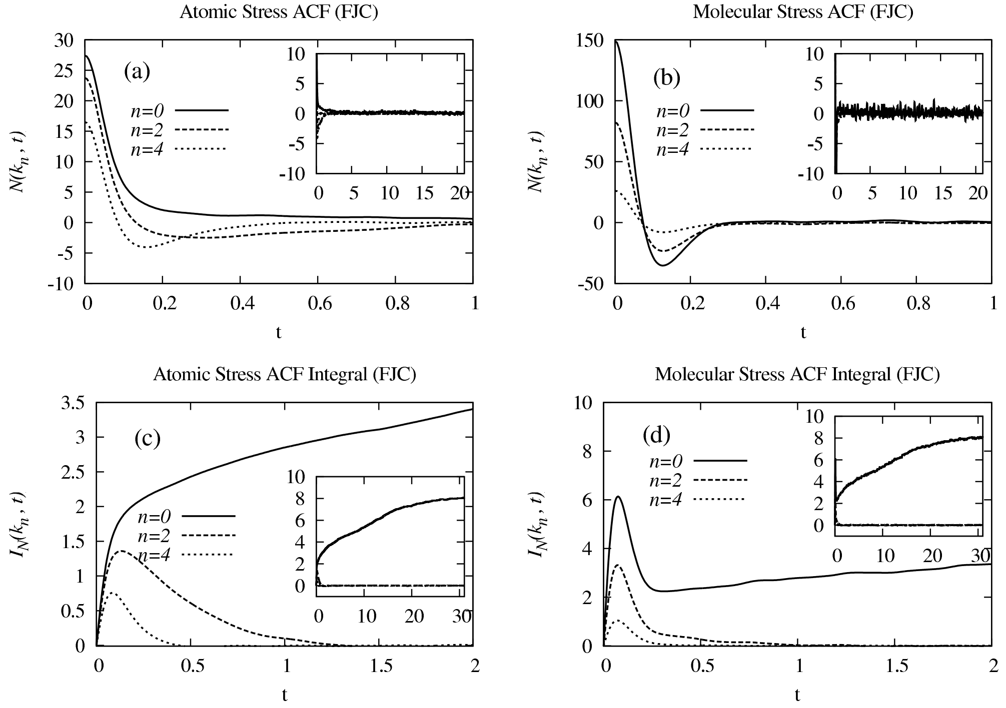
Atomic Stress ACF (FJC)

Molecular Stress ACF (FJC)

Atomic Stress ACF Integral (FJC)

Molecular Stress ACF Integral (FJC)

Fig. 4.4. Stress ACFs as a function of mode number n for FJC in atomic and molecular formalisms ($\rho_a = 0.84$, $T = 1.0$, $N_M = 108$, $N_s = 10$): (a) Atomic stress ACFs, Eq. (1.57); (b) Molecular stress ACFs, Eq. (1.57); (c) Integral of the atomic stress ACFs, Eq. (1.60); (d) Integral of the molecular stress ACFs, Eq. (1.60). The insets show the long-time behaviors for the same mode numbers.

butane system shows a shorter convergence time value compared to polymeric systems.

4.3 Reciprocal space viscosity kernel

The reciprocal space viscosity kernels for model butane and FJC are shown in Figs. 4.5-4.7. The error bars are within the symbol sizes and are therefore omitted. The statistical reliability of reciprocal space kernel data increases as k_y increases.

For butane we found the zero wavevector, zero frequency viscosity to be $\eta_0 = 4.8 \pm 0.2$ which agrees with the results of Daivis *et al.* [Daivis 1995] 4.8 ± 0.1 (or 0.154 ± 0.004 kg m^{-1} s^{-1}). For polymer melts we found $\eta_0 = 8.1 \pm 0.2$ ($N_s = 10$), $\eta_0 = 15.2 \pm 0.3$ ($N_s = 20$), $\eta_0 = 41.2 \pm 0.4$ ($N_s = 50$) which agrees with the limiting values $\eta_0 = 8.42 \pm 0.04$ ($N_s = 10$), $\eta_0 = 15.6 \pm 0.1$ ($N_s = 20$), $\eta_0 = 41.3 \pm 0.6$ ($N_s = 50$) [Daivis 2007] of the shear viscosities at zero strain rate. Kröger *et al.* also reported a slightly lower viscosity of 7.09 ± 0.09 for a 10-site FENE (finite extensible nonlinear elastic) chain [Kröger 1993]. We see that the zero-wave vector viscosity follows a simple proportionality $\eta \propto N_s$ (typically described by a Rouse model) which

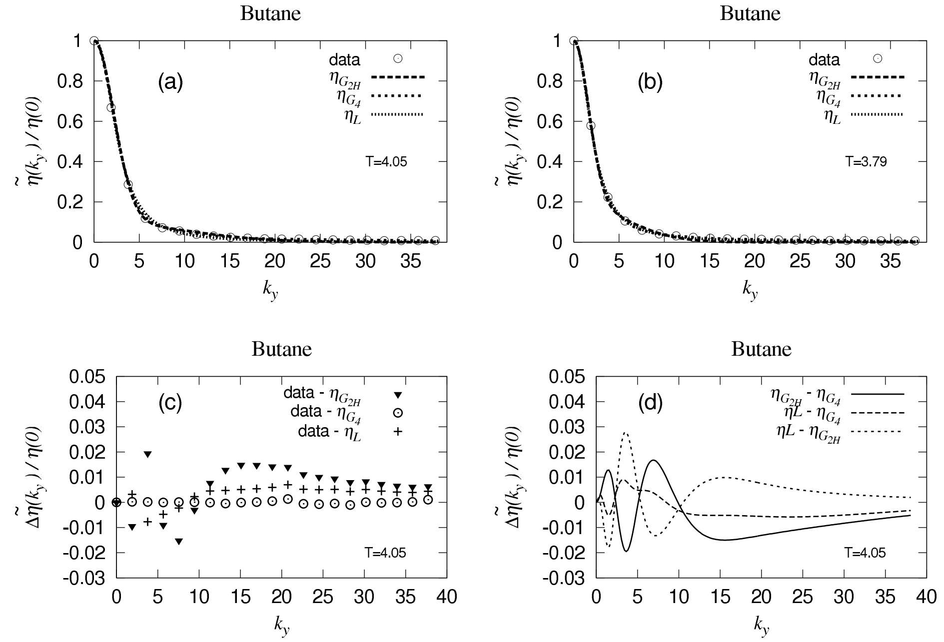

Fig. 4.5. Reciprocal space kernel of butane ($\rho_a = 1.46$, $N_m = 864$) in the atomic formalism: (a) Normalized kernel data at $T = 4.05$ and best fits to Eqs. (3.1) and (3.2); (b) Normalized kernel data at $T = 3.79$ and best fits to Eqs. (3.1) and (3.2); (c) Differences between the kernels data and fits shown in (a); (d) Differences between the fits shown in (a).

confirms that the chain considered here is not long enough to cover the crossover regime from the nonentangled to the entangled state.

In Figs. 4.5(a) and 4.5(b) we compare the reciprocal space kernels of butane at two state points ($\rho = 1.46$, $T = 4.05$) and ($\rho = 1.46$, $T = 3.79$). While the zero wavevector viscosity decreases with temperature from 5.41 at $T = 3.79$ to 4.76 at $T = 4.05$, the width and the shape of the normalized kernel data varies insignificantly in this range of temperatures, getting slightly larger at $T = 4.05$. The kernel data points in Figs. 4.5(a) and 4.5(b) have also been fitted to several functional forms given in the previous section for simple monatomic and diatomic fluids. We discuss the parameterization of the reciprocal space kernels further below. In Figs. 4.6 we plot the wavevector dependent viscosity for a polymeric chain upon increasing the chain length from 10 up to 50 sites per chain. It is seen that the zero wave-vector viscosity increases linearly with N_s. However, the half width at half maximum is almost constant which suggests that the normalized shape of the reciprocal space kernel with respect to zero wave-vector value must be identical for all three chain lengths. Further evidence supporting this statement will be shown later in Fig. 4.7.

For completeness we also compared the FJC kernels with kernels computed for FENE [Kröger 1993] chain systems of equivalent molecular weight and state point. The kernels in both models were essentially identical, therefore FENE results are not explicitly displayed. The

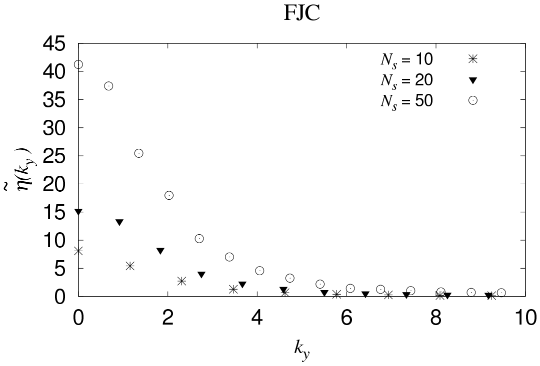

Fig. 4.6. Reciprocal space kernel of FJC melts in the atomic formalism at three different chain lengths ($\rho_a = 0.84$, $T = 1.0$, $N_m = 864$): $N_s = 10$, $N_s = 20$ and $N_s = 50$.

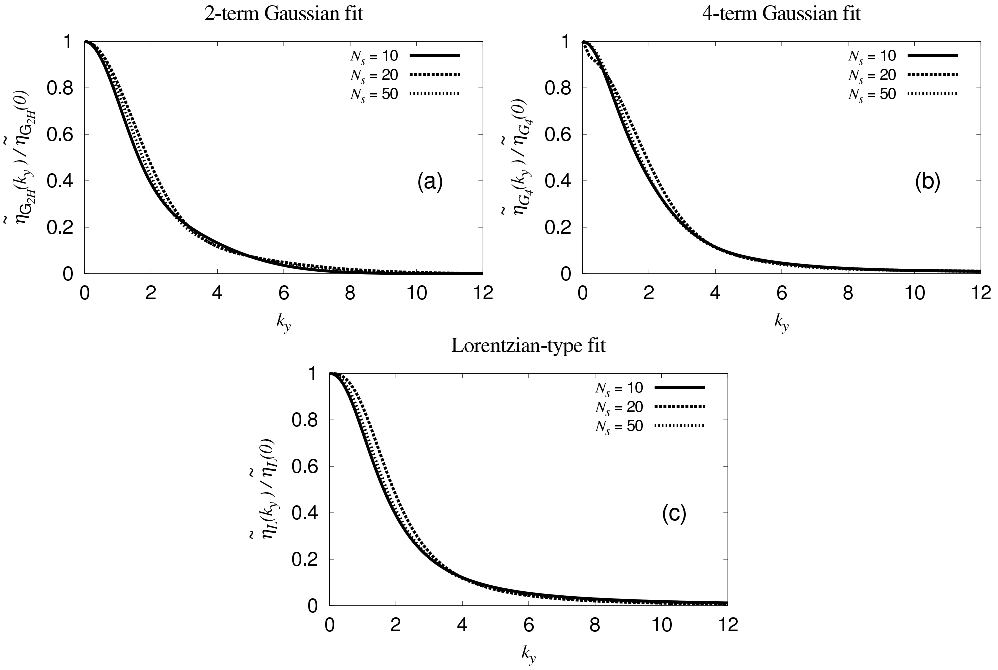

Fig. 4.7. Reciprocal space kernels of FJC melts at three different chain lengths: $N_s = 10$, $N_s = 20$ and $N_s = 50$ ($\rho_a = 0.84$, $T = 1.0$, $N_m = 864$): (a) Kernels obtained from the two-term Gaussian functional form Eq. (3.1); (b) Kernels obtained from the four-term Gaussian functional form Eq. (3.1); (c) Kernels obtained from the Lorentzian-type functional form Eq. (3.2).

similarity of the viscosity kernel of these two molecules arises because, despite using different models, the molecular structure varies only slightly. The similarity of FJC and FENE systems has also been recently confirmed by Hunt and Todd [Hunt 2009a, Hunt 2009b] for shear and extensional viscosities and diffusion tensor. The computational efficiency of the FENE and FJC force calculations are also similar due to the sparse matrix linear equation solver used for tridiagonal matrices which is applied in the FJC system.

In the previous section we proposed functional forms that fit the reciprocal space viscosity kernel data. The results of the fittings based on Eqs. (3.1) and (3.2) for butane and FJC chains are listed in Table 4.2 along with the magnitude of the residuals estimated using the residual standard deviation defined by Eq. (3.3). Table 4.3 also confirms the value of 1 for the total Gaussian amplitudes.

The results show that a relatively simple equally-weighted two-term Gaussian function fits the butane data, Figs. 4.5(a) and 4.5(b), with less then 2% error Fig. 4.5(c). The Lorentzian-type function fits the butane data much better over the entire wavevector range. While generally a third term in the Gaussian function improves the fit, only the fourth term shows a better precision compared to the Lorentzian-type function Fig. 4.5(c). In Fig. 4.5(d) we plot the diferences between all three functional forms for the same state point of butane.

In Figs. 4.7(a-c) we plot the Gaussian and Lorentzian-type fits to the atomic reciprocal space kernel data of the FJC system shown previously in Figs. 4.6(a-c) at three different chain lengths.

Tab. 4.2. Zero frequency, zero wavevector shear viscosity and fitting parameter values for molecular systems in the atomic representation

		Butane		FJC		
State Point	ρ_a	1.46	1.46	0.84		
	T	4.05	3.79	1.0		
System size	N_m	864		864		
	N_s	4		10	20	50
	η_0	4.8[0.2][1]	5.4[0.3]	8.1[0.2]	15.2[0.3]	41.2[0.4]
2-term Gaussian, $A_2 = 1 - A_1$ Eq. (3.1)	A	0.133	0.202	0.375	0.170	0.250
	σ_1	10.29	6.708	2.769	3.810	3.213
	σ_2	2.105	1.585	1.044	1.452	1.261
	s_r	0.078	0.086	0.092	0.194	0.552
2-term Gaussian Eq. (3.1)	A_1	0.123	0.200	0.368	0.139	0.252
	A_2	0.855	0.795	0.629	0.842	0.749
	σ_1	10.87	6.764	2.792	4.169	3.203
	σ_2	2.170	1.598	1.056	1.511	1.257
	s_r	0.077	0.089	0.094	0.181	0.567
4-term Gaussian Eq. (3.1)	A_1	0.646	0.349	0.571	0.773	0.544
	A_2	0.231	0.532	0.270	0.061	0.188
	A_3	0.094	0.095	0.144	0.147	0.251
	A_4	0.028	0.023	0.016	0.019	0.027
	σ_1	2.549	2.762	1.618	1.556	1.413
	σ_2	1.127	1.284	0.730	0.093	0.811
	σ_3	7.876	7.175	3.423	3.227	2.639
	σ_4	28.17	28.02	12.92	11.29	8.544
	s_r	0.006	0.004	0.006	0.102	0.443
Lorentzian-type Eq. (3.2)	α	0.145	0.235	0.338	0.167	0.270
	β	1.997	1.872	2.210	2.726	2.398
	s_r	0.046	0.032	0.054	0.069	0.417

Tab. 4.3. Total amplitude for Gaussian functional form

		Butane			FJC	
State Point	ρ_a	1.46	1.46		0.84	
	T	4.05	3.79		1.0	
	N_s	4		10	20	50
2-term Gaussian	$\sum_{j=1}^{2} A$	0.978	0.995	0.997	0.981	1.001
4-term Gaussian	$\sum_{j=1}^{4} A$	0.997	0.999	1.001	1.000	0.940

Though the shape of the normalized kernels is slightly affected by the choice of fitting function it shows very little difference upon increase of the chain length. Essentially, the normalized reciprocal space kernel of polymer melts does not change with the chain lengths considered here and the insignificant deviations could simply be due to the numerical error of the fitting procedure and relatively high zero wave-vector value the reciprocal space kernels are normalized with as we increase the chain length.

4.4 Real space viscosity kernel

The viscosity kernel in physical space can be found via an inverse Fourier cosine transform, Eq. (3.4), which is a special case of the continuous Fourier transform of even functions. The inverse Fourier cosine transform of the Gaussian function was given previously in Eq. (3.5) and for the Lorentzian-type function, the integral in Eq. (3.4) was evaluated numerically by a Simpson method [Hansen 2007, Puscasu 2010b].

The real space viscosity kernel results for butane at two temperatures ($T = 4.05$ and $T = 3.79$) are presented in Fig. 4.8 and data for polymer melts at three densities are presented in Figs. (4.9). The real space kernel decreases slightly with the temperature, but it is strongly affected by the choice of fitting function in reciprocal space. For instance, kernels obtained from a two-term equally-weighted Gaussian functional form, shown in Fig. 4.8(a), are strongly distorted in physical space and therefore more terms in the Gaussian form are needed. To illustrate this point, we consider a four-term Gaussian shown in Fig. 4.8(b). Kernels obtained numerically from the Lorentzian-type functional form are shown in Fig. 4.8(c), and feature a much smoother behaviour in real space. The maximum difference between the kernels obtained from the Gaussian functions is about 5% and between the kernels obtained from the Lorentzian-type function and Gaussian functions is less than 10%, Fig. 4.8(d).

For the FJC system, the trends are illustrated in Fig. 4.9 for unnormalized data and in Figs. 4.10 for normalized data. The difference between these functional forms is given in Fig. 4.11. Despite the very large discrepancy between kernels predicted by a four-term Gaussian function and a Lorentzian-type function of almost 40% at $y = 0$, Fig. 4.11(a), the local effective viscosity, η_0, obtained by integrating the nonlocal real space kernel over y is in good agreement (Table 4.4).

As mentioned previously, the four-term Gaussians show much better fits and can be trusted when transforming the reciprocal space kernels into the physical domain. However, we note that the four-term Gaussian function is sensitive to the statistical variation of the data and may result

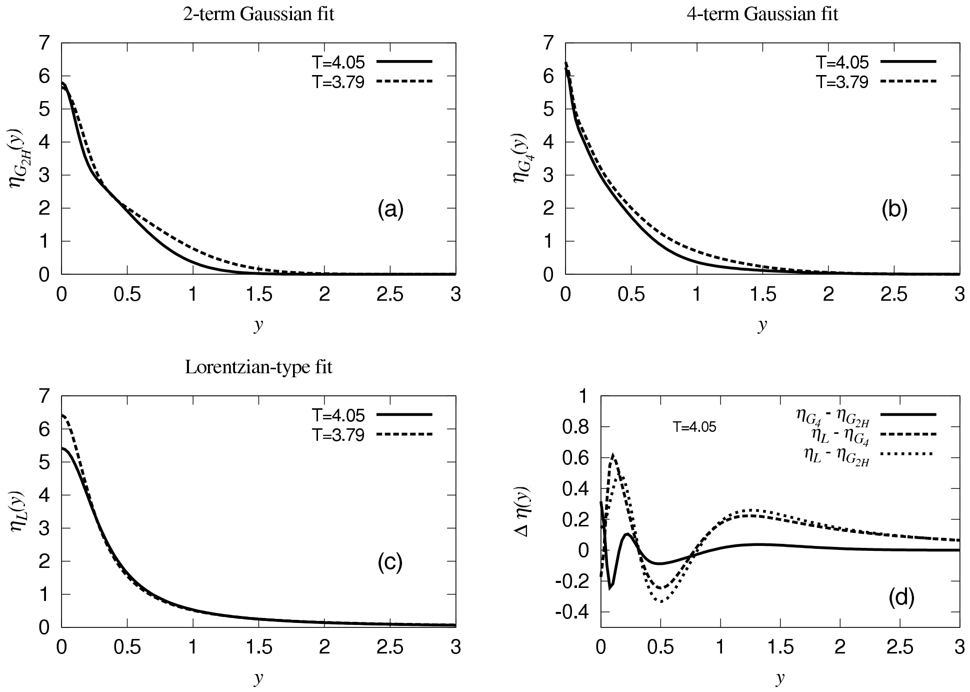

Fig. 4.8. Real space kernel of butane ($\rho_a = 1.46$) at two different temperatures, $T = 4.05$ and $T = 3.79$: (a) Real space kernels obtained from Gaussian functional form Eq. (3.5); (b) Real space kernels obtained from Gaussian functional form Eq. (3.5); (c) Real space kernels obtained numerically from the Lorentzian-type functional form Eq. (3.2); (d) Difference between the kernels (a-c) for $T = 4.05$.

in unnatural behaviour while the Lorentzian-type function shows a much smoother shape of the real space kernels.

The zero wavevector viscosity η_0 obtained via the Gaussian function Eq. (3.6) with $N_G = 2$ for the two-term Gaussian and $N_G = 4$ for the four-term Gaussian along with the zero wavevector viscosity obtained via the Lorentzian-type function are shown in Table 4.4. Though all three functional forms yield different kernel shapes the local effective viscosities η_0 are in good agreement with the simulated values presented in Table 4.2. It is seen that the error associated with the integration is less than 2% compared to simulated zero frequency zero wavevector viscosities given in Table 4.2. This confirms the accuracy of our numerical analysis.

The difference between the kernels obtained from the Lorentzian-type function and the four-term Gaussian functions increases with the chain length as seen in Fig. 4.11(b). However, the local effective viscosities agree with the computed values even at high molecular weights.

In order to compare the real space viscosity kernels for different molecular systems we use the normalization factor ξ_g that accounts for the structural properties defined previously in section 3. ξ_g is a measure of the range over which the radial distribution function decays to 1 and therefore is regarded as a correlation length of the radial distribution function (RDF). The RDF

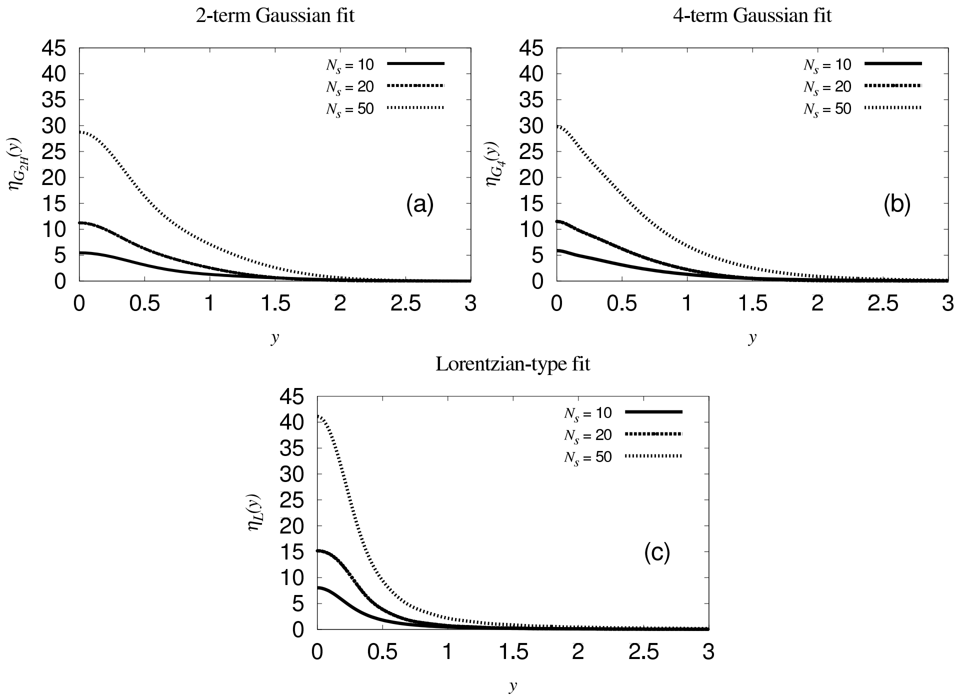

Fig. 4.9. Real space kernel of FJC melts at three different chain lengths $N_s = 10$, $N_s = 20$ and $N_s = 50$ ($\rho_a = 0.84$, $T = 1.0$, $N_m = 864$): (a) Real space kernels obtained from the equally-weighted two-term Gaussian functional forms Eq. (3.5); (b) Real space kernels obtained from the four-term Gaussian functional forms Eq. (3.5); (c) Real space kernels obtained numerically from the Lorentzian-type functional form Eq. (3.2).

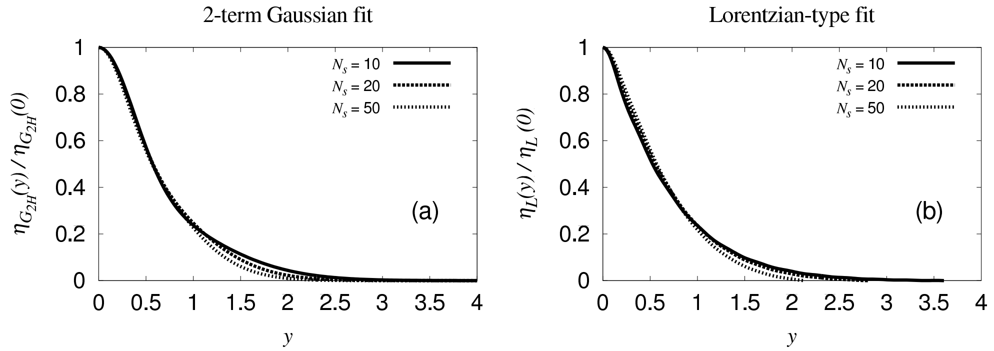

Fig. 4.10. Real space kernel of FJC melts at three different chain lengths, $N_s = 10$, $N_s = 20$ and $N_s = 50$ ($\rho_a = 0.84$, $T = 1.0$, $N_m = 864$): (a) Real space kernels normalized by $\eta(y = 0)$ obtained from the equally-weighted two-term Gaussian functional form Eq. (3.5); (b) Real space kernels normalized by $\eta(y = 0)$ and obtained numerically from Lorentzian-type functional form Eq. (3.2).

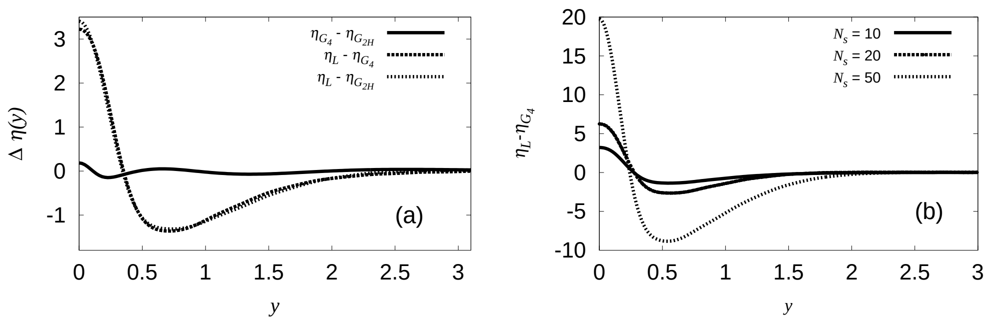

Fig. 4.11. Difference between the real space kernels for (a) 10-site FJC system obtained from three functional forms and (b) the difference between the real space kernels obtained from the Lorentzian-type and four-term Gaussian functions for three different chain lengths N_s.

gives us important information about structure in dense liquid butane and polymer melts and corresponding normalization factors for these systems are presented in Fig. 4.12.

RDFs for butane at state point ($\rho_a = 1.46$, $T = 4.05$) and ($\rho_a = 1.46$, $T = 3.79$) are shown in Fig. 4.12(a,b) and have the same form as those from [Edberg 1986, Ryckaert 1978]. The sharp peaks at $\sigma = 0.39$ and $\sigma = 0.63$ arising from nearest- and next-nearest-neighbour constraints are omitted from the calculation of ξ_g in Eq. (3.7). The broad and sharp peaks in Figs. 4.12(a,b) correspond to *gauche* and *trans* conformations respectively. The remainder of the $g(r)$ curves show intermolecular correlations. For the FJC system the radial distribution functions, given for $N_s = 10$, $N_s = 20$ and $N_s = 50$ in Figs. 4.12(c), 4.12(d) and 4.12(e), show the sharp peaks due to bonds ($l = 1.0\sigma$) and LJ shells. The second LJ coordination shell is visible in a peak at $r \approx 2\sigma$. Our RDFs for polymer melts are in agreement with [Bulacu 2007, Bennemann 1998]. Compared to butane, for which ξ_g changes significantly from 0.489 at state point $\rho = 1.676$, $T = 4.05$ to 1.195 at state point $\rho = 1.46$, $T = 3.79$, ξ_g for FJC only slightly increases from

Tab. 4.4. Effective viscosities evaluated from $\eta_{G_{2H}}(y)$, $\eta_{G_4}(y)$ and numerically from $\eta_L(k_y)$

		Butane		FJC		
State Point	ρ_a	1.46	1.46		0.84	
	T	4.05	3.79		1.0	
System size	N_m	864			108	
	N_s	4		10	20	50
2-term Gaussian	η_0	4.759	5.410	8.09	15.2	41.2
4-term Gaussian	η_0	4.760	5.410	8.09	15.2	41.2
Lorentzian	η_0	4.761	5.412	8.09	15.2	41.2

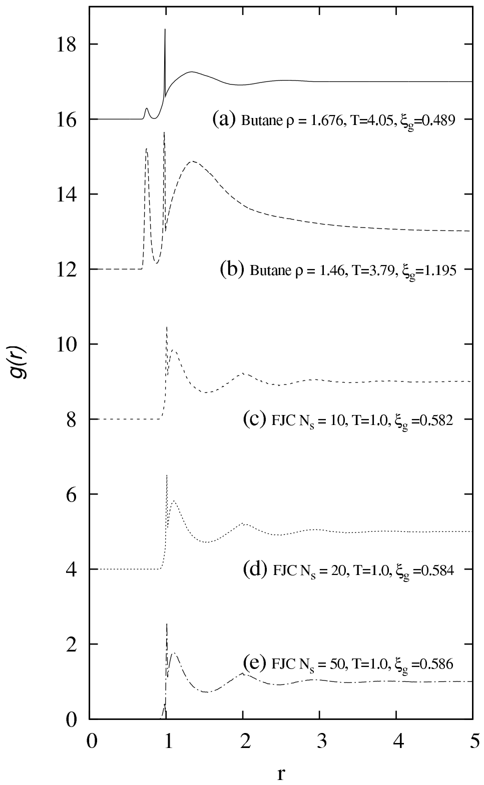

Fig. 4.12. Total intra- and intermolecular radial distribution function $g(r)$ and normalization factors ξ_g for butane at two state points (a) ($\rho_a = 1.46$, $T = 4.05$), (b) ($\rho_a = 1.46$, $T = 3.79$) and FJC at state point ($\rho_a = 0.84$, $T = 1.0$, $N_m = 864$) for (c) $N_s = 10$, (d) $N_s = 20$ and (e) $N_s = 50$. For butane the peaks at $\sigma = 0.30$ and $\sigma = 0.63$ arising from nearest-neighbour and next-nearest neighbour constraints are omitted. For clarity, the RDFs in (d), (c) (b) and (a) are shifted upwards by 4 units.

0.534 to 0.548 as we enlarge the polymers from 10 to 50 sites per molecule.

The real space kernels for butane, normalized with respect to their zero wavevector values and spatial scaling factor ξ_g, are shown in Fig. 4.13. Firstly, we see that the kernels obtained from a Lorentzian-type fit for two-different temperatures $T = 4.05$ (continuous line) and $T = 3.79$ (long-dashed line), Fig. 4.13(b), normalized with respect to ξ_g deviate substantially from their unnormalized analogs shown in Fig. 4.13(a). Since the normalization factor has been calculated from the total intra- and inter-molecular radial distribution function it is to be expected that the peaks due to intra-molecular interactions will have a greater contribution at low temperatures as seen in Fig. 4.13(b). Therefore, in addition to previously given kernels, we also plot the normalized kernels with respect to only the inter-molecular RDF (dashed and dotted lines in Fig. 4.13(b). We can see that the kernels are closer in Fig. 4.13(b) for the same set of temperatures and densities. However, our normalization did not remove the discrepancy between the kernels

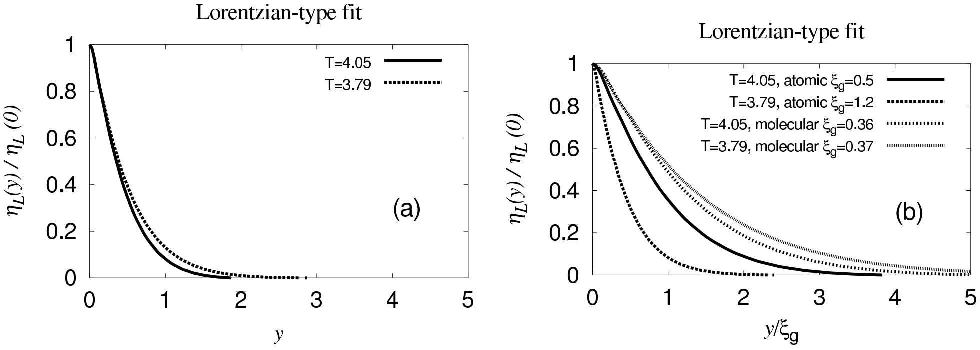

Fig. 4.13. Real space kernel of butane ($\rho_a = 1.46$) obtained in the atomic formalism at two different temperatures, $T = 4.05$ and $T = 3.79$: (a) Real space kernels in the atomic formalism obtained from the Lorentzian-type functional form and normalized by $\eta(y = 0)$ value; (b) Real space kernels shown in (a) normalized by the factor ξ_g. Note intermolecular interaction normalization in (b) (dotted and dashed lines).

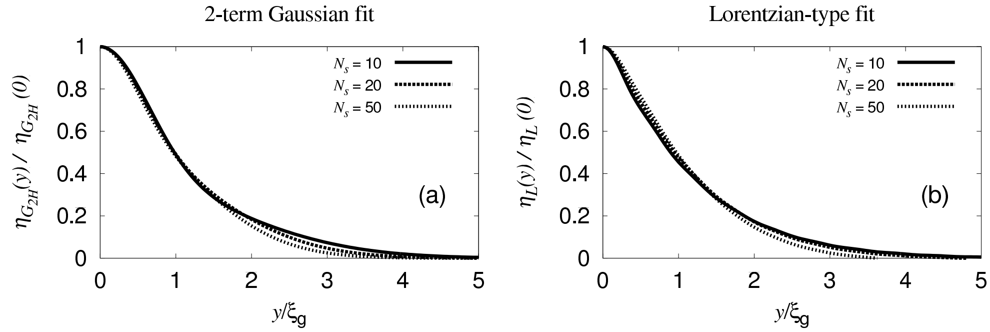

Fig. 4.14. Real space kernel of FJC melts for three different chain lengths: $N_s = 10$, $N_s = 20$, $N_s = 50$: (a) Real space kernels obtained from the equally-weighted two-term Gaussian functional form, Eq. (3.5), normalized by the factor ξ_g; (b) Real space kernels obtained from the Lorentzian-type functional form normalized by the factor ξ_g Eq. (3.7). The corresponding structurally unnormalized kernels are shown in Fig. (4.10).

for these two structures i.e. at $T = 4.05$ (dashed line) and $T = 3.79$ (dotted line).

Figs. 4.14(a) and 4.14(b) depict the FJC kernels in real space according to the atomic definition, normalized with respect to ξ_g and obtained from an equally-weighted two-term Gaussian function and Lorentzian-type function, respectively. We can see that despite the fact that structural normalization procedure preserved the features of the real space kernels, neither Lorentzian-type function nor Gaussian function completely remove the differences between the kernels in Figs. 4.10(a) and 4.10(b). As mentioned above for butane, a more comprehensive structural normalization is needed in order to be able to reduce the viscosity kernels to a universal curve for complex molecular fluids.

4.5 Summary

The main results can be summarized as follows:

(i) An insignificant variation in the shape of both normalized reciprocal space and real space kernels has been noted for the entire range of molecular weights considered here.

(ii) Though a relatively simple Lorentzian-type function fits the data well over a wide range of wavevectors, at all the state points, it is not possible to analytically inverse Fourier transform it to the spatial domain. Therefore, one may consider an expansion up to a four-term Gaussian which also gives a better accuracy compared to the Lorentzian-type function. Even though the parameterization of the reciprocal space kernel has shown that the density and temperature have a great impact on the parameters, the resulting kernels vary only slightly with those temperatures chosen here.

(iii) We identified that the choice of functional forms in reciprocal space plays a significant role in the prediction of the real space kernel shape. For instance, in the case of butane an equally weighted two-term Gaussian function is unsuitable as it distorts the real space kernel and underestimates the local effective viscosities which is consistent with earlier results for monatomic and diatomic fluids. However, for polymeric fluids all the fits reproduce accurately the local effective viscosities even though they have slightly different shapes.

(iv) The viscosity kernels of FENE and FJC chains are essentially the same. Much larger chains would also be worth considering in the future in order to cover the crossover regime from the nonentangled to the entangled state.

(v) Though a normalization scaling based on the correlation length of the radial distribution function allows us to compare the real space kernels of different polymeric melts, in the case of butane, only the inter-molecular contributions in the radial distribution function leads to an improved agreement. This suggests a need for a more comprehensive structural normalization of complex molecular structures.

(vi) Overall, we have shown that the normalized real space viscosity kernel of butane has a width of roughly 3-5 atomic diameters while for polymer melts the width is about 4-6 atomic diameters. This means that the generalized hydrodynamic viscosity must be used in predicting the flow properties of molecular fluids on length scales where the gradient in the strain rate is of the order of these dimensions.

5 Polymers approaching their Glassy State

5.1 Introduction

Generally, molecular systems can exist in three possible physical states: solid, liquid and gas. However, the transitions in polymers are more complex. Firstly, at high temperatures, polymeric molecules decompose rather than boil since what we would consider conventionally as their ”boiling points” are generally higher than their decomposition temperatures. Secondly, a given polymeric sample is composed of a mixture of molecules having different chain lengths (molecular weights). In contrast to simple molecules, the transition between the solid and liquid forms of a polymer is rather diffuse and occurs over a temperature range the magnitude of which (of the order of 2 to 10C) depends on the polydispersity of the polymer. Polymers become very viscous (viscoelastic) fluids on melting, unlike freely flowing low-molecular-weight materials. In addition, there is a more fundamental difference between the thermal behavior of polymers and simple molecules. Molecular motion in a polymer sample is promoted by its thermal energy. It is opposed by the cohesive forces between structural segments (groups of atoms) along the chain and between neighboring chains. These cohesive forces and, consequently, thermal transitions in polymers depend on the structure of the polymer. In this regard, two important temperatures at which certain physical properties of polymers undergo drastic changes, have been identified: the glass transition (GT) temperature, T_g and the crystalline melting point, T_m.

If a polymer is amorphous, the solid-to-liquid transition occurs very gradually, going through an intermediate ”rubbery” state without a phase transformation. The transition from the hard and brittle glass into a softer, rubbery state occurs over a narrow temperature range referred to as the GT temperature. In the case of a partially crystalline polymer, the above transformation occurs only in the amorphous regions. The crystalline zones remain unchanged and act as reinforcing elements thus making the sample hard and tough. If heating is continued, a temperature at which the crystalline zones begin to melt is reached. The equilibrium crystalline melting point, T_m, for polymers corresponds to the temperature at which the last crystallite starts melting. Again, in contrast to simple materials, the value of T_m depends on the degree of crystallinity and size distribution of crystallites.

Thermodynamic transitions are classified as being first- or second-order. In a first-order transition there is a transfer of heat between the system and its surroundings and the system undergoes an abrupt volume change. In a second-order transition, there is no transfer of heat, but the heat capacity does change. The volume changes to accommodate the increased motion of the wiggling chains, but it does not change discontinuously. A GT is known as a ”pseudo-second-order transition” since the discontinuities are not sharp and occur over a range of temperatures. Moreover, a glassy system is not actually in equilibrium because aging phenomena and flow have a non-negligible effect at long times. At best, we refer to a metastable equilibrium which can be treated as an equilibrium system in the case of short experimental times.

Generally speaking, the fundamental nature of the GT is still unclear. It is a complex process that involves equilibrium, thermodynamic and kinetic factors. Various theories of the glass transition exist, such as kinetic, equilibrium [Gibbs 1958, Gibbs 1955] and free volume [Williams 1955] theory. The thermodynamic approach is based on entropy considerations of the glassy state, while the kinetic theory of the glass transition considers the relaxation phenomena associated with the glass transition. Each approach gives only a partial explanation to the observed behavior of polymers [Ebewele 2000].

Historically viscosity has played an important role in analyzing glasses. The GT was associated for practical purposes with a specific number for the viscosity where the material could be considered not to flow during experimental time scales. A body of literature exists on the viscoelastic properties and the behaviour of the viscosity near the glass transition [Varnik 2002, Yamamoto 2002, Wallace 2004]. For instance, the group of K. Binder played a significant role in the computer simulation of glasses in general as well as in polymer glasses [Binder 2003, Binder 2010]. In particular, Binder *et al.* looked at a melt of simple bead spring polymer models. These are the simplest molecular dynamics models and allow, because of their enormous efficiency, to study a rather wide variation of cooling rates which can lead to a very different behaviour and huge jumps in the observed glass transition temperature. Also, the group of P. Harrowell [Harrowell 1993, Harrowell 2010] are currently carrying out detailed analysis of the nature of slow relaxation in some simple models of glass forming liquids using computer simulations and theoretical treatments. More recently Berthier *et al.* [Berthier 2010] investigated the glass transition of a dense fluid of hard spheres [Berthier 2009c, Berthier 2009b] and the dynamic criticality in glass-forming liquids [Berthier 2003, Whitelam 2004, Whitelam 2005].

However, to date there is much less information about the spatial dependence of viscosity. In order to understand the transport in such systems we devote this chapter to the analysis of the spatially dependent viscosity of polymeric fluids, when cooled towards their glass transition temperature. Another contribution of this section is the analysis of the chain length influence on the viscosity kernel. Though our previous results indicate little difference when increasing the chain length to up to 100 beads per chain at the standard state point ($\rho = 0.84$, $T = 1.0$) it is worth looking at much lower temperature regions which might offer an insight into where exactly the onset of large spatial correlations occurs.

We must stress that the main objective is not a precise prediction of the glass transition, but rather an analysis of temperature dependence of the viscosity kernel (i.e. the shape of the kernel) as we approach T_g. Though an impressive number of works exist on glass transition temperature estimation, it is generally difficult to compare all data values because they have been computed for different systems (bulk liquids, films, networks), under different conditions (constant pressure, constant volume), by applying different models (potential energy functions, cutoff distances) for various chain lengths and densities. Nevertheless, we will present the results for self-diffusion coefficients and stress autocorrelation functions which show the characteristics of the glassy state. We also estimate the value of T_g and compare the values with previous works where possible.

Our simulation methods have been described in detail in the previous section. In brief, we employ a freely jointed tangent chain model (FJC) and the Kremer-Grest model [Kremer 1990] to simulate three polymeric systems:

(i) In the first system each molecule consists of N_s sites of equal mass $m_{i\alpha}$ interacting via a truncated ($r_c = 2^{1/6}$) and shifted Lennard-Jones (LJ) potential (or Weeks-Chandler-Andersen (WCA) interaction, Eq. (2.1) [Weeks 1971]. The sites are joined by rigidly constrained bonds of length $l = \sigma$. The WCA interactions in this model can occur between any two different sites except those connected by a bond. This case will be termed, for simplicity, FJC-WCA system.

(ii) In the second system we also include the attractive part of the shifted LJ interaction by letting $r_c = 2.5\sigma$. This case will be termed FJC-LJ system.

(iii) In the third system, termed as FENE-LJ, in addition to the LJ potential, adjacent connected beads also interact through a FENE potential. The LJ potential cutoff distance was $r_c = 2.5\sigma$.

A series of three different systems composed of different molecular sizes consisting of 10-, 20- and 50-site molecules were studied. The reduced site number density was $\rho_a = 0.84$.

The fifth-order Gear predictor corrector algorithm was employed to solve the equations of motion [Gear 1966, Gear 1971], and the thermostatted equations of motion are given in Sec. 2.4.

After an equilibration run of length 10^6 times steps at low density, the molecular systems were compressed to the required density and re-equilibrated for 10^6 time steps. A total of 1.4×10^7 time steps was used to compute the ACF at each state point by ensemble averaging 14 independent runs, each of length 10^6 steps. The transverse momentum density ACFs were computed over at least 20 reduced time units for 10-site molecules and over at least 40 reduced time units for 50-site molecules. The stress ACFs were computed over at least 40 and 80 reduced time units for 10-site and 50-site molecules, respectively. Several very long test runs over 200, 400 and 600 reduced time units for 10-, 20- and 50-site molecules were also carried out at very low temperatures where a much slower convergence of the integral stress ACF occurs. By cooling down the polymer melts, conventional MD simulations become unfeasible due to the enormously large relaxation times. Therefore, in addition to the ACFs, we have employed a widely used fitting procedure (see Sec. 5.3) in which the stress ACF is extrapolated to much larger time values.

The results presented below were obtained by simulation of 864 molecules in the isokinetic molecular dynamics ensemble [Puscasu 2010a][4]. In order to validate our code and results we reproduced and compared previous results for self-diffusion and wave-vector and frequency dependent viscosities where possible. Very good agreement was found in all cases. We must also note that all our correlation functions were evaluated for both 108 and 864 molecule systems in order to determine whether the results were system size dependent. No such evidence was observed within statistical uncertainties either at relatively high temperatures or down to the glass transition region.

5.2 Self-diffusion coefficient and glass transition temperature

The self-diffusion coefficient can be obtained either from the mean square displacement or via the Green-Kubo relation. In this work we evaluate the integral

$$D = \frac{1}{3m_i^2} \int_0^\infty dt \langle \mathbf{p}_i(t) \mathbf{p}_i(0) \rangle. \tag{5.1}$$

The momenta $\mathbf{p}_i$ can be interpreted either as the momentum of an individual atom or as the center of mass momentum of a molecule. In this work we use the latter interpretation.

Figs. 5.1(a-c) depict the dependence of the self-diffusion as a function of temperature T and Figs. (5.2-5.4) depict the velocity correlation functions (VACFs) along with their running integrals.

A comparison of the velocity ACF of a 20-site FENE-LJ, Fig. 5.2(c), with those of Hunt and Todd [Hunt 2009b] at the lowest strain rate and for the highest temperature shows an excellent agreement. However, in order to limit the number of figures, we only show the results for the

---

[4] This section contains material reprinted with permission from R. M. Puscasu *et al.*, J. Chem. Phys. **133**, 144907 (2010). Copyright 2010, American Institute of Physics.

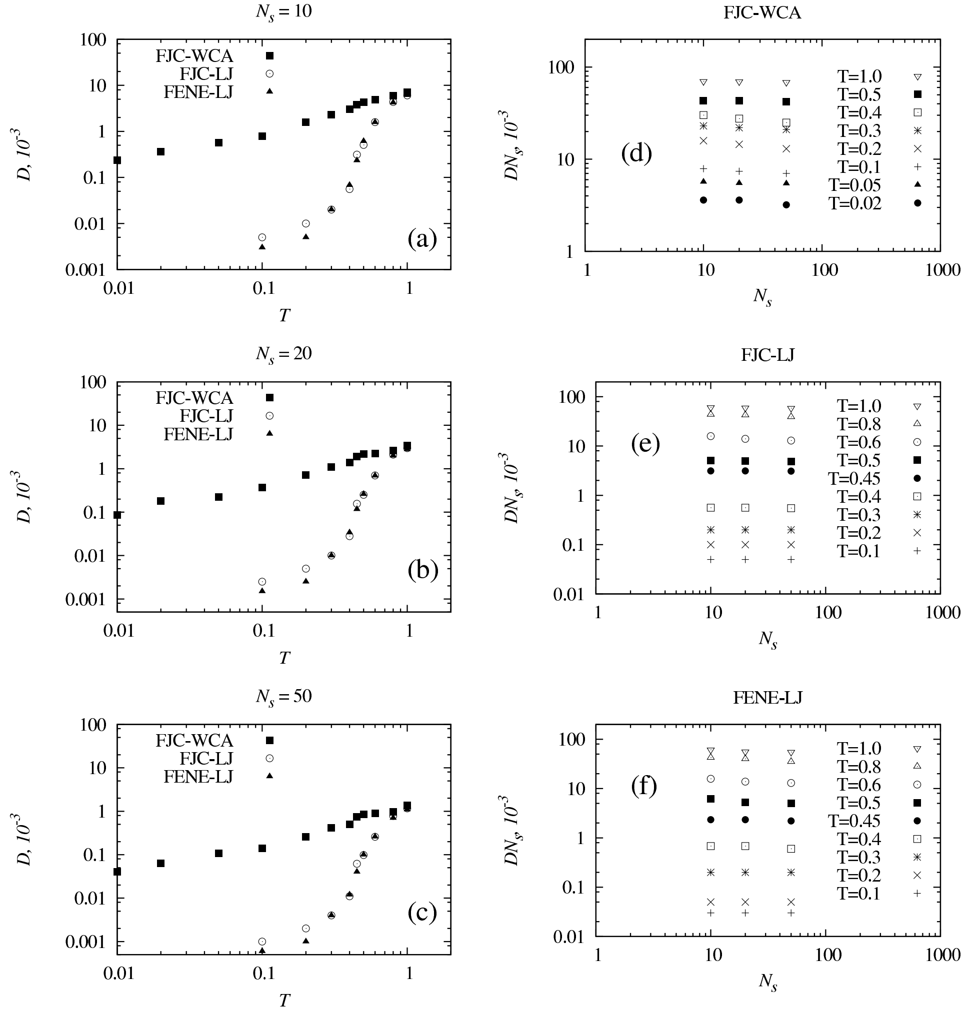

Fig. 5.1. Equilibrium diffusion coefficient D for FJC-WCA, FJC-LJ and FENE-LJ at different temperatures T and for three chain lengths: (a) D vs. T for $N_s = 10$; (b) D vs. T for $N_s = 20$; (c) D vs. T for $N_s = 50$; (d) DN_s vs. N_s for FJC-WCA; (e) DN_s vs. N_s for FJC-LJ; (f) DN_s vs. N_s for FENE-LJ. The dynamics of the systems is characteristic for a Rouse model.

self-diffusion coefficient and velocity ACFs for a few state points and system sizes. The complete set of correlation function results are available from the author.

Each of the velocity ACFs in Figs. (5.2-5.4)(a,c) begins with a peak at $t = 0$ and decays to zero as t increases. In FENE-LJ and FJC-LJ systems at low temperatures the ACFs have also a shallow minimum before an increase to zero. As it is expected, the initial values of the velocity ACFs are linearly proportional to the temperature and inversely proportional to the chain length for all three systems. Looking at the correlation functions for FENE-LJ and FJC-LJ polymer melts at the same temperature we can see that the ACFs and their running integrals are almost indistinguishable both in the low-time region as well as in their long-time behaviours shown in the insets. For temperatures below the glass transition temperature the ACFs even become

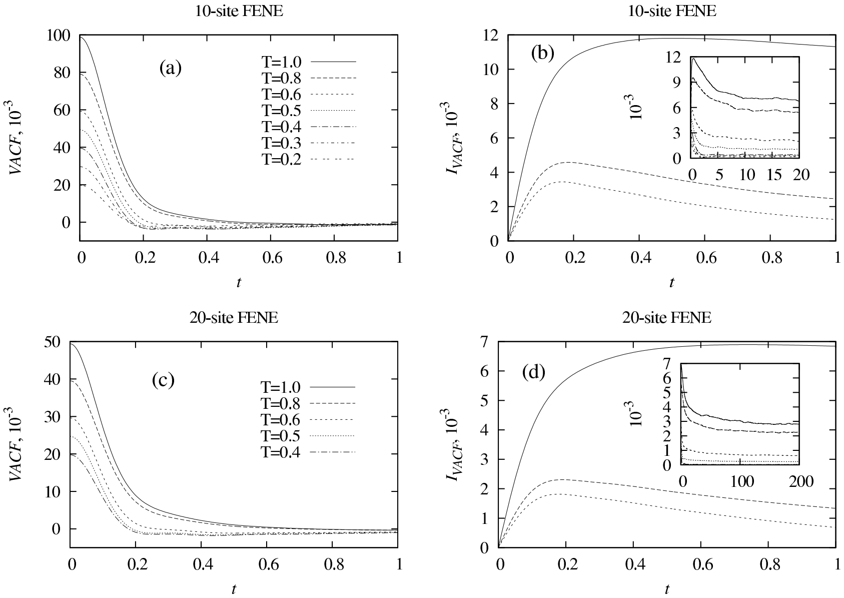

Fig. 5.2. Velocity ACFs as a function of temperature for a FENE-LJ polymer melt: (a) Velocity ACF of a 10-site chain function of temperature; (b) Velocity ACF integral of a 10-site chain function of temperature; (c) Velocity ACF of a 20-site chain function of temperature; (d) Velocity ACF integral of a 20-site chain function of temperature. The insets show the long-time behaviour.

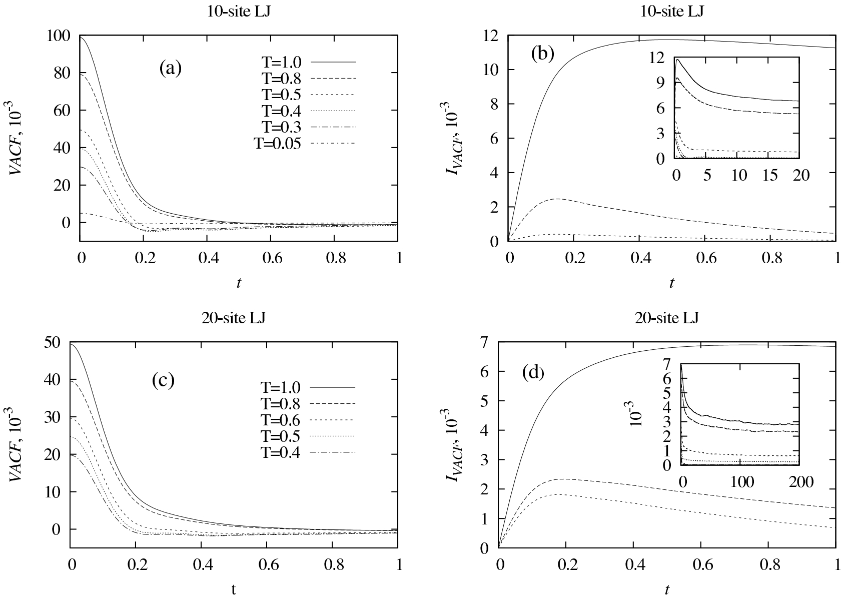

Fig. 5.3. Velocity ACFs as function of temperature for a FJC-LJ polymer melt: (a) Velocity ACF of a 10-site chain function of temperature; (b) Velocity ACF integral of a 10-site chain function of temperature; (c) Velocity ACF of a 20-site chain function of temperature; (d) Velocity ACF integral of a 20-site chain function of temperature. The insets show the long-time behaviour.

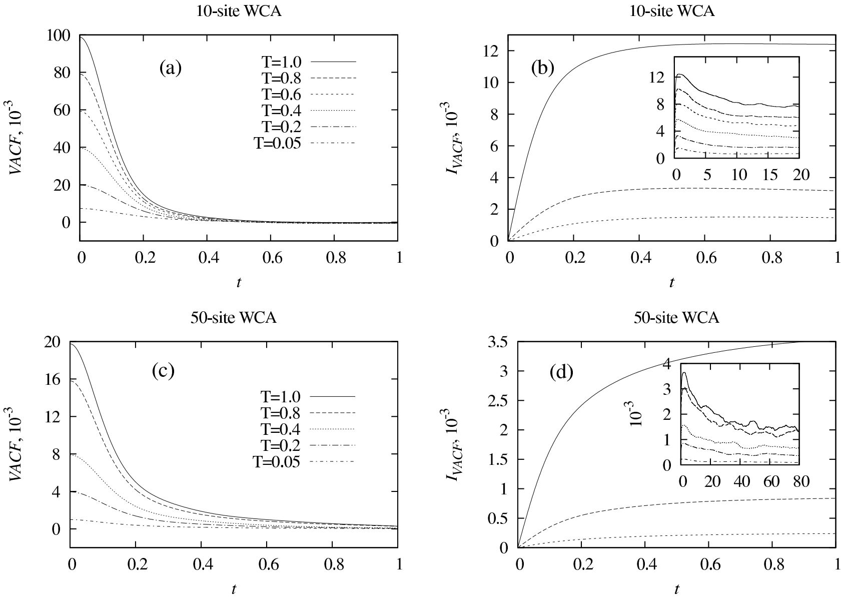

Fig. 5.4. Velocity ACFs as function of temperature for a FJC-WCA polymer melt: (a) Velocity ACF of a 10-site chain function of temperature; (b) Velocity ACF integral of a 10-site chain function of temperature; (c) Velocity ACF of a 50-site chain function of temperature; (d) Velocity ACF integral of a 50-site chain function of temperature. The insets show the long-time behaviour.

negative and then gradually increase to zero. At high temperatures, similar trends are found in the FJC-WCA melts. However, below $T = 0.8$ the trend of the ACFs for FJC-WCA melts is quite different compared to FJC-LJ melts. Furthermore, for FJC-WCA systems no negative values in the velocity ACFs were noticed, Fig. 5.4(a,c). Consequently, the integration of the above mentioned VACFs for FJC-WCA systems over the entire time space is likely to lead very different self-diffusion coefficients compared to the other systems.

In Figures 5.1(a-c), the dependence of the self-diffusion coefficient as a function of temperature T follows the expected behaviour: higher temperatures lead to higher diffusion coefficients and D decreases as N_s increases. However, for the FJC-WCA system, the diffusion coefficient seems to vanish at a much lower temperature compared to the other systems, i.e. $T_g^{FJC-WCA} < 0.01$ at $\rho = 0.84$. For this model one should recover a hard sphere potential [Berthier 2009c, Berthier 2009b]. This explains why it appears the diffusion constant is approaching a limiting constant value at low temperature [McCormick 2005]. Such systems exhibit a rather topologically induced glass transition which is controlled exclusively by chain structure since energy barriers do not exist for the hard sphere potential [Rosche 2000]. For a hard core model the temperatures and density chosen here are too low to furnish sufficient packing constraints to drive the glass transition, hence the glass aspects are weak. Therefore our results for the FJC-WCA model deal with a slightly supercooled liquid above the glass transition.

The glass transition temperature for the FJC-LJ and FENE-LJ polymer melts is considerably higher. This is generally explained by the fact that the diffusion is significantly reduced by the second LJ coordination shell which falls within the attractive region of the potential. For these systems $T_g^{FJC/FENE-LJ} \approx 0.40 - 0.45$ at $\rho = 0.84$. Later we find further evidence of the glass transition by investigating the zero wave-vector stress autocorrelation function. Our results for the self-diffusion are in agreement with those previously reported by Bennemann *et. al* for an identical system [Bennemann 1998]. It is also seen that for all chain lengths, Figs. 5.1(a-c), the data points collapse onto one curve at around $T = 1$ and above this temperature, there is no difference in the diffusion for different model chains at the same N_s, as found previously by Kremer and Grest [Kremer 1990].

The FJC-WCA system is not likely to undergo a sharp transition at the temperatures simulated here and should only be considered as an estimate of the interval associated with the glass transition. These results are consistent with those of Bulacu *et al.* [Bulacu 2007] though their suggested T_g for a similar system was 0.05. A more accurate estimation of the T_g would be necessary either by conducting simulations at lower temperatures or by fitting D as a function of T with different theoretical or empirical equations [Götze 1992]. Both methods are somewhat troublesome; equilibrium MD simulations are not accurate enough to distinguish between exponentially small and strictly zero values of D and the fitting procedure is weakly dependent on the temperature interval used. Since T_g is not our primary interest we did not perform such estimations.

Figs. 5.1(d-f) show the self-diffusion coefficient as a function of chain length at temperatures ranging from well below T_g to above T_g. At all temperatures, the chains behave approximately according to the Rouse theory for all three system types. The diffusion coefficient is inversely proportional to the chain length (hence viscosity should be directly proportional to N_s) which is consistent with our polymeric chains being not long enough to cover the crossover regime from the nonentangled to the entangled state, in agreement with previous observations [Kröger 2000].

5.3 Momentum density and stress correlation functions

The transverse momentum density ACF expressed by Eq. (1.53) and their running integrals, Eq. (1.54), are shown in Figs. 5.5, 5.6 and 5.7 for FJC-WCA, FJC-LJ and FENE-LJ systems respectively. Again, in order to limit the number of figures we only show here results for a 10-site system and for mode number $n = 2$. While $C_\perp(k_y, t)$ in all three models look similar, the running integrals in the case of FJC-WCA chain behave differently from FJC-LJ and FENE-LJ chains as we lower the temperature.

Figs. 5.5(a-d) show clear evidence that the FJC-WCA system, which contains only the repulsive part of the LJ potential, is unlikely to undergo a structural arrest even at $T = 0.05$.

A further examination of Figs. 5.5(a) and (b), 5.6(a) and (b), and 5.7(a) and (b) shows that in the atomic representation the zero time momentum density ACFs slightly differ from the molecular ones. As mentioned in the previous section, this is a consequence of correlations between the momenta of different sites on the same molecule that are involved in bond angle or bond length constraints. As a consequence, there is no longer a simple relationship between the temperature and the zero time value of the momentum density ACF. As discussed in the previous section, this is a consequence of correlations between the momenta of different sites on the same molecule that are involved in bond angle or bond length constraints (see Evans and Morriss, Chapter 4. Eq. (37) in [Evans 1990]). Therefore the y-intercepts in Figs. (5.5-5.7) are computed from the correlation function in Eq. (1.53) and not from the temperature, Eq. (1.55).

The stress autocorrelation function expressed by Eq. (1.57) and their running integrals expressed by Eq. (1.60) are shown in Figs. 5.8, 5.9 and 5.10 for FJC-WCA, FJC-LJ and FENE-LJ

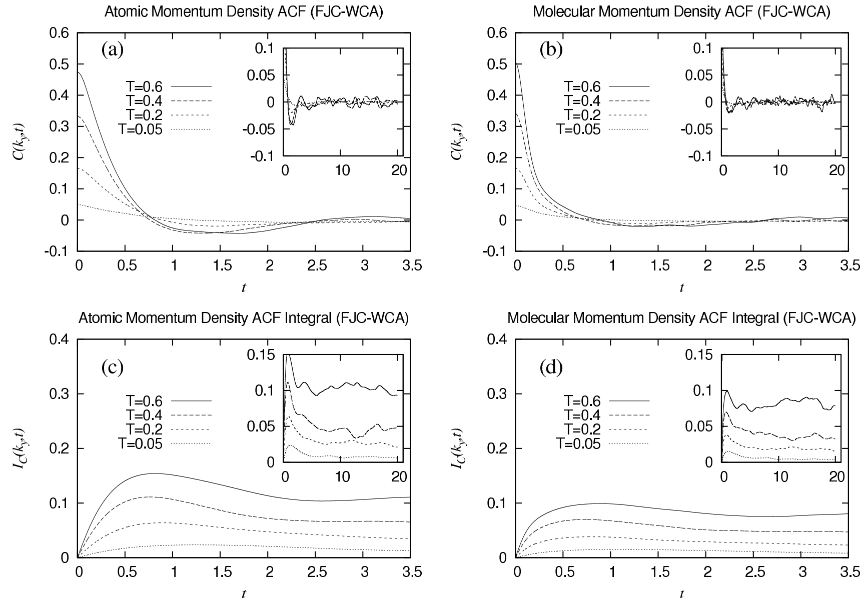

Fig. 5.5. Momentum density ACFs as function of temperature for a 10-site FJC-WCA chain: (a) Atomic transverse momentum density ACFs; (b) Molecular transverse momentum density ACFs; (c) Integral of the atomic transverse momentum density ACFs; (d) Integral of the molecular transverse momentum density ACFs. The mode number is $n = 2$. The insets show the long-time behaviours.

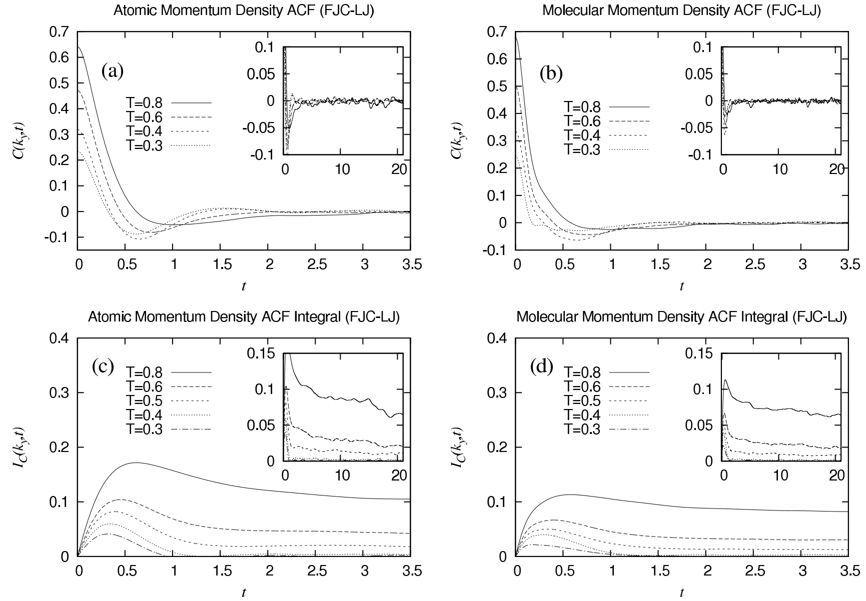

Fig. 5.6. Momentum density ACFs as function of temperature for a 10-site FJC-LJ chain: (a) Atomic transverse momentum density ACFs; (b) Molecular transverse momentum density ACFs; (c) Integral of the atomic transverse momentum density ACFs; (d) Integral of the molecular transverse momentum density ACFs. The mode number is $n = 2$. The insets show the long-time behaviours.

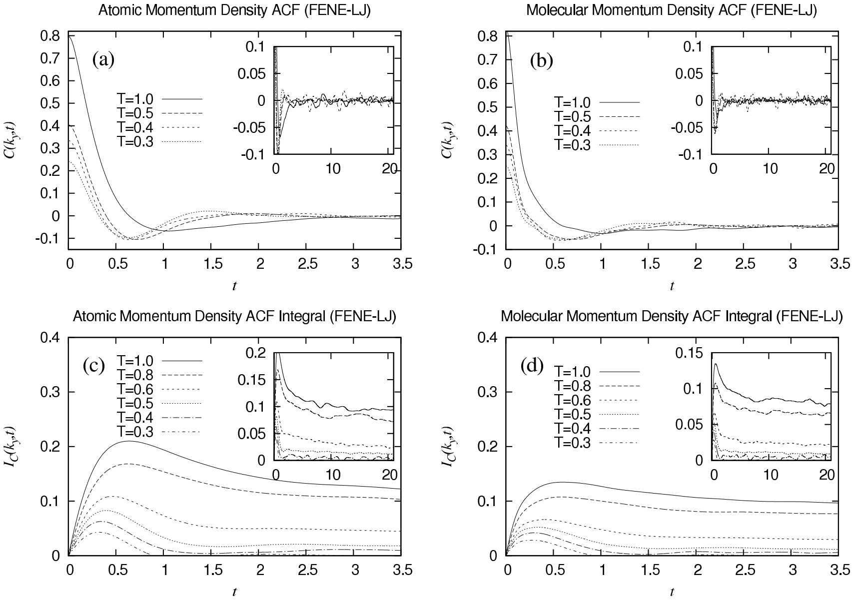

Fig. 5.7. Momentum density ACFs as function of temperature for a 10-site FENE-LJ chain: (a) Atomic transverse momentum density ACFs; (b) Molecular transverse momentum density ACFs; (c) Integral of the atomic transverse momentum density ACFs; (d) Integral of the molecular transverse momentum density ACFs. The mode number is $n = 2$. The insets show the long-time behaviours.

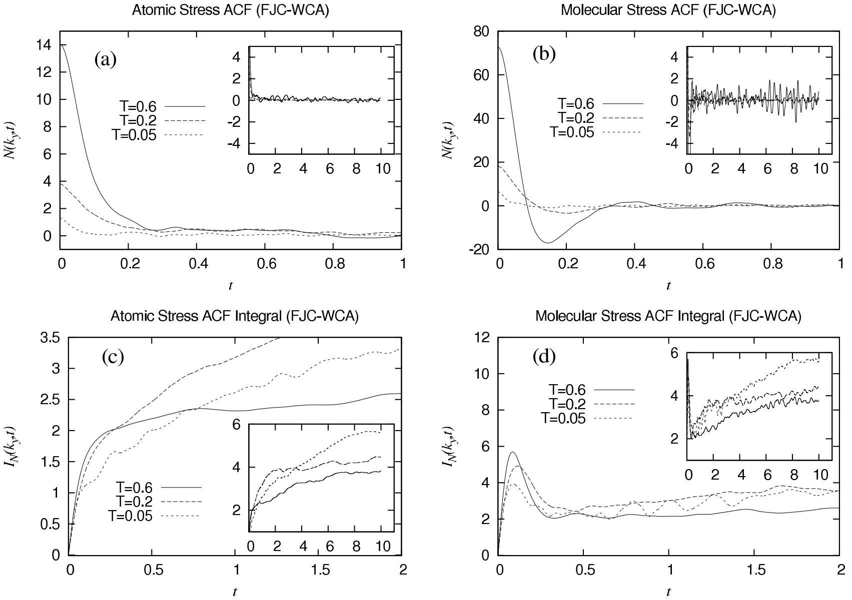

Fig. 5.8. Stress ACFs as function of temperature for a 10-site FJC-WCA chain: (a) Atomic stress ACFs; (b) Molecular stress ACFs; (c) Integral of the atomic stress ACFs; (d) Integral of the molecular stress ACFs. The insets show the long-time behaviours. Estimated glass transition temperature is $T_g \approx 0.40 - 0.45$.

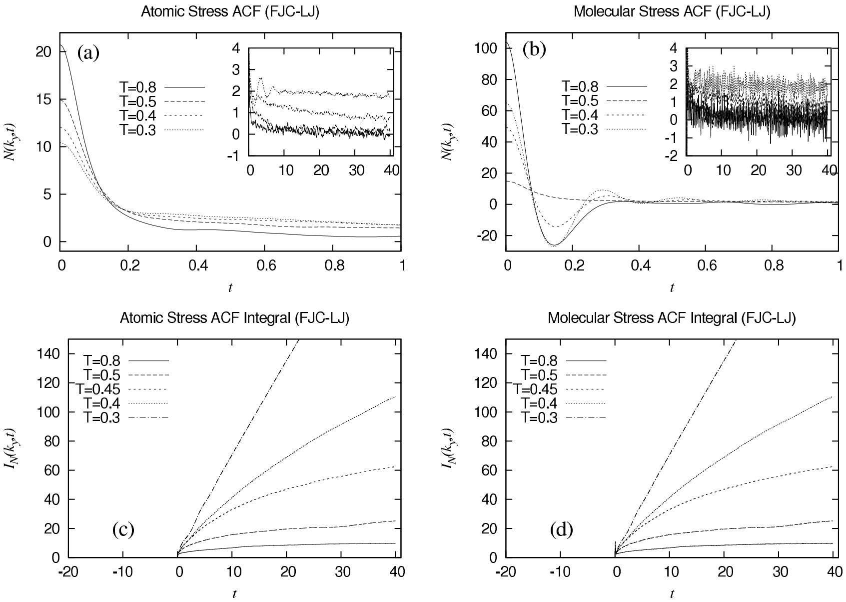

Fig. 5.9. Stress ACFs as function of temperature for a 10-site FJC-LJ chain: (a) Atomic stress ACFs; (b) Molecular stress ACFs; (c) Integral of the atomic stress ACFs; (d) Integral of the molecular stress ACFs. The insets show the long-time behaviours. Estimated glass transition temperature is $T_g \approx 0.40 - 0.45$.

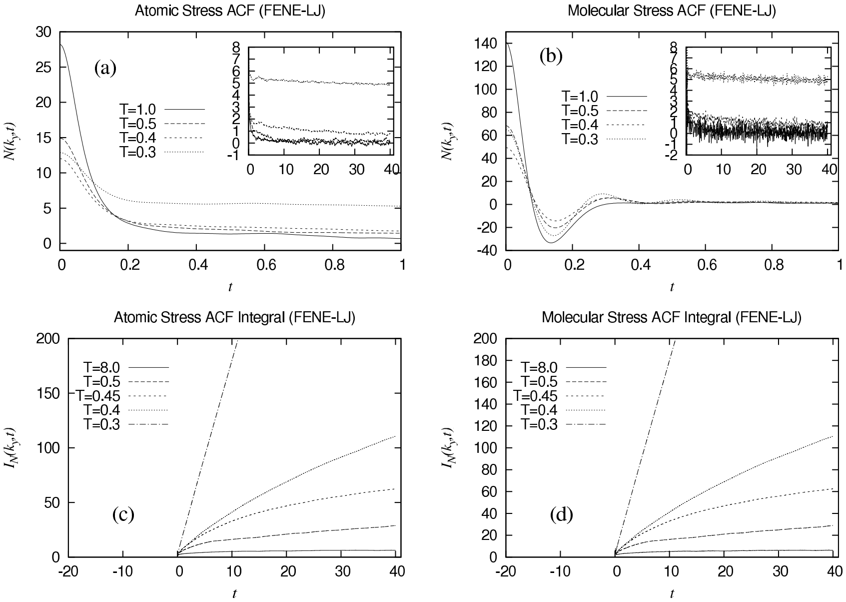

Fig. 5.10. Stress ACFs as function of temperature for a 10-site FENE-LJ chain: (a) Atomic stress ACFs; (b) Molecular stress ACFs; (c) Integral of the atomic stress ACFs; (d) Integral of the molecular stress ACFs. The insets show the long-time behaviours. Estimated glass transition temperature is $T_g \approx 0.40 - 0.45$.

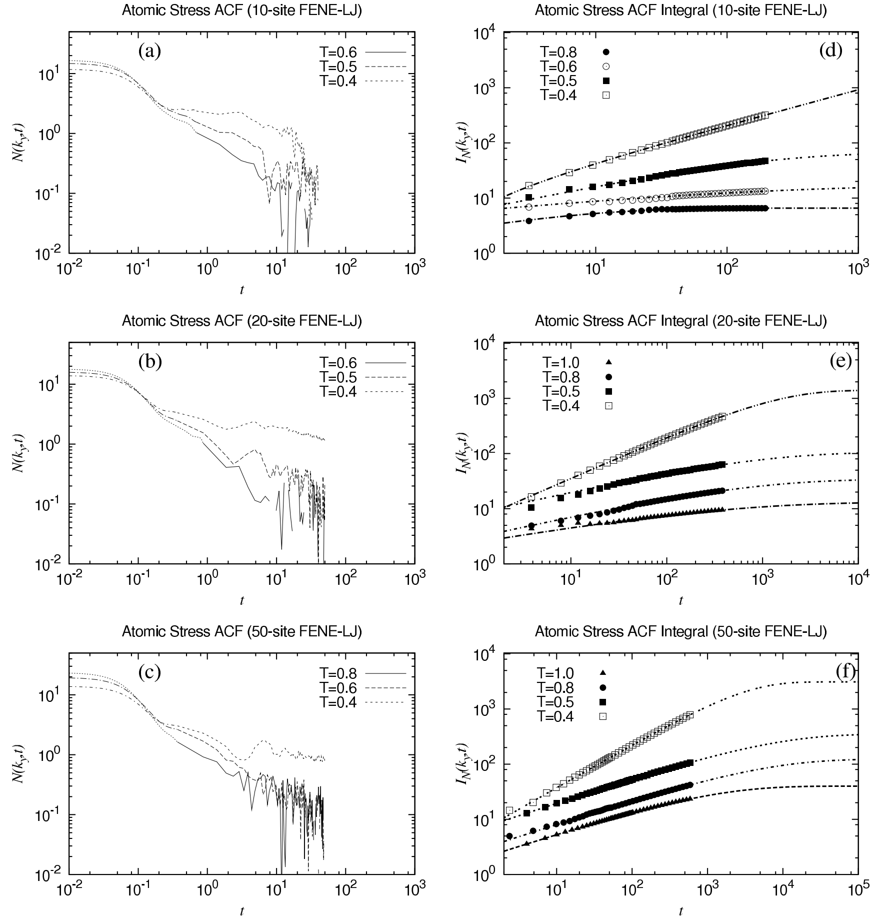

Fig. 5.11. Atomic stress ACF and running integrals at different temperatures for a 10-, 20- and 50-site FENE-LJ chain: (a) 10-site stress ACFs; (b) 20-site stress ACFs; (c) 50-site stress ACFs; (d) 10-site integral stress ACFs; (e) 20-site integral stress ACFs; (f) 50-site integral stress ACFs. The time extensions in (d-f) have been obtained from a fit based on Eq. (5.2) except for $T = 0.4$ in (a) where a power law, Eq. (5.3), was used. We note that in (e) and (f) the stretched-exponential fits the data slightly better compared to the power law, but due to the lack of data, we suggest the former underestimates the limiting value. The value of the exponent characterizing the power law was found to be approximately $\theta = 0.64$ for $N_s = 10$.

chains respectively. In contrast to the FJC-WCA model, in the FJC-LJ and FENE-LJ chains, the relaxation increases monotonically with decreasing temperature until a specific temperature is reached. At this temperature a sudden increase of the relaxation occurs indicating a strong slowing down of the chain dynamics. This temperature is very similar to the one obtained from the vanishing of the diffusion coefficient D, Fig. 5.1(a-c).

In addition to the above mentioned stress correlation functions calculated over 40 reduced time units, we also performed longer test runs over at least 200, 400 and 600 reduced time units for 10-, 20- and 50-site molecules respectively. The log-log stress atomic ACFs, for three different chain lengths, are displayed in Fig. 5.11(a-c) and their corresponding running integrals

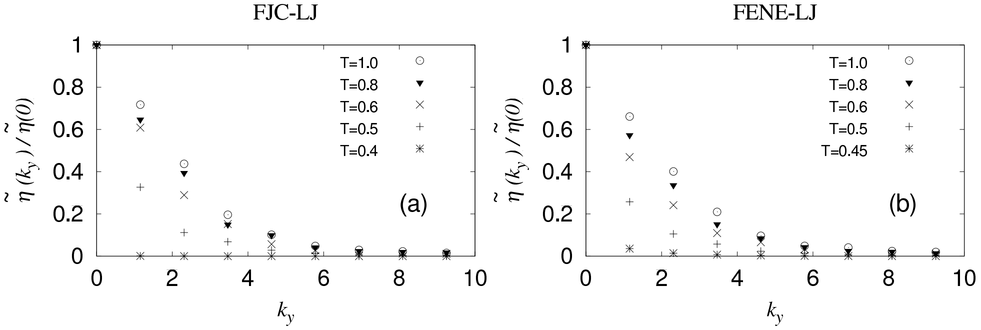

Fig. 5.12. Reciprocal space kernel of 10-site FJC-LJ and FENE-LJ melts at different temperatures in the atomic formalism: (a) Normalized kernels for FJC-LJ; (b) Normalized kernels for FENE-LJ.

are displayed in Fig. 5.11(d-f). As can be seen in Fig. 5.11(d-f), it is necessary to extend the ACF to times longer than actually observed to ensure convergence of the integral. In such situations, the stress correlation functions are usually fitted to the Kohlarausch-Williams-Watts (KWW) (or stretched-exponential) function above T_g and to a power law form below T_g [Wallace 2004]. Instead of fitting the ACFs in Fig. 5.11(a-c), we will use the running integrals, Figs. 5.11(d-f), to tune the fitting parameters. The latter method reduces the noise and gives better convergence. The stretched-exponential functional form is

$$I_N^{KWW}(k_y = 0, t) = I_N(0,0)\big[1 - \exp(-\gamma t^{\theta})\big], \tag{5.2}$$

and the power law functional form is

$$I_N^{pow}(k_y = 0, t) = A + Bt^{\phi}. \tag{5.3}$$

It is important to note that the values of fitting parameters depend weakly on where the fit starts. The fits are shown in Fig. 5.11 and cover all times beyond $t = 0.4$.

5.4 Reciprocal space viscosity kernel

The reciprocal space kernels in the atomic formulation for FJC-LJ and FENE-LJ systems are shown in Fig. 5.12. The statistical reliability of non-zero wavevector kernel data increases as k_y increases. The error bars for these components are of the same size as the symbols and are therefore omitted in all figures. For the zero wavevector component the main source of error at temperatures approaching the glass transition is associated with the fitting procedure.

The kernels in Fig. 5.12 are normalized with respect to the zero wavevector values which are given in Table 5.1. For higher temperatures, our results for the zero wavevector viscosity are in agreement with those reported previously by Daivis *et al.* [Daivis 2007] and Kröger *et al.* [Kröger 1993], but are slightly lower compared to Wallace *et al.* [Wallace 2004] especially for temperatures close to T_g. Some of the previously reported results are taken as limiting values of the shear rate dependent viscosities at zero strain rate. Nevertheless, they agree within the

Tab. 5.1. Zero wavevector, zero frequency viscosity obtained via Eq. (1.60) for different temperatures and chain lengths

Number of sites	N_s	10	20	50
	T		η_0	
FENE-LJ	1.0	8.1	15.3	42.8
	0.8	9.3	30.2	105
	0.6	20	50	150
	0.5	80	110	200
	0.45		$\approx 10^3$	
	0.4		$\approx 10^4$	
FJC-WCA	1.0	8.09	15.2	41.2
	0.8	9.3	17.0	44.5
	0.6	10	18	47
	0.4	12	21	52
	0.2	17	29	61
	0.1	25	38	72
	0.05	41	56	93
	0.02	67	81	117

statistical uncertainty.

The kernels of FJC-LJ and FENE-LJ chains are almost identical and therefore only FENE-LJ results are considered further in this chapter. The similarity of these two molecules has also been confirmed by Hunt and Todd [Hunt 2009a, Hunt 2009b] for shear viscosities, extensional viscosities and diffusion tensor.

We have previously found that two relatively simple functional forms could be used to extract the wavevector dependent viscosities for a polymer melt, namely, a Gaussian function and a Lorentzian-type function. As pointed out in our previous section, the inclusion of additional terms in the Gaussian sum yields a better fit and makes the Gaussian function a suitable analytical approximation of the reciprocal space viscosity kernel. However, a Gaussian function with higher number of terms may result in unnatural behaviour of the kernel with unphysical distortions in the real space kernels. By contrast, the Lorentzian-type function shows a much smoother shape of the real space kernels. The fitted parameter values for both functional forms are given in Table 5.2 and the results of the fitting are shown in Fig. 5.13.

Tab. 5.2. Parameter values of the Gaussian and Lorentzian-type fits for a 10-site FENE-LJ chain at different temperatures

	T	1.0	0.8	0.6	0.5	0.45	0.4
	η_0	8.1	9.3	20	80	10^3	10^4
2-term Gaussian Eq. (3.1)	A	0.605	0.528	0.366	0.166	0.023	0.006
	σ_1	2.454	2.351	2.416	2.426	2.364	1.993
	σ_2	0.745	0.674	0.672	0.578	0.402	0.342
Lorentzian-type Eq. (3.2)	α	0.327	0.497	0.811	2.182	19.5	55.5
	β	2.057	1.940	1.854	1.777	1.639	1.200

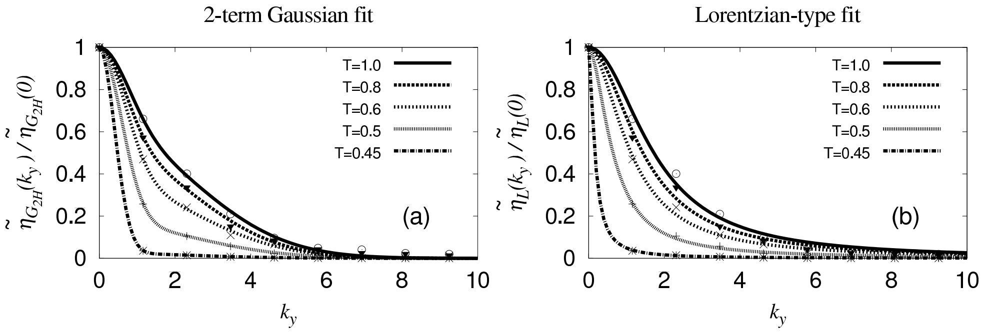

Fig. 5.13. Normalized reciprocal space kernel data of a 10-site FENE-LJ chain and the fits to the (a) two-term Gaussian functional form Eq. (3.2) and (b) Lorentzian-type functional form Eq. (3.2).

In order to test the iterative fitting procedure the magnitude of the residuals was estimated using the residual standard deviation defined by Eq. (3.3). The results of the fitting parameters as a function of temperature for different chain lengths are plotted in Fig. 5.14.

It is interesting to see whether η_0 obeys a Vogel-Fulcher-Tamman (VFT)-law [Varnik 2002]

$$\eta^{VFT}(T) = \eta(\infty) \exp[c/(T - T_0)], \tag{5.4}$$

where $\eta(\infty)$ is the shear viscosity at infinite temperature, c is a constant, and T_0 is the temperature where the shear viscosity is expected to diverge. Fitting our data for all three chain lengths to Eq. (5.4), we obtained $\eta(\infty) = 4.5 \pm 0.1$, $c = 0.306 \pm 0.005$ and $T_0 = 0.393 \pm 0.001$ for a 10-site chain; $\eta(\infty) = 18.2 \pm 4.8$, $c = 0.16 \pm 0.04$, $T_0 = 0.395 \pm 0.007$ for a 20-site chain and $\eta(\infty) = 46.8 \pm 13.5$, $c = 0.14 \pm 0.05$, $T_0 = 0.40 \pm 0.01$ for a 50-site chain. It should be mentioned that Varnik *et al.* [Varnik 2002] reported $\eta(\infty) = 13.23 \pm 0.13$, $c = 0.615 \pm 0.036$ and $T_0 = 0.19 \pm 0.005$ for a similar 10-site chain model, however, they introduced an additional potential barrier acting on the monomers in a layered confined system. We can see that $T_0 \approx 0.39$ is close to the estimated glass transition temperature from the calculations of self-diffusion. As shown in Fig. 5.14(a), the quality of the fit is very good for the 10-site molecule. However, as we have already mentioned, our data are not reliable below $T = 0.45$. Here correlation functions decay very slowly in time and the fitting procedure must be extended over much larger delay times.

The differences between the data and the fits are shown in Figs. 5.15(a) and (b) and confirm that a relatively simple two-term Gaussian functional form reproduces the kernel data with a similar accuracy ($\approx 1 - 3\%$) as the Lorentzian-type does. While generally a fourth term in the Gaussian function improves the fit, it makes the Gaussian expansion of the reciprocal space kernel less convenient. At low temperatures the difference between the Lorentzian-type fit and the Gaussian fit (except equally-weighted two-term Gaussian at first non-zero wavevector value) becomes lower ($\approx 1\%$) due to a delta function like behaviour of the viscosity data.

Table 5.1 clearly suggests that the Rouse model of the viscosity breaks down as we lower the temperature and it is therefore of interest to quantify the product $D\eta_0$ as a function of temperature and chain length. In order to quantify the Rouse failure and the break down of the Stokes-Einstein

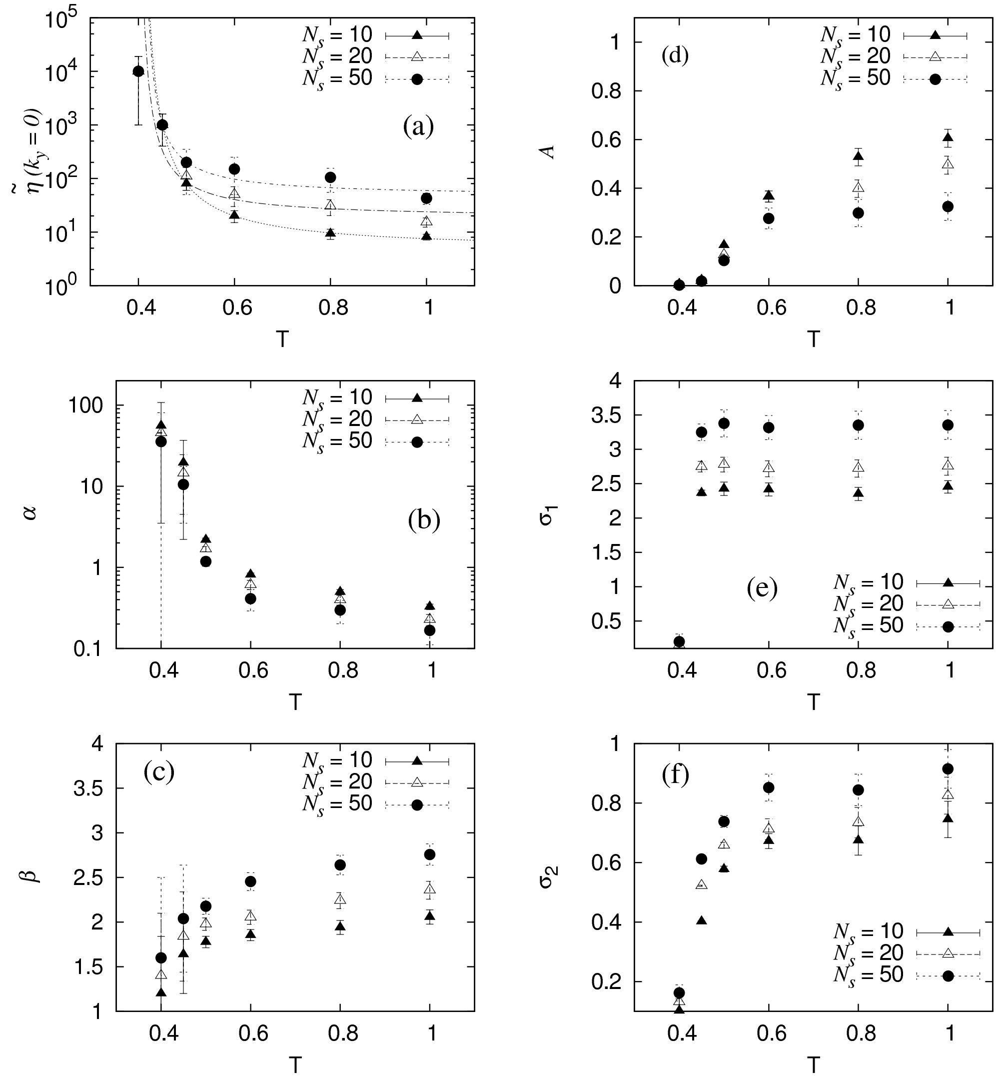

Fig. 5.14. Temperature dependence of the fitting parameters as a function of chain length for a FENE-LJ chain in the atomic formalism: (a) Temperature dependence of zero wavevector, zero frequency viscosity. Also shown are best fits with the VFT expression; (b) and (c) Temperature dependence of parameter α and β Eq. (3.2); (d-f) Temperature dependence of parameter A, σ_1 and σ_2 respectively. In (a) the error bars are based on averages over the test runs and in (b-f) the errors represent the asymptotic standard errors.

relation we plot the product $D\eta_0$ as a function of T and N_s in Fig. 5.16. In contrast to the self-diffusion coefficient presented in Sec. 5.2 for which the N_s scaling of the center of mass D is very simple and Rouse like irrespective of temperature (Fig. 5.1), the Rouse-type scaling of the viscosity for FENE-LJ polymer melts is only seen at high temperatures with a strong deviation

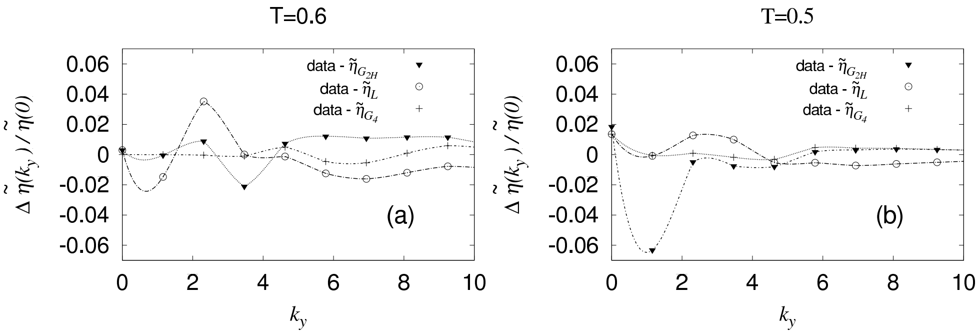

Fig. 5.15. Differences between the reciprocal space kernels of a 10-site FENE-LJ chain at two different temperatures: (a) $T = 0.6$; (b) $T = 0.5$. The lines serve as a guide to the eye.

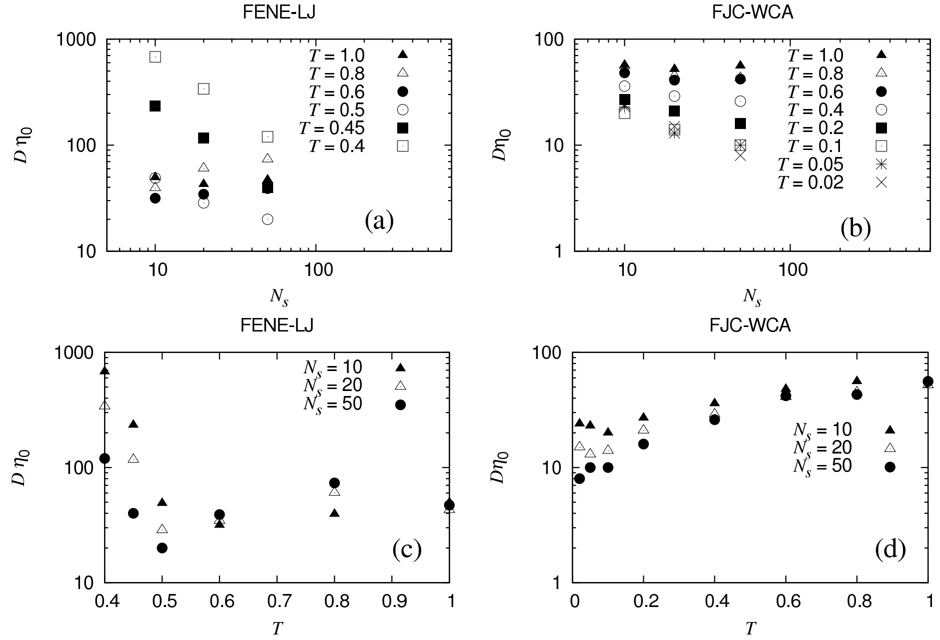

Fig. 5.16. Temperature and chain length dependence of $D\eta_0$: (a) $D\eta_0$ vs. N for FENE-LJ polymer melts; (b) $D\eta_0$ vs. N for FENE-WCA polymer melts; (c) $D\eta_0$ vs. T for FENE-LJ polymer melts; (d) $D\eta_0$ vs. T for FENE-WCA polymer melts.

at $T = 0.8$ (Table 5.1). For the FJC-WCA systems the viscosity is Rouse like down to around $T = 0.4$. Below this temperature $D\eta_0$ follows a power law for both FENE-LJ and FJC-WCA systems. More evidence for the slowing down of the dynamics can be seen in the temperature dependence of $D\eta_0$ shown in Fig. 5.16(c,d).

There are two reasons that can explain the observed behaviour. One is related to the extrapolation of the stress ACF integrals. If we recall that η_0 was taken as a limiting value based

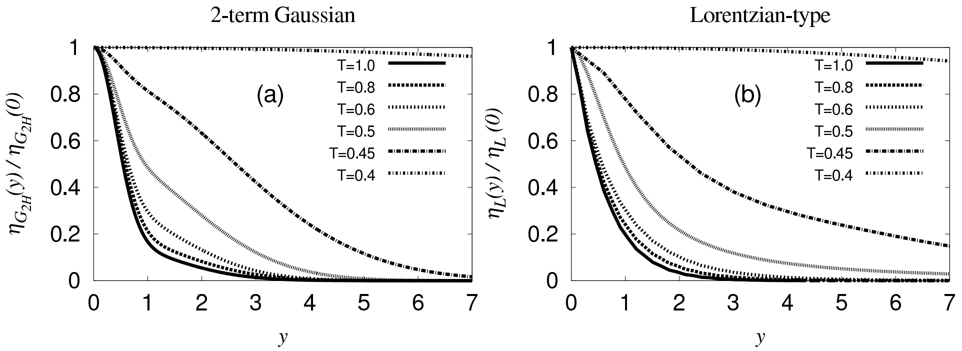

Fig. 5.17. Real space kernel of a 10-site FENE-LJ melt obtained numerically from the Lorentzian-type functional form Eq. (3.2) for different temperatures and normalized by $\eta(y = 0)$.

on stretched exponential and power law fits, Eqs. (5.2,5.3), given in Figs. 5.11(d,e,f), which becomes very sensitive to the interval used in the fitting in the absence of data at high time values as we lower the temperature below $T = 0.6$. Hence the product $D\eta_0$ is not accurate enough in the low-T regime. When much longer simulations are employed we expect a better agreement with the Rouse model prediction down to $T = 0.5$. The second reason relates to the crossing over between the two distinct regimes. This occurs at a temperature $0.45 < T < 0.5$ for FENE-LJ systems, Fig. 5.16(c), and $T < 0.1$ for FJC-WCA systems, Fig. 5.16(d) which is found to correspond well to the thermal decoupling associated with dynamic heterogeneity (as seen later in Sec. 5.5).

5.5 Real space viscosity kernel

The real space kernels of a 10-site FENE-LJ chain obtained analytically via a Gaussian function Eq. (3.4) and numerically via a Lorentzian-type function Eq. (3.4), are presented in Fig. 5.17. We can see that the width of the kernel is roughly 4-6 atomic diameters at $T = 1.0$. As mentioned previously, the reciprocal space kernel of both FJC-WCA and FENE-LJ chains decreases with decreasing temperature. This means that the real space kernel will increase with decreasing temperature. By cooling the melts down to $T = 0.5$, the width of the kernel increases to at least 10 atomic diameters and then increases dramatically in the glass transition region. As stated previously, the normalized real space kernel for the FJC-WCA system upon decreasing the temperatures are very close to each other and, since we are not confident that such a system will actually exhibit a glass transition within the temperature range considered here, we do not display them.

We have shown in the previous section that the form of the fitting function plays an important role on the kernel's shape [Puscasu 2010c]. As temperature decreases, the choice of fitting function has a greater effect on the shape compared to the form of the potential and consequently on the width of the kernel. For instance, kernels obtained from the two-term equal-weighted Gaussian functional forms are slightly distorted in physical space and yield smaller widths. This problem could be easily solved by including more terms in the Gaussian form. However, this

Tab. 5.3. Zero shear viscosities η_0 evaluated using the Gaussian and Lorentzian-type functions.

	T	1.0	0.8	0.6	0.5	0.45	0.4	0.2	0.02
						FENE-LJ			
2-term Gaussian	$N_s = 10$	8.2	8.8	17	53	$0.4 \cdot 10^3$	$0.4 \cdot 10^4$	-	-
	$N_s = 20$	15.7	28.2	43	86	$0.6 \cdot 10^3$	$0.5 \cdot 10^4$	-	-
	$N_s = 50$	42.8	105	150	140	$0.9 \cdot 10^3$	$0.8 \cdot 10^4$	-	-
4-term Gaussian	$N_s = 10$	8.1	9.3	19	78	$0.8 \cdot 10^3$	$0.9 \cdot 10^4$	-	-
	$N_s = 20$	15.3	29.8	48	103	$0.9 \cdot 10^3$	$1.1 \cdot 10^4$	-	-
	$N_s = 50$	42.8	105	150	184	$1.1 \cdot 10^3$	$1.3 \cdot 10^4$	-	-
Lorentzian-type	$N_s = 10$	8.1	9.2	28	70	$0.7 \cdot 10^3$	$0.8 \cdot 10^4$	-	-
	$N_s = 20$	15.5	31.0	55	119	$0.9 \cdot 10^3$	$1.0 \cdot 10^4$	-	-
	$N_s = 50$	42.8	105	150	223	$1.2 \cdot 10^3$	$1.3 \cdot 10^4$	-	-
						FJC-WCA			
2-term Gaussian	$N_s = 10$	8.0	8.9	9.2	-	-	10	15	61
	$N_s = 20$	14.9	16.8	18	-	-	19	28	77
	$N_s = 50$	40.2	42.5	44	-	-	50	59	102
4-term Gaussian	$N_s = 10$	8.1	9.3	10.1	-	-	11	17	65
	$N_s = 20$	15.2	17.0	19	-	-	20	30	80
	$N_s = 50$	41.3	44.5	46	-	-	52	62	124
Lorentzian-type	$N_s = 10$	8.1	9.2	12	-	-	11	18	69
	$N_s = 20$	15.9	17.2	22	-	-	21	30	84
	$N_s = 50$	42.4	45.8	50	-	-	53	63	131

introduces undesired additional fitting parameters with insignificant improvement in the overall shape at temperatures above $T = 0.5$.

For the FENE-LJ chain, the trends with chain length and the dependence of the results upon the choice of functional form for the real space are similar to those at state point $\rho = 0.84$, $T = 1.0$ shown in the previous section. The shape of the kernels varies slightly with the number of sites per chain for the range of chain lengths considered here. Though the Gaussian and Lorentzian-type functional forms predict different shapes of the real space kernel in general and the $\eta(y = 0)$ value in particular, the local effective viscosities, $\eta_0 = \int_{-\infty}^{\infty} \eta(y)dy$, shown in Table 5.3 were in good agreement with the simulated values given in Table 5.1 for the above mentioned state point and for all molecular weights. However, we stress that care must be taken when the Lorentzian-type function is inverse Fourier transformed over a very narrow function as it is very sensitive to the interval, number of points and truncation used in integration.

Additional insight into the relationship between the viscosity kernel and the structure of the fluid can be gained by considering a normalization factor that accounts for the structural properties. Structural properties that we have investigated include the radial distribution functions (RDFs) (or structure factor in reciprocal space) and the structural normalization factor ξ_g calculated from the RDF. If we recall that ξ_g is a measure of the range over which the RDF decays to one it is therefore regarded as a correlation length of the radial distribution function.

Our radial distribution functions presented in Fig. 5.18 are in good agreement with those published previously [Bulacu 2007, Bennemann 1998]. The RDFs for $N_s = 10$ in Fig. 5.18 show sharp peaks due to bonds ($l = 1.0\sigma$) and LJ shells. The second LJ coordination shell is visible in a peak at $r \approx 2\sigma$. ξ_g increases as we lower the temperature, from 0.582 at $T = 1.0$ to 0.836 at $T = 0.4$ for a 10-site molecule and only slightly increases as we enlarge the polymers

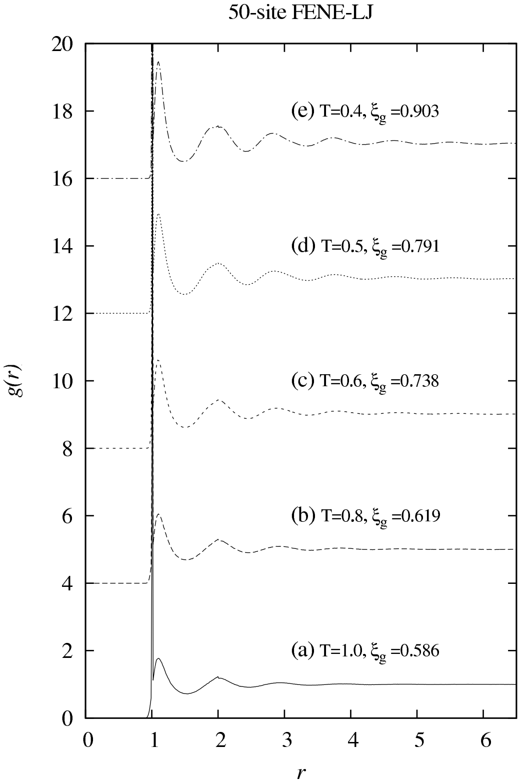

Fig. 5.18. Total intra- and intermolecular radial distribution function $g(r)$ and normalization factors ξ_g, as functions of temperature for a 50-site FENE-LJ chain. For clarity, the RDFs are shifted upwards by 4 units in (b), (c), (d) and (e). A complete set of normalization factors are plotted in Fig. 5.20.

from 10 to 50 sites per molecule as seen in Fig. 5.20(a). The static scaling factor based on the pair distribution function slightly decreases with temperature simply because of the peaks in $g(r)$ which attenuate as we raise the temperature. It is not a complete "structural" representation and must be therefore treated as an attempt to introduce structural normalizations. In addition, we found in our previous chapter that the inter-molecular contribution in $g(r)$ leads to a completely different picture of the static scaling factor. Consequently, a deeper analysis of the structural normalization for different complex fluids is needed.

The real space kernels shown in Figs. 5.17(a) and (b) are normalized with respect to ξ_g and replotted in Figs. 5.19(a) and (b). We can see that despite the fact that the structural normalization procedure has slightly reduced the difference between the real space kernels in the high temperature region $0.6 \leq T \leq 1.0$ and preserved their features, it does not completely remove this difference. This suggests that the width of the kernel does not only depend on the site-site correlations. The normalization factor based on the pair distribution function, which is generally related to liquid structure, must be extended to include correlations such as alignment and

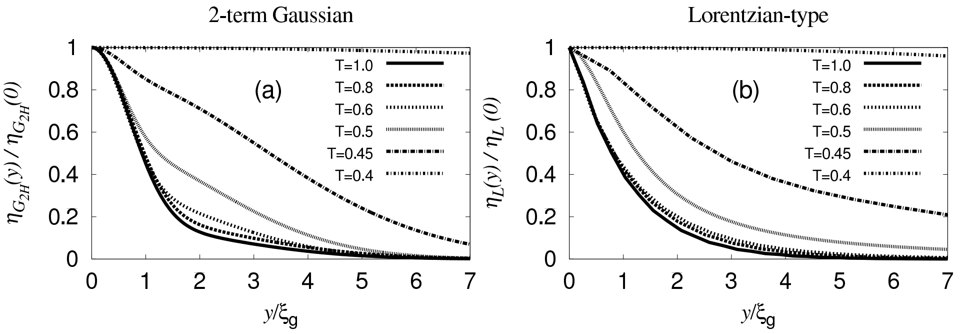

Fig. 5.19. Real space kernel of a 10-site FENE-LJ melt obtained numerically from the Lorentzian-type functional form Eq. (3.2) at different temperatures and normalized by the factor ξ_g.

orientation correlations. Furthermore, as the temperature approaches the glass transition region $T < 0.5$ the normalization must be further generalized in order to suggest a universal kernel function.

Such an approach could be based on the idea of dynamic heterogeneity which states that the dynamics of a glass former is governed by dynamic spatial correlations in contrast to the assumption of homogeneity of mode coupling theories [Hurley 1995]. Therefore a dynamic scaling factor must be employed. Such a scaling factor can be extracted for instance from Eq. (3.2) by non-dimensionalizing k_y by a length we will call ζ.

$$\zeta = \alpha^{1/\beta}. \tag{5.5}$$

The temperature dependence of ζ for different chain lengths is given in Fig. 5.20(b). We can see an exponential increase in the length scales as we approach the glass transition region. This confirms the existence of a dynamic heterogeneity in the system which implies that the increase in time scales as the glass transition is approached is associated with growing length scales of dynamically, not statically, correlated regions of space [Garrahan 2002].

Surprisingly, a qualitative comparison of the temperature dependence of the dynamic scaling factor ζ with the temperature dependence of the coherence length ℓ [Berthier 2004] shows a good agreement. The coherence length ℓ was associated with the ordering of the liquid's dynamics by measuring spatial correlations between individual particle relaxations [Hurley 1995] and calculated from the wavevector dependence of a correlator based on the standard self-intermediate scattering function [Berthier 2004, Whitelam 2005].

A further confirmation of the collective or cooperative dynamics can be seen in Fig. 5.21. The real space viscosity kernels fall onto essentially one curve for the entire range of temperatures. From Fig. 5.21, we can draw the conclusion that the behaviour of the relaxation time changes from the high-temperature to low-temperature behaviour close to the onset of a critical point responsible for the existence of the glass state. Thus, the viscosity of a supercooled liquid increases rapidly as temperature is lowered, because the dynamics becomes increasingly spatially correlated (or nonlocal).

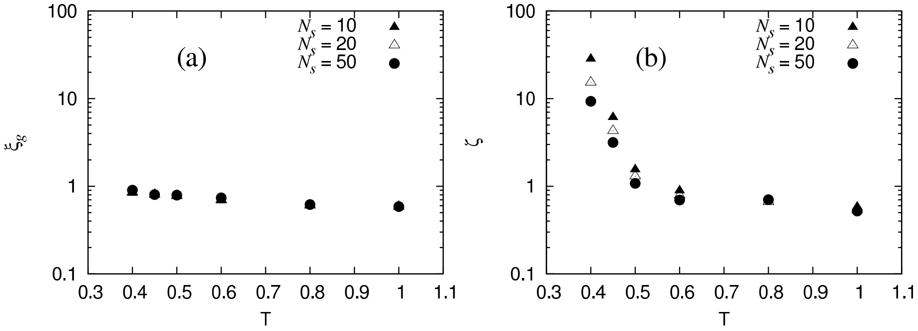

Fig. 5.20. Temperature dependence of the (a) static scaling factor ξ_g, Eq. (3.7), and (b) dynamic scaling factor ζ, Eq. (5.5), for different chain lengths.

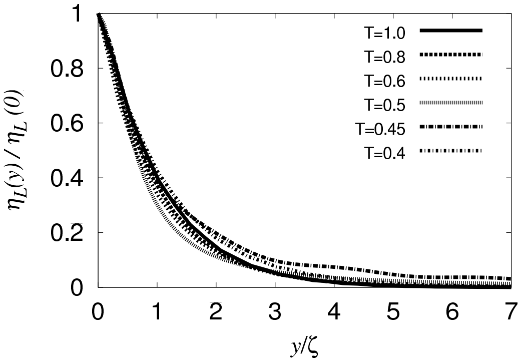

Fig. 5.21. Real space kernel of a 10-site FENE-LJ melt obtained numerically from the Lorentzian-type functional form Eq. (3.2) at different temperatures and normalized by the dynamic factor ζ, Eq. (5.5).

5.6 Summary

The main results can be summarized as follows:

(i) This section has been devoted to the analysis of the nonlocal viscosity kernel of polymeric fluids, when cooled towards their glass transition temperature using equilibrium molecular dynamics simulation. This study confirms the previous results for the self-diffusion coefficient and glass transition temperature and points out the importance of including the attractive part in the potential [Berthier 2009a] in order to achieve a glassy state in which to study the shape of the kernels.

(ii) The values obtained for the self-diffusion coefficients and the glass transition temperatures are in good agreement with those available in the literature. For the FJC-WCA system we observe no glasslike enhancement except at extremely low temperatures of less than 0.01. This value is not evident from the stress ACF.

(iii) The evaluation of the zero wave-vector viscosity involves calculations of the shear stress ACFs in the atomic hydrodynamic representation, as well as their extrapolation in the low temperature regions. The correlation functions and consequently zero wave-vector viscosity follow the expected behaviour when decreasing the temperature and the overall shape of the kernel at low temperatures is primarily affected by the attractive part of the potential. The data near and below the glass transition behave like a delta function in reciprocal space. Otherwise, it is well represented by a Lorentzian-type or two-term Gaussian function.

(iv) In the spatial domain and close to the glass transition temperature, the width of the kernel increases significantly from 4-6 atomic diameters at $T = 1$ to at least 10 atomic diameters at $T = 0.5$ followed by a dramatic increase closer to T_g. It is found that a dynamic scaling factor obtained from the reciprocal space viscosity kernels reduces the real space kernels to a unique form unlike the static scaling factors based on pair distribution functions. This is a further evidence that the slow dynamics in supercooled liquids is governed by a dynamic critical point at which time and length scales diverge [Whitelam 2004].

In conclusion, the response of polymer melts to a velocity gradient near T_g turns out to be highly nonlocal. In systems where the strain rate varies significantly over these distances, the generalized viscosity must be used in order to correctly compute the velocity profile of polymer melts via use of generalized hydrodynamics. This implies that the classical Navier-Stokes hydrodynamics will fail for such systems [Goyon 2008].

In view of the long runs required to obtain reliable data for the transport coefficients via equilibrium time correlation functions, the MD simulations should be extended to cover a much greater time range [Sen 2006, Ramirez 2007b, Ramirez 2007a]. We repeat that our conclusions are based on solid, but necessarily limited in range, numerical evidence. Thus, we leave open the possibility that the zero-wavevector zero-frequency viscosities change when a broader range of time scales is covered. However, we do not believe that our results would be significantly altered by computing correlation functions with longer total delay times except at the very lowest temperatures studied. The trend in the width of the real space viscosity kernel with decreasing temperatue would not significantly change. In future work, it would also be interesting to study polymer melts in the entangled regime [Kremer 1990, Yamamoto 2004, Likhtman 2007, Read 2008].

6 Conclusions

In this paper, we used molecular dynamics simulations to investigate the wave-vector dependent viscosities and their inverse Fourier transforms for simple monatomic fluids and two classes of molecular fluids: alkane (butane) and polymer (FJC and FENE) chains. Generally, the agreement between our results and other equilibrium data in the zero-frequency zero-wavevector limit confirms the validity of our data. The equilibrium molecular dynamics calculation involved the evaluation of the transverse momentum density and shear stress autocorrelation functions. The main results can be summarized as follows:

For monatomic fluids the shape of the normalized viscosity kernel in reciprocal space in the low wavevector region is the same. Though the normalized reciprocal kernels insignificantly decreases with the density they show a similar limiting behaviour at high k_y values. For the LJ potential compared to a WCA potential we find higher viscosities in the low wavevector region but the normalized shape of the kernels are almost identical.

For liquid chlorine, the real space viscosity kernel has a width of roughly 4-6 atomic diameters while for monatomic systems at high densities the width is about 3-5 atomic diameters and 2-4 atomic diameters at low densities.

For molecular systems, an insignificant variation in the shape of both normalized reciprocal space and real space kernels has been noted for the entire range of molecular weights considered here. The real space viscosity kernel of butane has a width of roughly 3-5 atomic diameters while for polymer melts the width is about 4-6 atomic diameters. The viscosity kernels of FENE and FJC chains are essentially the same but much larger chains would also be worth considering in the future in order to cover entangled polymers.

The proposed normalization scaling based on the correlation length of the radial distribution function allowed us to compare the real space kernels of different polymeric melts, however, in the case of butane, only the inter-molecular contributions in the radial distribution function leads to an improved agreement. This suggests a need for a more comprehensive structural normalization of complex molecular structures.

Also, we identified that the choice of functional forms used in the parameterization of the reciprocal space kernels plays a significant role in the prediction of the real space kernel shape. The parameterization reveals that two relatively simple functional forms, namely a sum of Gaussian terms and a Lorentzian-type function, fits the data well over a wide range of wavevectors and state points. The Lorentzian-type function can not be Fourier inverse transformed analytically, therefore an expansion up to a four-term Gaussian (which gives a better accuracy compared to the Lorentzian-type function) can be used in situations when an analytical input into fluid dynamics computations is needed. Even though the parameterization of the reciprocal space kernel has shown that the potential energy function, density and temperature have a great impact on the parameters, the resulting kernels vary only slightly with those temperatures chosen in this work (except for supercooled polymers).

For polymers cooled down towards their glassy state, our study confirms the previous results for the self-diffusion coefficient and glass transition temperature but points out the importance of including the attractive part in the potential in order to achieve a glassy state in which to study the shape of the kernels. While the values obtained for the glass transition temperatures of FENE-LJ and FJC-LJ polymer melts are in good agreement with those available in the literature for the FJC-WCA system we observe no glasslike enhancement except at extremely low temperatures of less than 0.01. At low temperatures the overall shape of the kernel is primarily affected by the attractive part of the potential. The data near and below the glass transition behave like a delta function in reciprocal space. Otherwise, it is well represented by a Lorentzian-type or two-term Gaussian function. In the spatial domain and close to the glass transition temperature, the width of the kernel increases significantly from 4-6 atomic diameters at $T = 1$ to at least 10 atomic diameters at $T = 0.5$ followed by a dramatic increase closer to T_g. It is found that a dynamic scaling factor obtained from the reciprocal space viscosity kernels reduces the real space kernels to a unique form unlike the static scaling factors based on pair distribution functions. This is an evidence that the slow dynamics in supercooled liquids is governed by a dynamic critical point at which time and length scales diverge [Whitelam 2004]. Thus, the response of polymer melts to a velocity gradient near the glass transition temperature turns out to be highly nonlocal.

Overall, in systems where the strain rate varies significantly over the width of the real space kernels, the generalized nonlocal viscosity must be used in order to correctly compute the velocity profile of atomic and molecular fluids via use of generalized hydrodynamics.

In view of the long runs required to obtain reliable data for the transport coefficients via equilibrium time correlation functions, the MD simulations could be extended to cover a much greater time range in particular by using coarse grained models [Ramirez 2007b, Ramirez 2007a]. In future work, it would also be interesting to study polymer melts in the entangled regime and to extend the spatial scaling factor to include alignment and orientation correlations. In order to compute the reciprocal space viscosities in the molecular hydrodynamic representation the extra correlation functions (e.g. due to coupling between the momentum current and the angular velocity at nonzero frequency) must be included in the future.

It might also be of interest to simulate systems in the near-critical region [Fixman 1967]. Many of the near-critical phenomena (e.g. shear thinning) cannot be experimentally observed on Earth due to gravity which stratifies the density so that the layer near the critical density is too thin to be studied in a viscometer [Berg 2008]. The density of fluids near their liquid-vapour critical point is enormously sensitive to gradients of pressure and temperature, therefore simulations have to be carried out at an extremely high resolution. A continuation in this regard would be the simulation of monatomic Lennard-Jones liquids [Smit 1992], alkanes [Smit 1994, Smit 1999] or more complex mixtures [Lisal 1999] and FENE [Ouyang 2008] chains near their critical region.

Finally, this work has been concerned with a few molecular systems, but the methodology can easily be used for larger and more complex molecules with different constraint schemes or nearest-neighbour bond constraints.

Acknowledgements

The author is indebted to Prof. Billy Todd, Prof. Peter Daivis and Dr. Jesper Hansen for their essential advice and support during the doctoral years and beyond. He is also grateful to the referees who reviewed this work in full or in part for their constructive discussions and valuable feedback.

References

[Abgrall 2009] P. Abgrall and N.-T. Nguyen. Nanofluidics. Artech House, Norwood, 2009.

[Alder 1967] B. J. Alder and T. E. Wainwright. *Velocity autocorrelations for hard spheres*. Phys. Rev. Lett., vol. 18, pages 988–990, 1967.

[Allen 1984] M. P. Allen. *Atomic and molecular representations of molecular hydrodynamic variables*. Mol. Phys., vol. 52, pages 705–716, 1984.

[Allen 1989] M. P. Allen and D. J. Tildesley. Computer simulation of liquids. Clarendon Press, New York, 1989.

[Alley 1983a] W. E. Alley and B. J. Alder. *Generalized transport coefficients for hard spheres*. Phys. Rev. A, vol. 27, pages 3158–3173, 1983.

[Alley 1983b] W. E. Alley, B. J. Alder and S. Yip. *The neutron scattering function for hard spheres*. Phys. Rev. A, vol. 27, pages 3174–3186, 1983.

[Baranyai 1990] A. Baranyai and D. J. Evans. *New algorithm for constrained molecular dynamics simulation of liquid benzene and naphthalene*. Mol. Phys., vol. 70, pages 53–63, 1990.

[Bennemann 1998] C. Bennemann, W. Paul, K. Binder and B. Dünweg. *Molecular-dynamics simulation of the thermal glass transition in polymer melts: α-relaxation behaviour*. Phys. Rev. E, vol. 57, page 843, 1998.

[Berg 2008] R. F. Berg, M.R. Moldover, M. Yao and G. Zimmerli. *Shear thinning near the critical point of xenon*. Phys. Rev. E, vol. 77, page 041116, 2008.

[Berthier 2003] L. Berthier and J. P. Garrahan. *Real space origin of temperature crossovers in supercooled liquids*. Phys. Rev. E, vol. 68, page 041201, 2003.

[Berthier 2004] L. Berthier. *Time and length scales in supercooled liquids*. Phys. Rev. E, vol. 69, page 020201, 2004.

[Berthier 2009a] L. Berthier and G. Tarjus. *Nonperturbative effect of attractive forces in viscous liquids*. Phys. Rev. Lett., vol. 103, page 175601, 2009.

[Berthier 2009b] L. Berthier and T. A. Witten. *Compressing nearly hard spheres fluids increases glass fragility*. EPL, vol. 86, page 10001, 2009.

[Berthier 2009c] L. Berthier and T. A. Witten. *Glass transition of dense fluid of hard and compressible spheres*. Phys. Rev. E, vol. 80, page 021502, 2009.

[Berthier 2010] L. Berthier. http://w3.lcvn.univ-montp2.fr/ berthier, 2010.

[Bertolini 1995] D. Bertolini and A. Tani. *Stress tensor and viscosity of water: Molecular dynamics and generalized hydrodynamics results*. Phys. Rev. E, vol. 52, page 1699, 1995.

[Bhatia 2008] S. K. Bhatia and D. Nicholson. *Modeling Mixture Transport in Nanopores: Departure from Existing Paradigms*. Phys. Rev. Lett., vol. 100, page 236103, 2008.

[Binder 1986] K. Binder and A. P. Young. *Spin glasses: experimental facts, theoretical concepts, and open questions*. Rev. Mod. Phys., vol. 58, pages 801–976, 1986.

[Binder 1995] K. Binder. Monte carlo and molecular dynamics simulations in polymer science. Oxford University Press, New York, 1995.

[Binder 1999] K. Binder, C. Bennemann, J. Baschnagel and W. Paul. *Anomalous diffusion of polymers in supercooled melts near the glass transition*. In R. Kutner, A. Pekalski and K. Sznajd-Weron, editeurs, Anomalous Diffusion: From basics to Applications, pages 124–139. Springer, Berlin, 1999.

[Binder 2003] K. Binder, J. Baschnagel and W. Paul. *Glass transition of polymer melts: test of theoretical concepts by computer simulation*. Prog. Polym. Sci., vol. 28, pages 115–172, 2003.

[Binder 2010] K. Binder. *Condensed Matter Theory Group, Johannes Gutenberg University Mainz.* http://www.cond-mat.physik.uni-mainz.de, 2010.

[Bishop 1979] M. Bishop, M.H. Kalos and H.L. Frish. *Molecular dynamics of polymeric systems.* J. Chem. Phys, vol. 70, no. 3, pages 1299–1304, 1979.

[Bitsanis 1988] I. Bitsanis, T. K. Vanderlick, M. Tirrell and H. T. Davis. *Tractable molecular theory of flow in strongly inhomogeneous fluids.* J. Chem. Phys., vol. 89, pages 3152–3162, 1988.

[Bitsanis 1990] I. Bitsanis, S. A. Somers, H.T. Davis and M. Tirrell. *Microscopic dynamics of flow in molecularly narrow pores.* J. Chem. Phys., vol. 93, pages 3427–3431, 1990.

[Boon 1980] J. P. Boon and S. Yip. Molecular hydrodynamics. McGraw-Hill, New York, 1980.

[Bosko 2004a] J. T. Bosko, B. D. Todd and R. J. Sadus. *Internal structure of dendrimers in the melt under shear: A molecular dynamics study.* J. Chem. Phys., vol. 121, no. 2, pages 1091–1096, 2004.

[Bosko 2004b] J. T. Bosko, B. D. Todd and R. J. Sadus. *Viscoelastic properties of dendrimers in the melt from nonequilibrium molecular dynamics.* J. Chem. Phys., vol. 121, no. 23, pages 12050–12059, 2004.

[Bosko 2005] J. T. Bosko, B. D. Todd and R. J. Sadus. *Molecular simulation of dendrimers and their mixtures under shear: Comparison of isothermal-isobaric (NpT) and isothermal-isochoric (NVT) ensemble systems.* J. Chem. Phys., vol. 123, page 034905, 2005.

[Brown 1995] D. Brown and S. Neyertz. *A general pressure tensor calculation for molecular dynamics simulations.* Mol. Phys., vol. 84, pages 577–595, 1995.

[Bruus 2008] H. Bruus. Theoretical microfluidics. Oxford University Press, 2008.

[Bulacu 2005] M. Bulacu and E. Van der Giessen. *Effect of bending and torsion rigidity on self-diffusion in polymer melts: A molecular-dynamics study.* J. Chem. Phys., vol. 123, no. 11, page 114901, 2005.

[Bulacu 2007] M. Bulacu and E. Van der Giessen. *Molecular-dynamics simulation study of the glass transition in amorphous polymers with controlled chain stiffness.* Phys. Rev. E, vol. 76, page 011807, 2007.

[Bulacu 2008] Monica Bulacu. *Molecular Dynamics Study of Entangled Polymer Chains.* PhD thesis, University of Groningen, 2008.

[Cadusch 2008] P. J. Cadusch, B. D. Todd, J. Zhang and P. J. Daivis. *A non-local hydrodynamic model for the shear viscosity of confined fluids: analysis of homogeneous kernel.* J. Phys. A, vol. 41, page 035501, 2008.

[Car 1985] R. Car and M. Parrinello. *Unified approach for molecular dynamics and density-functional theory.* Phys. Rev. Lett., vol. 55, no. 22, pages 2471–2474, 1985.

[Chynoweth 1991] S. Chynoweth, U. C. Klomp and Y. Michopoulos. *Comment on: Rheology of n-alkanes by nonequilibrium molecular dynamics.* J. Chem. Phys., vol. 95, page 3024, 1991.

[Cicotti 1986] G. Cicotti and W. G. Hoover. Molecular dynamics simulations of statistical mechanical systems. North Holland, Amsterdam, 1986.

[Cieplak 2001] M. Cieplak, J. Koplik and J. R. Banavar. *Boundary conditions at a fluid-solid interface.* Phys. Rev. Lett., vol. 86, pages 803–806, 2001.

[Cramer 2002] C. J. Cramer. Essentials of computational chemistry. John Wiley & Sons, New York, 2002.

[Daivis 1992] P. J. Daivis, D. J. Evans and G. P. Morriss. *Computer simulation study of the comparative rheology of branched and linear alkanes.* J. Chem. Phys., vol. 97, page 616, 1992.

[Daivis 1994] P. J. Daivis and D. J. Evans. *Comparison of constant pressure and constant volume nonequilibrium simulations of sheared model decane.* J. Chem. Phys., vol. 100, pages 541–547, 1994.

[Daivis 1995] P. J. Daivis and D. J. Evans. *Tranasport coefficients of liquid butane near the boiling point by equilibrium molecular dynamics.* J. Chem. Phys., vol. 103, page 4261, 1995.

[Daivis 2003] P. J. Daivis, M. L. Matin and B. D. Todd. *Nonlinear shear and elongational rheology of model polymer melts by nonequilibrium molecular dynamics*. J. Non-Newtonian Fluid Mech., vol. 111, pages 1–18, 2003.

[Daivis 2004] P. J. Daivis and D. J. Evans. *A comparison of methods used to calculate the wavevector and frequency dependent viscosity*. unpublished, 2004.

[Daivis 2007] P. J. Daivis, M. L. Matin and B. D. Todd. *Nonlinear shear and elongational rheology of model polymer melts at low strain rates*. J. Non-Newtonian Fluid Mech., vol. 147, pages 35–44, 2007.

[de Gennes 1979] P. G. de Gennes. Scaling concepts in polymer physics. Cornell University Press, Ithaca, NY, 1979.

[Dhont 1999] Jan K. G. Dhont. *A constitutive relation describing the shear-banding transition*. Phys. Rev. E, vol. 60, no. 4, pages 4534–4544, 1999.

[Doi 1986] M. Doi and S. F. Edwards. The theory of polymer dynamics. Oxford Science Publications, Oxford, 1986.

[Doi 1996] M. Doi. Introduction to polymer physics. Clarendon Press, Oxford, 1996.

[Ebewele 2000] R. O. Ebewele. Polymer science and technology. CRC Press, New York, 2000.

[Edberg 1986] R. Edberg, D. J. Evans and G. P. Morriss. *Constrained molecular dynamics: Simulations of liquid alkanes with new algorithm*. J. Chem. Phys, vol. 84, page 6933, 1986.

[Edberg 1987a] R. Edberg, D. J. Evans and G. P. Morriss. *On the nonlinear Born effect*. Mol. Phys., vol. 62, no. 6, pages 1357–1369, 1987.

[Edberg 1987b] R. Edberg, G. P. Morriss and D. J. Evans. *Rheology of n-alkanes by nonequilibrium molecular dynamics*. J. Chem. Phys, vol. 86(8), pages 4555–4570, 1987.

[Edel 2009] J. B. Edel and A. J. deMello. Nanofluidics: Nanoscience and nanotechnology. The Royal Society of Chemistry, London, 2009.

[Eijkel 2005] J. C. T. Eijkel and A. van den Berg. *Nanofluidics: what is it and what can we expect from it?* Microfluidics Nanofluidics, vol. 1, page 249, 2005.

[Evans 1976] D. J. Evans. *On the generalized hydrodynamics of polyatomic fluids*. Mol. Phys., vol. 32, pages 1171–1176, 1976.

[Evans 1980] D. J. Evans. *Enhanced t-3/2 Long time tail for the stress-stress time correlation function*. J. Stat. Phys., vol. 22, pages 81–90, 1980.

[Evans 1981a] D. J. Evans. *Equilibrium fluctuation expression for the wave-vector- and frequency-dependent shear viscosity*. Phys. Rev. A., vol. 23, pages 2622–2626, 1981.

[Evans 1981b] D. J. Evans. *Rheological properties of simple fluids by computer simulation*. Phys. Rev. A., vol. 23, pages 1988–1997, 1981.

[Evans 1983] D. J. Evans. *Erratum: Fluctuation expressions for the wave-vector- and frequency-dependent shear viscosity*. Phys. Rev. A., vol. 27, page 1207, 1983.

[Evans 1987] K. E. Evans. *A scaling analysis of the fracture mechanisms in glassy polymers*. J. Polym. Sci., Part B: Polym. Phys., vol. 25, pages 353–368, 1987.

[Evans 1990] D. J. Evans and G. P. Morriss. Statistical mechanics of nonequilibrium liquids. Academic Press, London, 1990.

[Faller 2001] R. Faller and F. Müller-Plathe. *Chain stiffness intensifies the reptation characteristics of polymer dynamics in the melt*. ChemPhysChem, vol. 2, no. 3, pages 180–184, 2001.

[Ferry 1980] J. D. Ferry. Viscoelastic properties of polymer melts. Wiley, New York, 1980.

[Fixman 1967] M. Fixman. *Transport coefficients in the gas critical region*. J. Chem. Phys, vol. 47, no. 8, pages 2808–2818, 1967.

[Flory 1969] P. J. Flory. Statistical mechanics of chain molecules. Interscience Publishers, New York, 1969.

[Freund 1982] M. Freund and G. Mozes. Paraffin products: properties, technologies, applications. Elsevier, New York, 1982.

[Furukawa 2009] A. Furukawa and H. Tanaka. *Nonlocal Nature of the Viscous Transport in Supercooled Liquids: Complex Fluid Approach to Supercooled Liquids*. Phys. Rev. Lett., vol. 103, page 135703, 2009.

[Garrahan 2002] J. P. Garrahan and D. Chandler. *Geometrical explanation and scaling of dynamical heterogeneities in glass forming systems*. Phys. Rev. Lett., vol. 89, page 035704, 2002.

[Gear 1966] C. W. Gear. The numerical integration of ordinary differential equations of various orders. Argonne National Laboratory, Englewood Cliffs, 1966.

[Gear 1971] C. W. Gear. Numerical initial value problems in ordinary differential equations. Prentice Hall, London, 1971.

[Gibbs 1955] J. H. Gibbs and E. A. DiMarzio. *Nature of the glass transition and the glassy state*. J. Chem. Phys, vol. 28, page 373, 1955.

[Gibbs 1958] J. H. Gibbs and E. A. DiMarzio. *Chain stiffness and the lattice theory of polymer phases*. J. Chem. Phys, vol. 28, page 807, 1958.

[Goff 208] C. L. Goff and P. Ben-Abdallah. *Enhanced thermal conductivity in nanofluids under the action of oscillating force fields*. J. Nanopart. Res., vol. 10, pages 1115–1120, 208.

[Golub 1996] G. H. Golub and C. F. Van Loan. Matrix computations. Johns Hopkins, Baltimore, 1996.

[Gordon 2006] P. A. Gordon. *Development of intermolecular potentials for predicting transport properties of hydrocarbons*. J. Chem. Phys., vol. 125, page 014504, 2006.

[Götze 1992] W. Götze and Sjögren. *Relaxation processes in supercooled liquids*. Rep. Progr. Phys., vol. 55, page 241, 1992.

[Goyon 2008] J. Goyon, A. Colin, G. Ovarlez, A. Ajdari and L. Bocquet. *Spatial cooperativity in soft glassy flows*. Nature, vol. 454, page 84, 2008.

[Grest 1981] G. S. Grest and M. Cohen. *Liquids, glasses and the glass transition: a free volume approach*. In S. A. Rice I. Prigogine, editeur, Advances in Chemical Physics, volume 48, pages 455–525. Wiley, New York, 1981.

[Haile 1983] J. M. Haile and S. Gupta. *Extensions of the molecular dynamics simulation method. II. Isothermal systems*. J. Chem. Phys, vol. 79, pages 3067–3076, 1983.

[Hansen 1986] J. P. Hansen and I. R. McDonald. Theory of simple liquids. Academic Press, London, 1986.

[Hansen 2007] J. S. Hansen, P. J. Daivis, , K. P. Travis and B. D. Todd. *Parameterization of the nonlocal viscosity kernel for an atomic fluid*. Phys. Rev. E, vol. 76, page 041121, 2007.

[Hansen 2010] J. S. Hansen, B. D. Todd and P. J. Daivis. *Prediction of fluid velocity slip at solid surfaces*. vol. In preparation, 2010.

[Harrowell 1993] P. Harrowell. *Visualizing the collective motions responsible for the α and β relaxations in a model glass*. Phys. Rev. E, vol. 48, pages 4359–4363, 1993.

[Harrowell 2010] P. Harrowell. *School of Chemistry, University of Sydney*. http://www.chem.usyd.edu.au/research/harrowell.html, 2010.

[Holian 1980] B. L. Holian, W. G. Hoover, B. Moran and G. K. Straub. *Shock-wave structure via nonequilibrium molecular dynamics and Navier-Stokes continuum mechanics*. Phys. Rev. A, vol. 22, no. 6, pages 2798–2808, 1980.

[Holian 1998] L. Holian and P. S. Lomdahl. *Plasticity induced by shock waves in nonequilibrium molecular-dynamics simulations.* Science, vol. 280, page 2085, 1998.

[Hounkonnou 1992] M. N. Hounkonnou, C. Pierleoni and J. P. Ryckaert. *Liquid chlorine in shear and elongational flows: A nonequillibrium molecular dynamics study*. J. Chem. Phys., vol. 97, no. 3, pages 9335–9343, 1992.

[Hunt 2009a] T. A. Hunt and B. D. Todd. *A comparison of model linear chain molecules with constrained and flexible bond lengths under Couette and extensional flows*. Mol. Simul., vol. 35, pages 1153–1167, 2009.

[Hunt 2009b] T. A. Hunt and B. D. Todd. *Diffusion of linear polymer melts in shear and extensional flows*. J. Chem. Phys., vol. 131, page 054904, 2009.

[Hurley 1995] M. M. Hurley and P. Harrowell. *Kinetic structure of a two-dimensional liquid*. Phys. Rev. E, vol. 52, pages 1694–1698, 1995.

[Hurley 1996] M. M. Hurley and P. Harrowell. *Non-Gaussian behavior and the dynamical complexity of particle motion in a dense two-dimensional liquid*. J. Chem. Phys., vol. 105, page 10521, 1996.

[Irving 1950] J. H. Irving and J. G. Kirkwood. *The Statistical Mechanical Theory of Transport Processes. IV. The Equations of Hydrodynamics*. J. Chem. Phys., vol. 18, pages 817–829, 1950.

[Isobe 2009] M. Isobe and B. J. Alder. *Molasses tail in two dimensions*. Mol. Phys., vol. 107, pages 609–613, 2009.

[IUPAC 2010] IUPAC. *International Union of Pure and Applied Chemistry*. http://www.iupac.org, 2010.

[Jensen 2007] Frank Jensen. Introduction to computational chemistry. John Wiley & Sons, New York, 2007.

[Johnson 1994] J. K. Johnson, E. A. Müler and K. E. Gubbins. *Equation of state for Lennard-Jones chains*. J. Phys. Chem., vol. 98, pages 6413–6419, 1994.

[Keblinski 2005] P. Keblinski, J. A. Eastman and D. G. Cahill. *Nanofluid for thermal transport*. Matter Today, vol. 8, pages 36–44, 2005.

[Kenna 1986] G. B. Mc Kenna. *Glassformation and glassy behaviour*. In C. Booth and C. Proce, editeurs, Comprehensive Polymer Science, volume 2, pages 311–362. Pergamont Press, Oxford, 1986.

[Kim 2005] J. Kim and T. Keyes. *On the Breakdown of the Stokes-Einstein Law in Supercooled Liquids*. J. Phys. Chem., vol. 109, no. 45, pages 21445–21448, 2005.

[Kremer 1990] K. Kremer and G. S. Grest. *Dynamics of entangled linear polymer melts: A molecular-dynamics simulation*. J. Chem. Phys., vol. 92, no. 8, pages 5057–5086, 1990.

[Kremer 2003] K. Kremer. *Computer simulations for macromolecular science*. Macromol. Chem. Phys., vol. 204, pages 257–264, 2003.

[Kröger 1993] M. Kröger, W. Loose and S. Hess. *Rheology and structural changes of polymer melts via nonequilibrium molecular dynamics*. J. Rheol., vol. 37, pages 1057–1079, 1993.

[Kröger 1997] M. Kröger, C. Luap and R. Müller. *Polymer melts under uniaxial elongational ow: Stress-ical behaviour from experimental and nonequilibrium molecular dynamics computer simulations*. Macromol., vol. 30, no. 3, pages 526–539, 1997.

[Kröger 2000] M. Kröger and S. Hess. *Rheological evidence for a dynamical crossover in polymer melts via nonequilibrium molecular dynamics*. Phys. Rev. Lett., vol. 85, no. 5, pages 1128–1131, 2000.

[Leutheusser 1982a] E. Leutheusser. *Dynamics of a classical hard-spheres gas I. Formal theory*. J. Phys. C, vol. 15, page 2801, 1982.

[Leutheusser 1982b] E. Leutheusser. *Dynamics of a classical hard-spheres gas. II. Numerical results*. J. Phys. C, vol. 15, page 2827, 1982.

[Levesque 1973] D. Levesque, L. Verlet and J. Kurkijarvi. *Computer experiments on classical fluids. IV. Transport properties and time-correlation functions of the Lennard-Jones liquid near its triple point*. Phys. Rev. A, vol. 7, pages 1690–1700, 1973.

[Levesque 1987] D. Levesque and L. Verlet. *Molecular dynamics calculations of transport coefficients*. Mol. Phys., vol. 61, pages 143–159, 1987.

[Likhtman 2007] A. E. Likhtman, S. K. Sukumaran and J. Ramirez. *Linear viscoelasticity from molecular dynamics simulation of entangled polymers*. Macromol., vol. 40, pages 6748–6757, 2007.

[Lisal 1999] M. Lisal, W. R. Smith and I. Nezbeda. *Accurate computer simulation of phase equilibrium for complex mixtures. Application to binaries involving isobutane, methanol, methyl tert-butyl ether, and n-butane*. J. Phys. Chem. B, vol. 103, no. 47, pages 10496–10505, 1999.

[Luo 1991] H. Luo and C. Hoheisel. *Behaviour of collective time correlation functions in liquids composed of polyatomic molecules*. J. Chem. Phys., vol. 94, no. 12, pages 8378–8383, 1991.

[Luo 1992a] H. Luo and C. Hoheisel. *Computation of transport coefficients of liquid benzene and cyclohexane using rigid multicenter pair interaction models*. J. Chem. Phys., vol. 96, no. 4, pages 3173–3176, 1992.

[Luo 1992b] H. Luo and C. Hoheisel. *Thermodynamics and transport properties of n-butane computed by molecular dynamics using a rigid interaction model*. J. Chem. Phys., vol. 47, no. 6, pages 3956–3961, 1992.

[Martin 1998] M. G. Martin and J. I. Siepmann. *Transferable potentials for phase equilibria. 1. United-atom description of n-alkanes*. J. Phys. Chem. B, vol. 102, pages 2569–2577, 1998.

[Masselon 2008] C. Masselon, J.-B. Salmon and A. Colin. *Nonlocal Effects in Flows of Wormlike Micellar Solutions*. Phys. Rev. Lett., vol. 100, page 038301, 2008.

[Matin 2000] M. L. Matin, P. J. Daivis and B. D. Todd. *Comparison of planar shear flow and planar elongational flow for systems of small molecules*. J. Chem. Phys., vol. 113, no. 20, pages 9122–9131, 2000.

[Matin 2001] M. L. Matin, P. J. Daivis and B. D. Todd. *Erratum: Comparison of planar shear flow and planar elongational flow for systems of small molecules*. J. Chem. Phys., vol. 115, no. 11, page 5338, 2001.

[Matin 2003] M. L. Matin, P. J. Daivis and B. D. Todd. *Cell neighbour list method for planar elongational flow: rheology of a diatomic fluid*. Comput. Phys. Commun., vol. 151, pages 35–46, 2003.

[McCormick 2005] J. A. McCormick, C. K. Hall and S. A. Khan. *The dynamics of single chains within a model polymer melt*. J. Chem. Phys., vol. 122, page 114902, 2005.

[Morriss 1991] G. P. Morriss and D. J. Evans. *A constraint algorithm for the computer simulation of complex molecular liquids*. Comput. Phys. Commun., vol. 62, pages 267–278, 1991.

[Mountain 1994] R. D. Mountain. *Length scales for fragile glass-forming liquids*. J. Chem. Phys., vol. 102, no. 13, pages 5408–5410, 1994.

[Olah 2003] G. A. Olah and A. Molnar. Hydrocarbon chemistry. John Wiley & Sons, New Jersey, 2003.

[Olmsted 1976a] R. D. Olmsted and R. F. Snider. *Difference in fluid dynamics associated with an atomic versus a molecular description of the same system*. J. Chem. Phys., vol. 65, page 3407, 1976.

[Olmsted 1976b] R. D. Olmsted and R. F. Snider. *Symmetry of the pressure tensor in molecular fluids*. J. Chem. Phys., vol. 65, page 3423, 1976.

[Omelyan 2005] I. P. Omelyan, I. M. Mryglod and M. V. Tokarchuk. *Wavevector- and frequency-dependent shear viscosity of water: the modified collective mode approach and molecular dynamics calculations*. Condensed Matter Physics, vol. 8, no. 1(41), pages 25–46, 2005.

[Onsager 1931a] L. Onsager. *Reciprocal relations in irreversible processes. I.* Phys. Rev., vol. 37, page 405, 1931.

[Onsager 1931b] L. Onsager. *Reciprocal relations in irreversible processes. II.* Phys. Rev., vol. 38, pages 2265–2279, 1931.

[Ouyang 2008] W.-Z. Ouyang, Z.-Y. Lu, Z.-Y. Sun and L.-J. An. *Molecular dynamics study on the phase diagrams of linear and branched chain molecules*. Chem. Phys., vol. 344, pages 52–60, 2008.

[Padding 2002] J. T. Padding and W. J. Briels. *Time and length scales of polymer melts studied by coarse-grained molecular dynamics simulations*. J. Chem. Phys, vol. 117, no. 2, pages 925–943, 2002.

[Palmer 1994] B. J. Palmer. *Transverse-current autocorrelation-function calculations of the shear viscosity for molecular liquids*. Phys. Rev. E, vol. 49, pages 359–366, 1994.

[Papoulis 1962] A. Papoulis. The fourier integral and its applications. McCraw-Hill, New York, 1962.

[Peck 2008] R. Peck, C. Olsen and J. Devore. Introduction to statistics and data analysis. BrooksCole, Belmont, 3 édition, 2008.

[Perera 1996] D. N. Perera and P. Harrowell. *Consequences of kinetic inhomogeneities in glasses*. Phys. Rev. E, vol. 54, pages 1652–1662, 1996.

[Petravic 2007] J. Petravic and P. Harrowell. *On the equilibrium calculation of the friction coefficient for liquid slip against a wall*. J. Chem. Phys., vol. 127, page 174706, 2007.

[Puscasu 2010a] R. M. Puscasu, B. D. Todd, P. J. Daivis and J. S. Hansen. *The dynamics of non-local viscosity kernel of polymer melts toward their glassy state*. J. Chem. Phys., vol. 133, page 144907, 2010.

[Puscasu 2010b] R. M. Puscasu, B. D. Todd, P. J. Daivis and J. S. Hansen. *An extended analysis of the viscosity kernel for monatomic and diatomic fluids*. J. Phys.: Condens. Matter, vol. 22, page 195105, 2010.

[Puscasu 2010c] R. M. Puscasu, B. D. Todd, P. J. Daivis and J. S. Hansen. *Non-local viscosity kernel of molecular fluids: butane and polymer melts*. Phys. Rev. E, vol. 82, page 011801, 2010.

[Rahman 1964] A. Rahman. *Correlations in the motion of atoms in liquid argon*. Phys. Rev. A, vol. 136, page 405, 1964.

[Ramirez 2007a] J. Ramirez, S. K. Sukumaran and A. E. Likhtman. *Hierarchical modeling of entangled polymers*. Macromol. Symp., vol. 252, pages 119–129, 2007.

[Ramirez 2007b] J. Ramirez, S. K. Sukumaran and A. E. Likhtman. *Significance of cross correlations in the stress relaxation of polymer melts*. J. Chem. Phys., vol. 126, page 244904, 2007.

[Rapaport 1979] D. C. Rapaport. *Molecular dynamics study of a polymer chain in solution*. J. Chem. Phys., vol. 71, no. 8, pages 3299–3303, 1979.

[Rapaport 1995] D. C. Rapaport. The art of molecular dynamics simulation. Cambridge University Press, Cambridge, 1995.

[Read 2008] D. J. Read, K. Jagannathan and A. E. Likhtman. *Entangled polymers: constraint release, mean paths, and tube bending energy*. Macromol., vol. 41, pages 6843–6853, 2008.

[Reed 2003] Evan J. Reed, Laurence E. Fried and J. D. Joannopoulos. *A Method for Tractable Dynamical Studies of Single and Double Shock Compression*. Phys. Rev. Lett., vol. 90, no. 23, page 235503, Jun 2003.

[Reed 2006] E. J. Reed, L. E. Fried, W. D. Henshaw and C. M. Tarver. *Analysis of simulation technique for steady shock waves in materials with analytical equations of state*. Phys. Rev. E, vol. 74, page 056706, 2006.

[Rigby 1987] D. Rigby and R. J. Roe. *Molecular dynamics simulations of polymer liquid and glass. I. glass transition*. J. Chem. Phys., vol. 87, pages 7285–7292, 1987.

[Roe 1994] R. J. Roe. *Short time dynamics of polymer liquids and glass studied by molecular dynamics*. J. Chem. Phys., vol. 100, no. 2, pages 1610–1619, 1994.

[Rosche 2000] M. Rosche, R. G. Winkler, P. Reineker and M. Schulz. *Topologically induced glass transition in dense polymer systems*. J. Chem. Phys., vol. 112, no. 6, pages 3051–3062, 2000.

[Rouse 1953] P. E. Rouse. *A theory of linear viscoelastic properties of dilute solutions of coiling polymers*. J. Chem. Phys., vol. 21, no. 7, pages 1272–1280, 1953.

[Ryckaert 1975] J. P. Ryckaert and A. Bellemans. *Molecular dynamics of liquid n-butane near its boiling point*. Chem. Phys. Lett., vol. 30, page 123, 1975.

[Ryckaert 1978] J. P. Ryckaert and A. Bellemans. *Molecular dynamics of liquid alkanes*. Discuss. Faraday Soc., vol. 66, page 95, 1978.

[Sadus 1999] Richard J. Sadus. Molecular simulation of fluids: Theory, algorithms and object orientation. Elsevier, Amsterdam, 1999.

[Schiek 1995] R. L. Schiek and E. S. G. Shaqfeh. *A nonlocal theory for stress in bound, Brownian suspensions of slender rigid fibers*. J. Fluid. Mech., vol. 296, page 271, 1995.

[Sen 2006] S. Sen, S.K. Kumar and P. Keblinski. *Analysis of uncertainties in polymer viscoelastic properties obtained from equilibrium computer simulations*. J. Chem. Phys., vol. 124, page 144909, 2006.

[Smit 1992] B. Smit. *Phase diagrams of Lennard-Jones fluids*. J. Chem. Phys., vol. 96, no. 11, pages 8639–8640, 1992.

[Smit 1994] B. Smit, S. Karaborni and J. I. Siepmann. *Computer simulations of vapour-liquid phase equilibria of n-alkanes*. J. Chem. Phys., vol. 102, no. 5, pages 2126–2139, 1994.

[Smit 1999] B. Smit, S. Karaborni and J. I. Siepmann. *Transferable potentials for phase equilibria. 3. Explicit-hydrogen description of normal alkanes*. J. Phys. Chem. B, vol. 103, no. 25, pages 5370–5379, 1999.

[Smith 1996] S. W. Smith, C. K. Hall and B. D. Freeman. *Molecular dynamics study of entangled hard-chain fluids*. J. Chem. Phys., vol. 104, no. 14, pages 5616–5637, 1996.

[Sokhan 2008] V. P. Sokhan and N. Quirke. *Slip coefficient in nanoscale pore flow*. Phys. Rev. E, vol. 78, page 015301(R), 2008.

[Tabeling 2005] P. Tabeling. Introduction to microfluidics. Oxford University Press, New York, 2005.

[Takeuchi 1991] H. Takeuchi and R. J. Roe. *Molecular dynamics simulation of local chain motion in bulk amorphous polymers. II dynamics at glass transition*. J. Chem. Phys., vol. 94, no. 11, pages 7458–7465, 1991.

[Tegenfeldt 2004] J. O. Tegenfeldt, C. Prinz, H. Cao, R. L. Huang, R. H. Austin, S. Y. Chou, E. C. Cox and J. C. Sturm. *Micro- and nanofluidics for DNA analysis*. Anal. Bional. Chem., vol. 378, pages 1678–1692, 2004.

[Thompson 1997] P. A. Thompson and S. M. Troian. *A general boundary condition for liquid flow at solid surfaces*. Nature, vol. 389, page 360, 1997.

[Todd 2007] B. D. Todd and P. J. Daivis. *Homogeneous non-equilibrium molecular dynamics simulations of viscous flow: techniques and applications*. Mol. Sim., vol. 33, page 189, 2007.

[Todd 2008a] B. D. Todd and J. S. Hansen. *Nonlocal viscous transport and the effect on fluid stress*. Phys. Rev. E, vol. 78, page 051202, 2008.

[Todd 2008b] B. D. Todd, J. S. Hansen and P.J. Daivis. *Nonlocal shear stress for homogeneous fluids*. Phys. Rev. Lett., vol. 100, page 195901, 2008.

[Toxvaerd 1990] S. Toxvaerd. *Molecular dynamics calculation of the equation of state of alkanes*. J. Chem. Phys., vol. 93, page 4290, 1990.

[Travis 1995a] K. P. Travis, P. J. Daivis and D. J. Evans. *Thermostats for molecular fluids undergoing shear flow: Application to liquid chlorine*. J. Chem. Phys., vol. 103, no. 24, pages 10638–10651, 1995.

[Travis 1995b] K.P. Travis, P.J. Daivis and D.J. Evans. *Computer simulation algorithms for molecules undergoing planar Couette flow: A nonequilibrium molecular dynamics study*. J. Chem. Phys., vol. 103, no. 3, pages 1109–1118, 1995.

[Travis 1997] K. P. Travis, B. D. Todd and D. J. Evans. *Departure from Navier-Stokes hydrodynamics in confined liquids*. Phys. Rev. E, vol. 55, no. 4, page 4288, 1997.

[Varnik 2002] F. Varnik and K. Binder. *Shear viscosity of a supercooled polymer melt via nonequilibrium molecular dynamics simulation*. J. Chem. Phys., vol. 117, pages 6336–6349, 2002.

[Wallace 2004] M. L. Wallace, B. Joos and M. Plischke. *Rigidity transition in polymer melts with van der Waals interaction*. Phys. Rev. E, vol. 70, page 041501, 2004.

[Wang 2002] J.-C. Wang and K. A. Fichthorn. *Molecular dynamics studies of the effects of chain branching on the properties of confined alkanes*. J. Chem. Phys., vol. 116, no. 1, pages 410–417, 2002.

[Wang 2008a] X. Q. Wang and A. S. Mujumdar. *A review on nanofluids - Part I: theoretical and numerical investigations*. Brazilian Journal of Chemical Engineering, vol. 25, pages 613–630, 2008.

[Wang 2008b] X. Q. Wang and A. S. Mujumdar. *A review on nanofluids - Part II: experiments and applications*. Brazilian Journal of Chemical Engineering, vol. 25, pages 631–648, 2008.

[Weeks 1971] J. D. Weeks, D. Chandler and H. C. Andersen. *Role of Repulsive Forces in Determining the Equilibrium Structure of Simple Liquids*. J. Chem. Phys., vol. 54, pages 5237–5247, 1971.

[Whitelam 2004] S. Whitelam, L. Berthier and J. Garrahan. *Dynamic criticality in glass-forming liquids*. Phys. Rev. Lett., vol. 92, no. 18, page 185705, 2004.

[Whitelam 2005] S. Whitelam, L. Berthier and J. Garrahan. Phys. Rev. E, vol. 71, page 026128, 2005.

[Widmer-Cooper 2008] A. Widmer-Cooper, H. Perry, P. Harrowell and D. R. Reichman. *Irreversible reorganization in a supercooled liquid originates from localized soft modes*. Nature Physics, vol. 4, no. 9, pages 711–715, 2008.

[Widmer-Cooper 2009] A. Widmer-Cooper, H. Perry, P. Harrowell and D. R. Reichman. *Localized soft modes and the supercooled liquids irreversible passage through its configuration space*. J. Chem. Phys., vol. 131, no. 19, page 194508, 2009.

[Williams 1955] M. L. Williams, R. F. Landell and J. A. Ferry. *The temperature dependence of relaxation mechanisms in amorphous polymers and other glass-forming liquids*. J. Am Chem. Soc., vol. 77, page 3701, 1955.

[Yamamoto 2002] R. Yamamoto and A. Onuki. *Dynamics and rheology of a supercooled polymer melt in shear flow*. J. Chem. Phys, vol. 117, pages 2359–2367, 2002.

[Yamamoto 2004] R. Yamamoto and A. Onuki. *Entanglements in quiescent and sheared polymer melts*. Phys. Rev. E, vol. 70, page 041801, 2004.

[Yip 1982] S. Yip, W.E. Alley and B.J. Alder. *Evaluation of time correlation functions from a generalized Enskog equation*. J. Stat. Phys., vol. 27, page 201, 1982.

[Zhang 1997] F. Zhang. *Operator splitting integrators for constant-temperature molecular dynamics*. J. Chem. Phys., vol. 106, pages 6102–6106, 1997.

[Zhang 2004] J. Zhang, B. D. Todd and K. P. Travis. *Viscosity of confined inhomogeneous nonequilibrium fluids*. J. Chem. Phys., vol. 121, no. 21, pages 10778–10786, 2004.

[Zhang 2005] J. Zhang, B. D. Todd and K. P. Travis. *Erratum: Viscosity of confined inhomogeneous nonequilibrium fluids*. J. Chem. Phys., vol. 122, pages 219901–219902, 2005.

[Zhu 2003] S. Granick Y. Zhu and H. Lee. *Slippery questions of stick when fluid flows past surfaces*. Nature Materials, vol. 2, page 221, 2003.